



Design and Analysis of a Composite Tailcone for the XM-1002 Training Round

**by James M. Sands, James Garner, Peter Dehmer, Uday Vaidya,
Adolfo Villalobos, Juan Serrano, George Husman,
and Robert Brannon**

ARL-TR-4428

April 2008

NOTICES

Disclaimers

The findings in this report are not to be construed as an official Department of the Army position unless so designated by other authorized documents.

Citation of manufacturer's or trade names does not constitute an official endorsement or approval of the use thereof.

Destroy this report when it is no longer needed. Do not return it to the originator.

Army Research Laboratory

Aberdeen Proving Ground, MD 21005-5069

ARL-TR-4428**April 2008**

Design and Analysis of a Composite Tailcone for the XM-1002 Training Round

James M. Sands, James Garner, and Peter Dehmer
Weapons and Materials Research Directorate, ARL

Uday Vaidya, Adolfo Villalobos, Juan Serrano, and George Husman
University of Alabama at Birmingham

Robert Brannon
National Composite Center

REPORT DOCUMENTATION PAGE				Form Approved OMB No. 0704-0188	
Public reporting burden for this collection of information is estimated to average 1 hour per response, including the time for reviewing instructions, searching existing data sources, gathering and maintaining the data needed, and completing and reviewing the collection information. Send comments regarding this burden estimate or any other aspect of this collection of information, including suggestions for reducing the burden, to Department of Defense, Washington Headquarters Services, Directorate for Information Operations and Reports (0704-0188), 1215 Jefferson Davis Highway, Suite 1204, Arlington, VA 22202-4302. Respondents should be aware that notwithstanding any other provision of law, no person shall be subject to any penalty for failing to comply with a collection of information if it does not display a currently valid OMB control number. PLEASE DO NOT RETURN YOUR FORM TO THE ABOVE ADDRESS.					
1. REPORT DATE (DD-MM-YYYY) April 2008		2. REPORT TYPE Final		3. DATES COVERED (From - To) March 2004–April 2005	
4. TITLE AND SUBTITLE Design and Analysis of a Composite Tailcone for the XM-1002 Training Round				5a. CONTRACT NUMBER W911NF-04-2-008	
				5b. GRANT NUMBER	
				5c. PROGRAM ELEMENT NUMBER	
6. AUTHOR(S) James M. Sands, James Garner, Peter Dehmer, Uday Vaidya,* Adolfo Villalobos,* Juan Serrano,* George Husman,* and Robert Brannon†				5d. PROJECT NUMBER	
				5e. TASK NUMBER	
				5f. WORK UNIT NUMBER	
7. PERFORMING ORGANIZATION NAME(S) AND ADDRESS(ES) U.S. Army Research Laboratory ATTN: AMSRD-ARL-WM-MD Aberdeen Proving Ground, MD 21005-5069				8. PERFORMING ORGANIZATION REPORT NUMBER ARL-TR-4428	
9. SPONSORING/MONITORING AGENCY NAME(S) AND ADDRESS(ES)				10. SPONSOR/MONITOR'S ACRONYM(S)	
				11. SPONSOR/MONITOR'S REPORT NUMBER(S)	
12. DISTRIBUTION/AVAILABILITY STATEMENT Approved for public release; distribution is unlimited.					
13. SUPPLEMENTARY NOTES *University of Alabama, Birmingham, AL †National Composite Center, Kettering, OH					
14. ABSTRACT A long-fiber thermoplastic (LFT) composite XM-1002 tailcone has been designed and fabricated to explore the technical feasibility of substituting aluminum-machined tailcones with low-cost, fiber-reinforced polymer tailcones. The design phase of the project involved developing a material model and numerically evaluating the stresses on the projectile using a simulated launch environment. A detailed ANSYS-based finite element analysis (FEA) was undertaken to investigate the behavior of the LFT tailcone compared to the existing aluminum version for various fiber loading. In the analysis, the tailcone was subjected to a variety of mechanical- and thermal-loading conditions. This report summarizes the detailed design and FEA of two versions of the XM-1002 composite tailcone. These are referred to as hollow-back and filled-back. For the hollow-back geometry, the objective was to mimic the external geometry of the presently used aluminum tailcone. The hollow-back tailcone was further investigated for two metal insert geometries, beaded and threaded. Weight reduction with respect to the all-metal (aluminum) version of the tailcone is not desirable; hence a metal insert was used in conjunction with the LFT material. Three conditions with respect to the firing of a projectile have also been discussed—in-bore, transition, and out-of-bore. The response of the LFT composite tailcone to pressure, gravitational load, and temperature has been evaluated. The testing trial held at Aberdeen Proving Ground, MD, demonstrated that the LFT filled-back glass/nylon tailcone with 40% glass loading successfully passed the firing conditions. By implementing the proposed LFT composite tailcone, significant cost savings are projected compared to the existing aluminum version.					
15. SUBJECT TERMS LFT, composite, XM-1002, long-fiber thermoplastic, manufacturing					
16. SECURITY CLASSIFICATION OF:			17. LIMITATION OF ABSTRACT UL	18. NUMBER OF PAGES 84	19a. NAME OF RESPONSIBLE PERSON James M. Sands
a. REPORT UNCLASSIFIED	b. ABSTRACT UNCLASSIFIED	c. THIS PAGE UNCLASSIFIED			19b. TELEPHONE NUMBER (Include area code) (410) 306-0878

Contents

List of Figures	v
List of Tables	x
1. Introduction	1
1.1 Ammunition.....	1
1.2 Practice vs. Battlefield Rounds	2
2. Materials	3
2.1 Composites	3
2.2 Long Fiber-Reinforced Thermoplastics	4
2.3 Material Choice	6
3. XM-1002 LFT Composite Tailcone Design	7
4. Problem Definition	8
4.1 In-Bore Condition.....	9
4.2 Transition Condition.....	9
4.3 In-Flight or Out-of-Bore Condition.....	12
5. Existing Design	12
6. Finite-Element Mesh Details	13
6.1 Element Type	13
6.2 Meshing Approach	14
7. Aluminum Tailcone	15
7.1 Thermal Analysis	16
7.1.1 In-Bore Conditions	16
7.1.2 Out-of-Bore Condition	17
7.2 Structural Analysis	20
7.2.1 In-Bore Conditions	20
7.2.2 Transition Condition.....	21

8. Hollow-Back LFT Tailcone	23
8.1 Thermal Analysis	23
8.1.1 In-Bore Condition.....	24
8.1.2 Out-of-Bore Conditions.....	25
8.2 Structural Analysis	27
8.2.1 Bonding Between Aluminum and Polymer.....	31
8.2.2 In-Bore Conditions	32
8.2.3 Transition Condition.....	36
9. Tests for the Hollow-Back Geometry Tailcones	42
9.1 Beaded Insert Geometry	43
9.2 Threaded Insert Geometry	46
10. Filled-Back LFT Tailcone	47
10.1 Two Different Insert Geometries.....	50
10.1.1 Rationale for the 95-mm Insert Geometry	50
10.1.2 Rationale for the 100-mm Insert Geometry	51
10.2 Structural Analysis	51
10.2.1 In-Bore Conditions	51
10.2.2 Transition Condition.....	54
11. Tests for the Filled-Back Geometry Tailcones	63
12. Summary and Conclusions	66
13. References	67
Distribution List	69

List of Figures

Figure 1. Components of typical military ammunition.....	1
Figure 2. Configuration of projectiles: (a) training round, (b) battlefield round, and (c) position of tailcone with respect to the origin.....	2
Figure 3. Difference in the modulus of the polymer and fiber yields a combined modulus for the PMC.	4
Figure 4. Single fiber pullout test to find the critical fiber length.	5
Figure 5. Force vs. embedded length for a single fiber pullout test. Prior to the critical length l_c , the force is proportional to the length. After l_c is reached, this force is constant.	5
Figure 6. Tailcone geometry: (a) threaded and (b) beaded.	8
Figure 7. Insert geometry: (a) 100- and (b) 99-mm length.	8
Figure 8. In-bore and transition conditions for tailcone analysis.....	9
Figure 9. Acceleration and pressure in-bore for the XM-1002 projectile.....	10
Figure 10. Temperature in-bore for the XM-1002 projectile.....	10
Figure 11. Mohr's circles for transition and in-bore conditions. The graph does not represent actual values but is only an illustration to explain the differences in the applied loads.	11
Figure 12. Transformation of applied pressure into a force and a moment (note that $P_2 \gg P_0$).	11
Figure 13. XM-1002 and M865 tailcones.....	12
Figure 14. Explosion of a large-caliber projectile.	13
Figure 15. General geometry of PLANE 42 element.	14
Figure 16. Finite-element mesh for XM-1002 tailcone generated using quads and corresponding axisymmetric expansion of 2-D model.	15
Figure 17. Corresponding finite-element mesh for hollow-back tailcone and filled-back tailcone.....	15
Figure 18. Initial conditions for the in-bore thermal analysis of the aluminum tailcone.....	17
Figure 19. Transient thermal in-bore analysis for the steel and aluminum parts. The 0.8 mm of temperature-affected molten material is shown.....	18
Figure 20. Initial conditions for the out-of-bore thermal analysis of the aluminum tailcone. In this case, the temperature is only applied to the outer part of the tailcone, which is in direct contact with the flowing air.	19
Figure 21. Transient thermal out-of-bore analysis for the steel and aluminum parts. The 3-D temperature visualization is presented to provide a better understanding of the material response.....	19
Figure 22. Initial conditions for the in-bore structural analysis of the aluminum tailcone.....	21

Figure 23. Von Mises stress plot for the 7075 aluminum tailcone at in-bore condition. The top-right part shows maximum stresses.....	22
Figure 24. Initial conditions for the transition regime structural analysis of the aluminum tailcone.....	23
Figure 25. Von Mises stress plot for the 7075 aluminum tailcone at transition condition (acceleration of $63,000 \text{ m/s}^2$ in the $-y$ direction). The maximum applied stress is 1030 MPa and is located in the top-right corner.....	24
Figure 26. Von Mises stress plot for the 7075-T6 aluminum tailcone at transitions regime. The maximum applied stress is 1090 MPa (6% higher than the case with acceleration) and is located at the top-right corner.....	25
Figure 27. Detail of the von Mises stress plot. The scale is changed so the maximum stress shown is the yield stress. Any stress higher than the yield strength is shown as a gray region.	26
Figure 28. Initial conditions for the in-bore analysis of the LFT tailcone.....	26
Figure 29. In-bore thermal analysis for the LFT, steel, and aluminum parts. In this case, only 0.4 mm of heat-affected material is observed.....	27
Figure 30. Initial conditions for the tailcone in out-of-bore conditions. The conditions from the in-bore analysis were used as the initial temperature.	28
Figure 31. Out-of-bore thermal analysis for the LFT, steel, and aluminum parts. The maximum applied temperature at 5 s is 675 K. In this case, the shoulder acts as a heat sink.....	29
Figure 32. Detail of out-of-bore thermal analysis for the LFT, steel, and aluminum parts. The maximum temperature on the scale is 570 K, which is the melting temperature for the LFT.....	30
Figure 33. Section of the LFT-aluminum interface in the hollow-back threaded insert tailcone. There is a high concentration of nylon in the threads.	32
Figure 34. Initial conditions for the in-bore structural analysis of the LFT section of the beaded tailcone.....	32
Figure 35. Tsai-Wu failure criterion plot for the beaded LFT section of the tailcone at in-bore conditions. The maximum value is 1.437 and is located at the edge of the bead. A stress concentrator, due to the presence of the steel projectile, is observed in the top-right corner of the tailcone.	34
Figure 36. Detail of the Tsai-Wu failure criterion plot for the beaded LFT section of the tailcone at in-bore conditions. The failure region in the interface is 6% of the complete interface between the LFT and the aluminum insert.	35
Figure 37. Vector plot that shows the displacement of the beaded LFT section of the tailcone comparing it to its original position. The bead acts as a “splitting” nose for the LFT.	36
Figure 38. Detail of thread in LFT-aluminum interface. The small radius in each thread is approximated to be a sharp corner that is fully constrained.	37
Figure 39. Initial conditions for the in-bore structural analysis of the LFT section of the threaded tailcone. The detail shows the threads as fully constrained at each corner.....	37

Figure 40. Tsai-Wu failure criterion plot for the threaded LFT section of the tailcone at in-bore conditions. The maximum value is 1.247 and is located at the top-right part of the tailcone due to the presence of the steel projectile in the top-right corner of the tailcone.	38
Figure 41. Detail of the Tsai-Wu failure criterion plot for the threaded LFT section of the tailcone at in-bore conditions. The LFT-aluminum interface is under the critical value of the stress.....	39
Figure 42. Vector plot that shows the displacement of the threaded LFT section of the tailcone compared to its original position. The threads restrict movement and cause better distribution of the stresses.....	40
Figure 43. Displacement per node on the transition analysis for the beaded geometry. The blue arrows represent the displacement of the marked nodes as they tend to separate the aluminum insert. The red arrows represent their displacement toward the insert.	41
Figure 44. Tsai-Wu failure criterion plot for the beaded LFT section of the tailcone at transition conditions. The maximum value is 2.487 and is located at the edge of the bead. ..	42
Figure 45. Detail of the Tsai-Wu failure criterion plot for the beaded LFT section of the tailcone at transition conditions. The failure path in the top part is due to the neck that is created with the load.	43
Figure 46. Vector plot that shows the displacement of the threaded LFT section of the tailcone comparing it to its original position. The region shown as the axis of rotation is where the maximum loads are applied.....	44
Figure 47. Displacement per node on the transition analysis for the threaded geometry. The displacements move in a counter-clockwise manner around the center point.....	45
Figure 48. Initial conditions for the transition structural analysis of the LFT section of the threaded tailcone. The expanded view highlights that there are only constraints where the material displaces toward the insert.....	45
Figure 49. Tsai-Wu failure criterion plot for the threaded LFT section of the tailcone at transition conditions. The maximum value is 3.737 (33% higher for the beaded geometry), which can be attributed to the larger constrained area.	46
Figure 50. Detail of the Tsai-Wu failure criterion plot for the threaded LFT section of the tailcone at transition conditions. The failure path in this geometry is longer than the beaded. The failure path increase and decrease in neck length is an advantage over the beaded geometry.	47
Figure 51. Fired projectile with beaded geometry at 15 m. The failure path and the line where the tailcone separates from the insert coincide with the FEA.....	48
Figure 52. Fired projectile with threaded geometry at 15 m. The failure path coincides with the FEA.	49
Figure 53. Transformation of the applied pressures into a force and a moment. The figure shows the filled-back geometry compared to the hollow-back geometry. The arm for the filled-back geometry is 40% smaller.	50
Figure 54. Initial conditions for the in-bore structural analysis of the LFT section of the 95-mm insert tailcone. The expanded inset highlights that the threads are fully constrained at each corner and normally constrained at each groove.....	51

Figure 55. Tsai-Wu failure criterion plot for the 95-mm insert LFT section of the tailcone at in-bore conditions. The maximum value is 1.307 and is located at the bottom corner where the threads meet the lip. This is due to the splitting nose effect seen also in the beaded geometry.	52
Figure 56. Detail of the Tsai-Wu failure criterion plot for the 95-mm insert LFT section of the tailcone at in-bore conditions. The area of the failure region is 0.6% of the total LFT area.	53
Figure 57. Initial conditions for the in-bore structural analysis of the LFT section of the 95-mm insert tailcone. The detail shows the threads fully constrained at each corner and normally constrained at each thread.	54
Figure 58. Tsai-Wu failure criterion plot for the 100-mm insert LFT section of the tailcone at in-bore conditions. The maximum value is 1.494 and is located at the top corner where the LFT meets the steel projectile.	55
Figure 59. Detail of the Tsai-Wu failure criterion plot for the 100-mm insert LFT section of the tailcone at in-bore conditions. The failure region area is 0.1% of the total LFT area.	56
Figure 60. Initial conditions for the transition structural analysis of the LFT tailcone with a 95-mm insert. The detail shows the threads constrained normally in the top surface of each thread. The applied pressure is only in the y direction.	57
Figure 61. Displacement-per-node plot for the 95-mm insert geometry at the transition condition. No stationary point can be seen in the geometry, thus no rotation axis was assumed.	57
Figure 62. Tsai-Wu failure criterion plot for the 95-mm insert LFT section of the tailcone at the transition condition. The maximum failure criterion value is 2.789.	58
Figure 63. Detail of the Tsai-Wu failure criterion plot for the 95-mm insert LFT tailcone at the transition condition. The probable failure path divides the lip from the tailcone. The lip will be compressed toward the insert by the pressure at transition.	59
Figure 64. X-displacement plot of the 95-mm insert LFT section of the tailcone. A maximum displacement of 0.09 mm is calculated for the threads under load.	60
Figure 65. Initial conditions for the transition structural analysis of the LFT section of the 100-mm insert tailcone. The detail shows the threads constrained normally in the top surface of each one. The applied pressure is only in the y direction.	61
Figure 66. Tsai-Wu failure criterion plot for the 100-mm insert LFT section of the tailcone at the transition condition. The maximum failure criterion value is 2.185.	62
Figure 67. Detail of the Tsai-Wu failure criterion plot for the 100-mm insert LFT section of the tailcone at the transition condition. From a structural point of view, this geometry has better performance than the 95-mm insert geometry.	63
Figure 68. X-displacement plot of the 100-mm insert LFT section of the tailcone. A maximum displacement of 0.345 mm is calculated for the threads under load (3.6× greater than for the 95-mm insert geometry).	64

Figure 69. Fired projectile with full-back LFT tailcone geometry at 5 m. The filled-back tailcone maintained its integrity at a 5-m distance.....	65
Figure 70. Fired projectile with full-back LFT tailcone geometry at 15 m. The filled-back tailcone maintained its integrity at a 15-m distance.....	65

List of Tables

Table 1. Structural, thermal, and economical properties of three main candidates for the LFT tailcone material (data for 40% glass fiber by weight).	7
Table 2. Properties for the XM-1002 and the M865 projectile.....	16
Table 3. Properties for 7075 T-6 aluminum and steel.	16

1. Introduction

Military ammunition can be divided into three groups: small, medium, and large caliber (1). The small caliber is used in a variety of infantry and mounted weapons, such as the M16 rifle and M4 carbine; the M14 and M24 sniper rifles; the M249 and M240 machine guns, and the M2 .50-caliber machine gun. Medium caliber is used in the GAU-8 seven-barrel machine gun and the M230 chain cannon. They are mounted on Apache helicopters, A-10 Thunderbolt II aircraft, and Bradley infantry fighting vehicles. They are classified as 20-, 25-, and 30-mm rounds. Large-caliber rounds are used in fixed cannons, such as the M1A1 and M1A2 Abrams tanks. These are the 105- and 120-mm rounds. They are capable of destroying light armored vehicles, structures, and helicopters. In the case of the 120-mm ammunition, there are several types of projectiles, depending on the need. The high-explosive antitank projectile explodes at the moment of impact. The high-explosive obstacle reduction penetrates the obstacle by means of a hard steel nose and then explodes. The canister cartridge then separates into smaller pieces and is used against infantry, and the armor-piercing projectiles (kinetic energy penetrator) penetrate the structure. Bits of broken armor and the residual shell content are sent flying inside the tank, ruining equipment and incapacitating crewmen (1).

1.1 Ammunition

The basic ammunition consists of a cartridge case, a primer, a projectile, and the propellant (figure 1) (2). When the primer is ignited, the propellant (which is the explosive charge) creates a hot, expanding gas that pushes the projectile out of the case. The sabot confines the projectile to the size of the inner diameter of the canon.

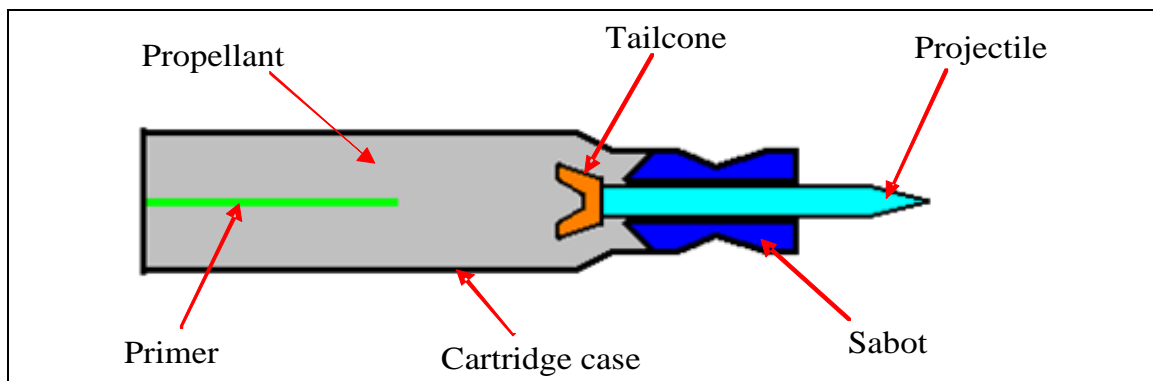


Figure 1. Components of typical military ammunition.

Projectile: The projectile portion of ammunition is the part that is propelled from the canon toward the target. The projectile is measured in calibers according to the diameter of the canon bore. Projectiles are made of depleted uranium (for their high density) or steel.

Cartridge Case: The metal cylinder (open at the mouth and closed at the base) holds the projectile, propellant, and primer.

Propellant: The combustible propellant occupies the space between the projectile and the primer inside the case. On detonation, the ignited powder rapidly decomposes into a hot, forceful gas that instantaneously expands and propels the projectile out of the bore. Powder grains are produced in different shapes and sizes to control the burn rate. The grains can also have different surface coatings.

Primer: The primer is a self-contained metallic ignition rod at the center of the ammunition case. When struck by the firing pin, the primer combusts, sending sparks through the case, and ignites the powder charge. Primers are components made of ignition chemicals, a cup, and an anvil.

1.2 Practice vs. Battlefield Rounds

Practice (or training) ammunition is often used for training military personnel. In terms of safety, range, and cost, training rounds are used to provide a realistic simulation of tank cannon ammunition in a controlled environment. The main purpose of these rounds is to provide training personnel the maximum projectile-operation experience in a practice range. Practice rounds utilize a slotted tailcone that limits the range to a permitted maximum. In addition to limiting the range, the tailcone stabilizes the projectile (figure 2).

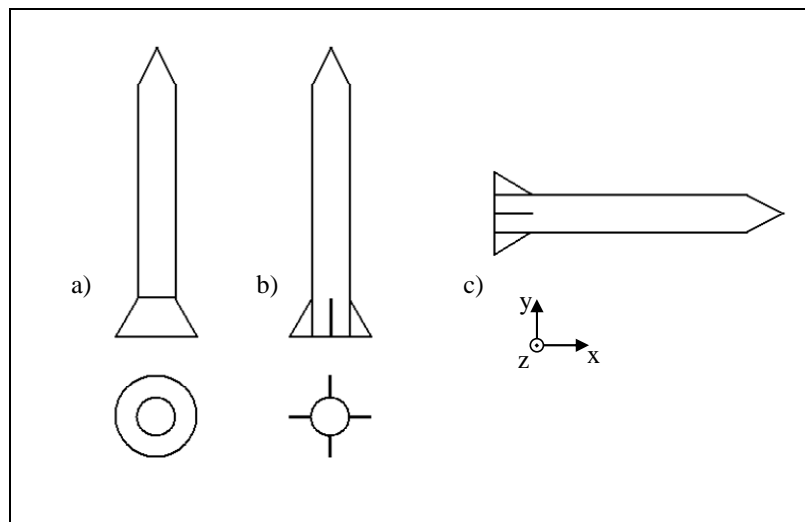


Figure 2. Configuration of projectiles: (a) training round, (b) battlefield round, and (c) position of tailcone with respect to the origin.

The battlefield round is made of depleted uranium (less than 0.7% of the isotope uranium-235), which has more than twice the density of steel ($19,000 \text{ kg/m}^3$ vs. 7800 kg/m^3) (1). Heavy metals like depleted uranium are used to obtain a higher weight projectile (more kinetic energy).

Typical battlefield rounds have a maximum reach of 8000 m and a target range between 3000 and 4000 m (1). They achieve this higher range because instead of a tailcone design (with slots) that causes deceleration, these have a finned tail.

By comparing the geometry of a tailcone to the geometry of a finned tail, it may be noted that the two different geometries cause completely different effects on their aerodynamic behavior. The shape of the tailcone causes turbulence at the back end of its geometry that decelerates the projectile (3, 4). This occurs because this turbulence causes the boundary layer to separate from the tailcone, thereby providing drag. In the case of the finned tail, the fins are used to maintain the position of the projectile (no rotation in the Y or Z axis).

The present design (used by the Army) of the tailcone utilizes 7075 aluminum, which is a high-strength material used for highly stressed structural parts, such as aircraft fittings, gears and shafts, missile parts, and aerospace and defense applications. Cost is a major concern because 7075-T6 aluminum alloy is an expensive material, and the machining cost for over 250,000 parts per year is not trivial. Hence the motivation for the present work is identifying and pursuing alternate materials and technologies.

2. Materials

2.1 Composites

The focus of this work is to investigate polymer matrix composites (PMCs) for the tailcone application. Pure polymers have desirable properties, most notably their ability to easily form into complex shapes. However, homopolymers have limited mechanical properties (compared to metals). Materials such as glass, aramid, or carbon have extremely high mechanical properties; although in a bulk form, these properties are not realized. Random surface flaws cause the material to crack and fail well below its theoretical strength; hence the material is produced in fiber form, which contains a lower probability of aligned defects. Even if the same probability of a random flaw exists, its size is limited to the size of the fiber, allowing the rest of the fibers in a bundle to achieve close to the material theoretical strength. Most fibers are highly directional and exhibit superior strength and stiffness in the axis of the fiber and lower strength and stiffness in the transverse axis (5).

PMCs combine a polymer system and reinforcing fibers. The properties of the resulting composite material will combine the properties of the constituent polymer and fibers (figure 3) (5). The polymer matrix distributes the applied load to the composite between each of the individual fibers and also protects the fibers from being damaged from impact or other external loads. The advantages of PMCs over metals include high strength and stiffness, ease of manufacturing complex shapes, higher environmental resistance, and lower density.

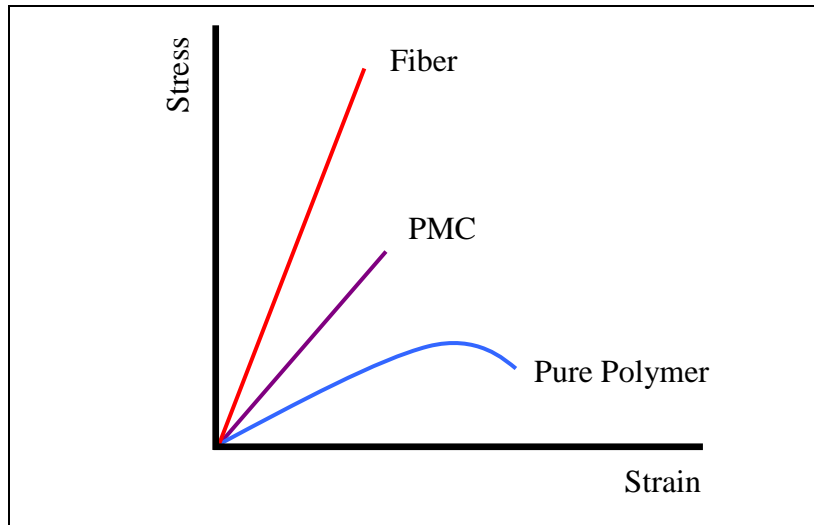


Figure 3. Difference in the modulus of the polymer and fiber yields a combined modulus for the PMC.

The composite properties are determined by the following:

- The properties of the fiber.
- The properties of the polymer.
- The ratio of fiber to polymer in the composite (fiber-volume fraction).
- The geometry and orientation of the fibers in the composite.
- The interface between the fiber and the matrix.

Since the mechanical properties of fibers are higher than those of polymers, the higher the fiber-volume fraction, the higher the mechanical properties of the resultant composite. PMCs can have highly anisotropic properties and can be tailored in different directions.

2.2 Long Fiber-Reinforced Thermoplastics

Long fiber-reinforced thermoplastics (LFTs) are discontinuous fiber composites that have fiber lengths between 7 and 25 mm, depending on the fiber, the matrix, and the type of sizing (if any) (6). Unlike short fiber-reinforced thermoplastics, LFTs possess high strength, stiffness, and impact properties. In addition, they have high-volume processability, the ability to fill complex geometries, the intrinsic capacity to be recycled, and the capacity for parts integration.

LFTs are typically made of a low-cost polymer like polypropylene (PP), polyethylene, polyamide (PA), and polycarbonate reinforced with glass, carbon, or aramid fibers. E-glass fiber is commonly used because of its best cost-to-performance ratio. The fiber-aspect ratio, defined as the length-to-diameter ratio, differentiates short fiber from long fiber reinforcement. The aspect ratio of a long fiber is typically an order of magnitude higher than that of a short fiber (7). While short fiber-reinforced thermoplastics realize substantial gains in mechanical properties

over that of homopolymer, the full potential of the reinforcement is not realized because the fiber is below a critical length (l_c). The fracture strength of the fiber (σ_f), the radius (r), and the yield shear strength of the matrix (τ_y) is related by (8)

$$l_c = \frac{\sigma_f r}{2\tau_y}. \quad (1)$$

For the case where the fiber is loaded by the matrix and not by an external force as it is done in the pullout test (figures 4 and 5), equation 1 is stated as (5)

$$l_c = \frac{\sigma_f r}{\tau_y} \text{ or } \frac{l}{r} = \frac{\sigma_f}{\tau_y}. \quad (2)$$

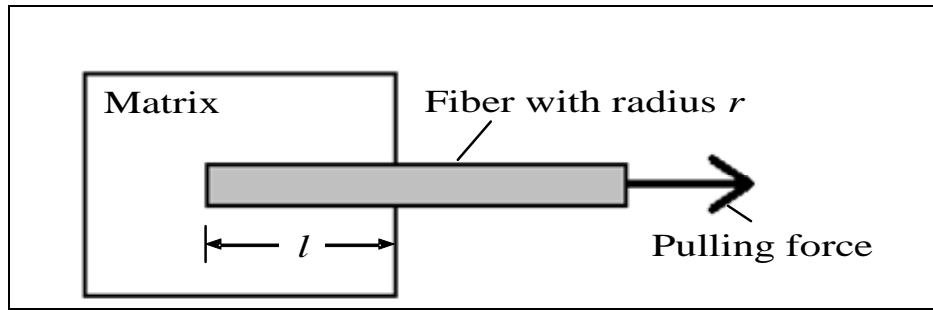


Figure 4. Single fiber pullout test to find the critical fiber length.

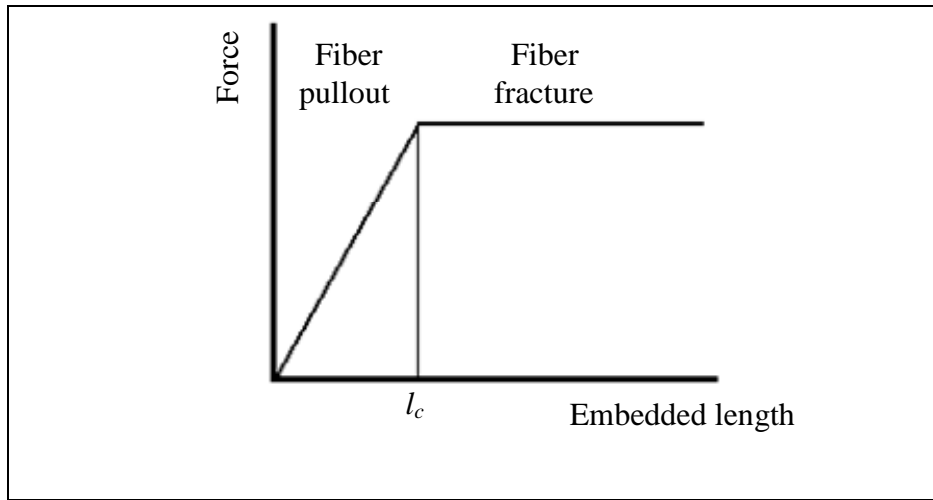


Figure 5. Force vs. embedded length for a single fiber pullout test. Prior to the critical length l_c , the force is proportional to the length. After l_c is reached, this force is constant.

There are a couple of simplifying assumptions for these equations. The first is that the strain to failure for the fiber is less than that for the matrix. This assumption is usually correct for a thermoplastic matrix. The second assumes constant interface shear strength over the fiber length, which is not totally correct (9). Fibers produce higher stresses at their tips, resulting in lower elongation to failure.

2.3 Material Choice

There are many factors involved in selecting the material: strength (tension compression and impact), modulus, tenacity, density, processability, melt temperature, thermal conduction, heat capacity, and cost. The candidate material for the application requires high thermal and structural properties and compatibility to a metallic insert, as will be discussed later. In the present work, three candidate polymers were considered for the tailcone application. These are PA, also called nylon, PP, and polyetheretherketone (PEEK).

For structural design purposes, the materials are loaded to a fraction of the ultimate load in order to prevent failure. If the material has a very high modulus but a very low ultimate strain, it will fail catastrophically when the ultimate load is attained. If the material has large deformation capability but a very low modulus, it will not retain its shape and its large deformation would cause mechanical-bond failure to a metallic insert. Hence an optimal compromise between strength, modulus, and maximum deformation was required for the XM-1002 tailcone application. The thermal properties were very important in choosing the material, because the material would be subjected to high temperatures during processing and in service. Factors such as thermal resistance, melting temperature, and thermal conduction are important.

Table 1 compares the properties of three polymer-system candidates for 40% glass fiber content LFT (10). From this table, the best candidate from a thermal and structural point of view appears to be PEEK. However, PEEK is a very expensive material and requires a very high processing temperature. Cost reduction is the main driver for replacing the aluminum tailcone. Therefore, a compromise had to be made between using a material with superior mechanical properties against cost. Although the modulus is 10% higher for PEEK than for PA, and melting temperature of PEEK is about twice that of nylon, the price is 20× higher. This was the rationale for choosing nylon as the candidate for the tailcone material. Other factors for choosing the material included environmental resistance and compatibility with propellant.

Table 1. Structural, thermal, and economical properties of three main candidates for the LFT tailcone material (data for 40% glass fiber by weight).

Property	Nylon	PP	PEEK
Density (kg/m ³)	1460	1210	1610
Ultimate strength (MPa)	221	62	186
Modulus (GPa)	13.8	8.3	15.1
Melting temperature (°C)	299	232	399
Thermal conductivity (W/m*K)	0.52	0.35	0.39
Specific heat (J/kg*K)	2200	2200	1900
Price (\$/kg) (11)	3.3	2.2	72.6

3. XM-1002 LFT Composite Tailcone Design

This report provides details on two versions of the design and analysis of the LFT composite tailcone. These are referred to as hollow-back and filled-back geometry throughout the document. For the hollow-back geometry, the objective was to mimic the external geometry of the presently used (by the Army) aluminum tailcone. The hollow-back tailcone was further investigated for two metal insert geometries, beaded and threaded (figure 6). The main idea behind the metal insert concept will be explained in section 7, but to give a brief introduction, the insert is a 6061 aluminum stud used to mate the tailcone to the projectile and provide weight to the tailcone. The objective does not call for weight reduction with respect to the all-metal (aluminum) version of the tailcone that is presently adopted by the Army. In fact, weight reduction would change the projectile's center of gravity. The necessity to maintain the identical weight between the LFT and the all-metal tailcone will be explained later in section 7.

After firing trials were conducted with the hollow-back geometry tailcones (figure 6), it was deemed necessary to redesign them to withstand the various loading conditions. A second set of geometries featuring the filled-back LFT material (section 9) was designed and analyzed (figure 7). As the names suggest, the filled-back version featured a reinforced back that diminished the applied loads and the resulting stresses on the tailcone, making it more effective to withstand the firing scenario.

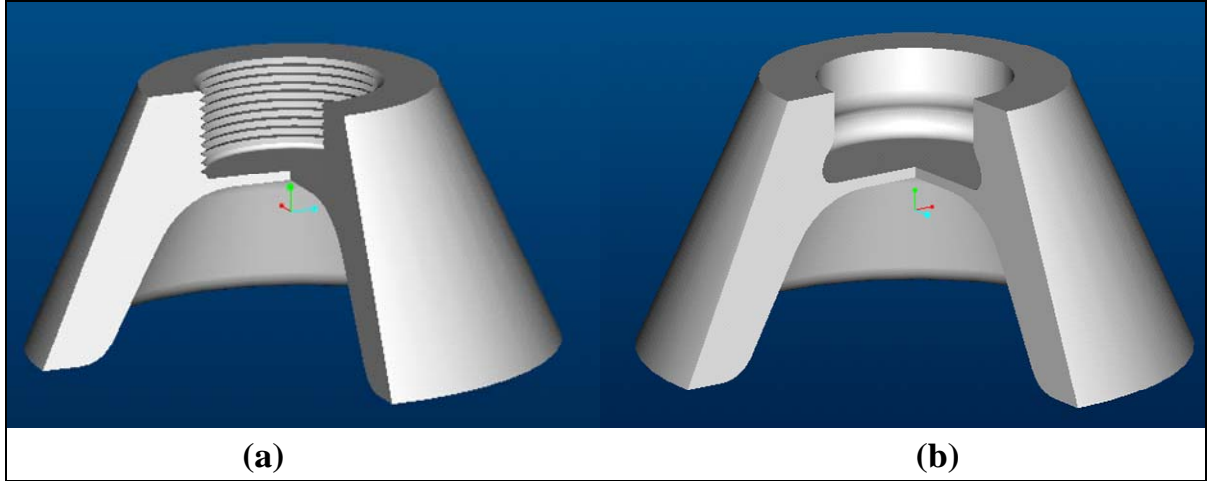


Figure 6. Tailcone geometry: (a) threaded and (b) beaded.

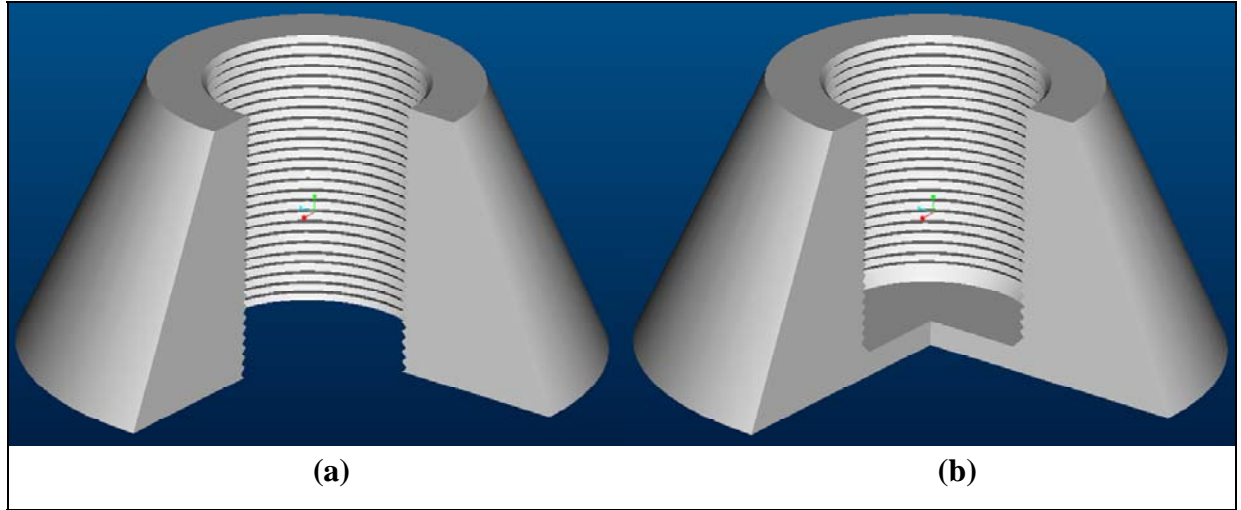


Figure 7. Insert geometry: (a) 100- and (b) 99-mm length.

4. Problem Definition

This work focused on the design, analysis, and manufacture of the XM-1002 projectile. The tailcone is a component of the XM-1002 projectile. The loads on the tailcone can be divided into three conditions—in-bore, transition (figure 8), and out-of-bore. The in-bore condition corresponds to the tailcone loads at the instant of firing, i.e., when the projectile is resident in the bore. The transition condition corresponds to the instance of the tailcone exiting the bore. The out-of-bore condition corresponds to the flight of the projectile along with the tailcone.

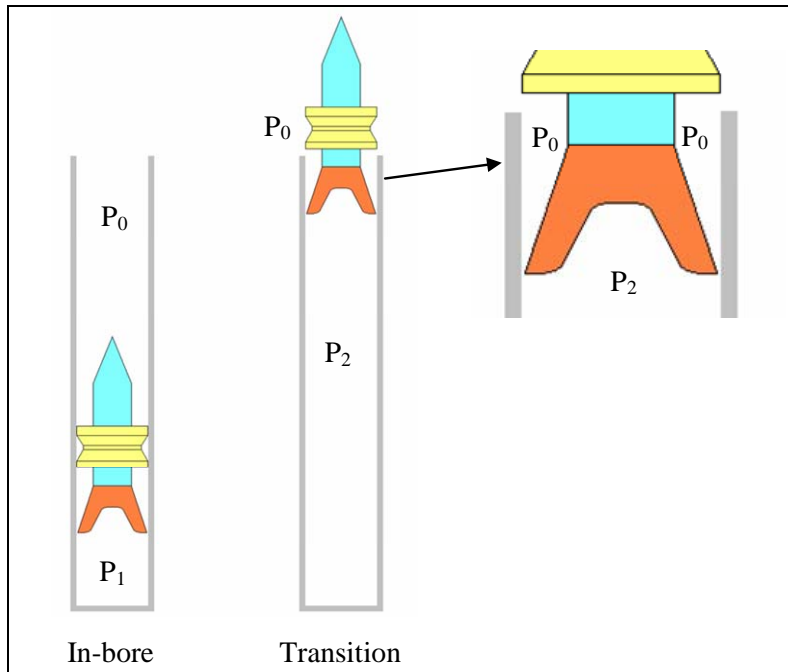


Figure 8. In-bore and transition conditions for tailcone analysis.

4.1 In-Bore Condition

The tailcone is subjected to harsh loading conditions. From figure 1, it can be seen that this is the only part of the projectile that is completely inside the chamber at the moment of firing and therefore experiences the highest loads. The in-bore condition creates the highest pressure and temperature profiles on the projectile. The in-bore pressure and acceleration data vs. time for the XM-1002 projectile are plotted in figure 9 (12).

The projectile takes 6.15 ms to reach the end of the bore, and in that time, the part has to withstand a maximum acceleration of $434,140 \text{ m/s}^2$ (44,300 g's) and a maximum hydrostatic pressure of 406 MPa at 1.95 ms. The tailcone is simultaneously subjected to an average temperature of 1970 K, which is obtained from the values in figure 10 (12). Although these are very harsh conditions from both structural and thermal perspectives, the exposure interval is a mere 6 ms, which minimizes the degradation window, especially coupled with the low thermal conductivity of the PMC resin.

4.2 Transition Condition

The most critical condition in terms of stresses witnessed by the tailcone is the transition condition. In this condition, the applied pressure is about $6.7\times$ smaller than the highest pressure the tailcone has to withstand (in-bore), but there is a differential in pressure that is not experienced in-bore. It is this differential in pressure that causes the higher stresses. The in-bore

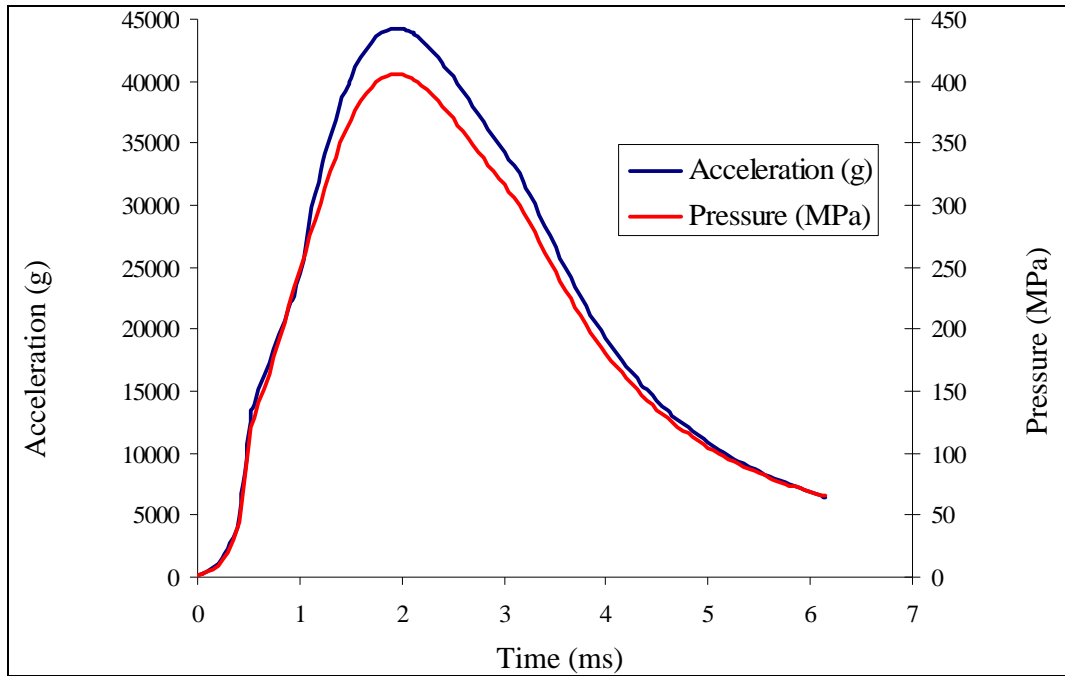


Figure 9. Acceleration and pressure in-bore for the XM-1002 projectile.

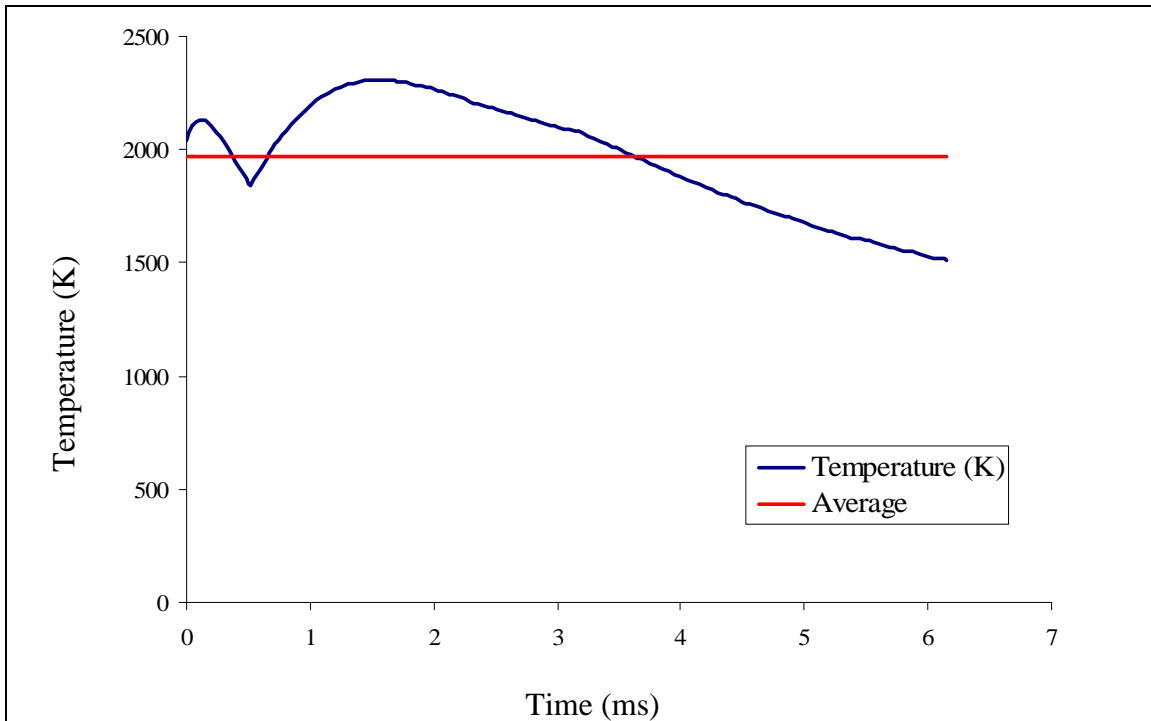


Figure 10. Temperature in-bore for the XM-1002 projectile.

pressure is essentially a hydrostatic pressure. This means that the value of the pressure is approximately the same over the entire volume of the part (the same effect as placing the tailcone underwater). Compared to the hydrostatic pressure (from the in-bore loading condition), the pressure differential (from the transition condition) is a more critical loading scenario. This can be illustrated from a Mohr's circle representation of shear stresses as shown in figure 11 (13). Both the in-bore (hydrostatic) and the transition (pressure differential) are plotted in this figure.

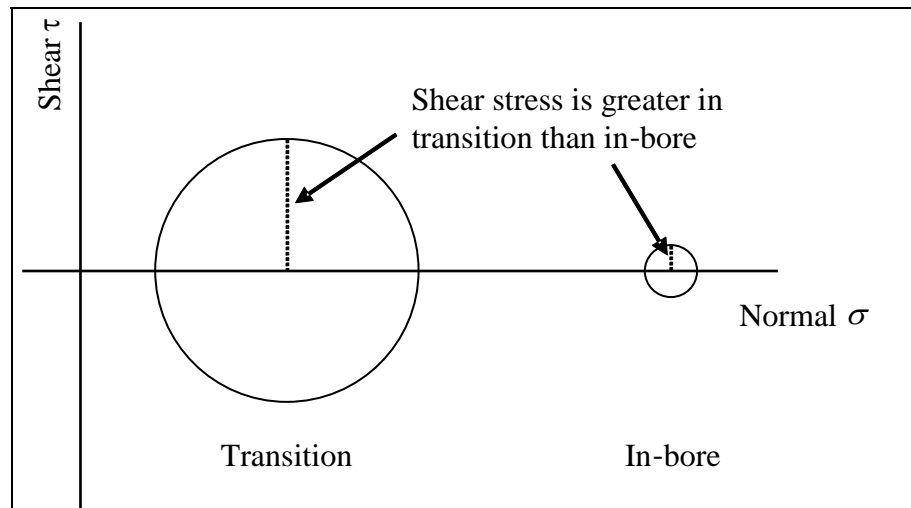


Figure 11. Mohr's circles for transition and in-bore conditions. The graph does not represent actual values but is only an illustration to explain the differences in the applied loads.

The difference in pressure that is represented by the larger-radius circle signifies the pushing outwards of the “arm” of the tailcone. Figure 12 shows the loads on the tailcone in the transition condition. The pressure differential can be represented by a single force applied at a distance L of the axis of rotation. This force creates a moment arm that results in bending, hence opening the tailcone from the metal insert.

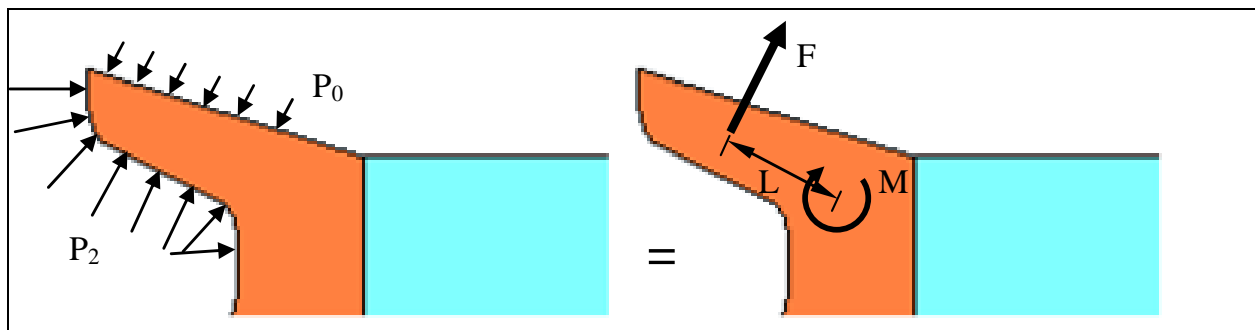


Figure 12. Transformation of applied pressure into a force and a moment (note that $P_2 \gg P_0$).

4.3 In-Flight or Out-of-Bore Condition

The loads induced by the aerodynamic forces are experienced by the tailcone in the out-of-bore condition. Here, the applied loads cause stresses in the tailcone that are various orders of magnitude lower than those induced in-bore and in the transition condition. For the out-of-bore (i.e., in flight) condition, the analysis focused mainly on the temperature from thermodynamic drag.

5. Existing Design

The existing design of the tailcone for the XM-1002 projectile has two functions: to align and decelerate the projectile. The alignment is done by the slots (figures 13 and 14). There are six air passages radially positioned and oriented 60° from each other. In the XM-1002, the slots are slanted 10° with respect to the axis of the projectile. The purpose of slanting the slots is to gyroscopically stabilize the projectile (14). The deceleration is achieved by creating turbulence behind the projectile. The widest part of the tailcone creates vorticities that reduce the air pressure in the back of the projectile. This reduction in pressure decelerates the projectile.

The tailcone is fit to the projectile via threads (figure 13). The projectile has inner threads that mate to the outer threads of the tailcone. An O-ring (figure 14) between the projectile and the tailcone prevents high pressure and high temperature gases from coming into contact with the threads, thereby preventing their damage (14).

From figure 14, it can be seen that the tailcone has a second source of heat that has to be taken into account in the design, i.e., the tracer. This is a small insert that is threaded to the back of the tailcone. The purpose of the tracer is to ignite as soon as the projectile leaves the bore, which then allows tracking the trajectory of the projectile.

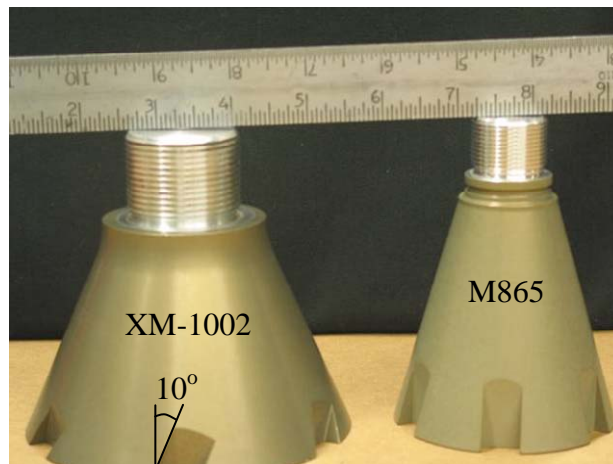


Figure 13. XM-1002 and M865 tailcones.

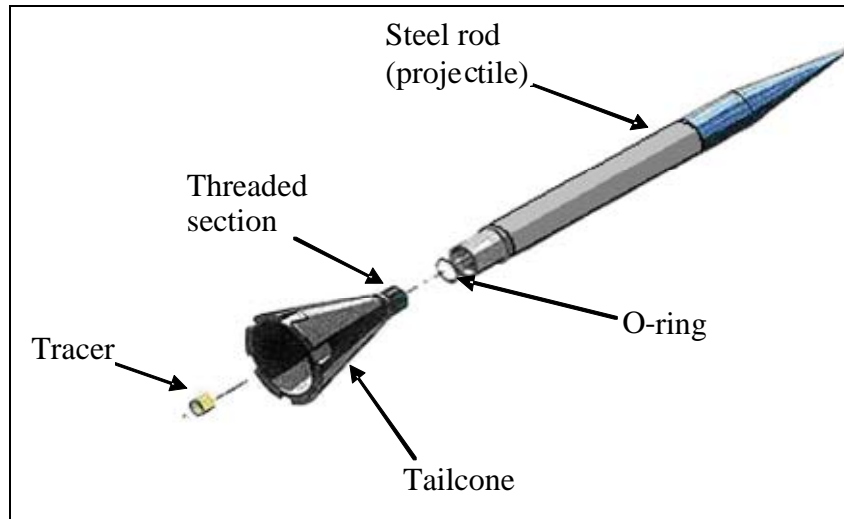


Figure 14. Explosion of a large-caliber projectile.

6. Finite-Element Mesh Details

The structural and thermal analyses were performed using ANSYS 8.0. Two-dimensional (2-D) axisymmetric tailcone mesh was generated to optimize computational time for solution convergence. This approach assumes that the tailcone is always subjected to the same loading condition regardless of the position around the vertical axis (axisymmetric loading in the tailcone faces). The use of an expandable 2-D model allows for the use of a highly refined finite element mesh.

6.1 Element Type

PLANE 42 was used as the element type for the pressure and gravitational simulations. PLANE 42 is commonly used for 2-D solid-structural modeling. It can be used either as a plane element (plane stress or plane strain) or as an axisymmetric element. The element is defined by four nodes having 2 degrees of freedom at each node (translations in the nodal x and y directions). The element has plasticity, creep, swelling, stress-stiffening, large-deflection, and large-strain capabilities. PLANE 42 only accepts axisymmetric loading.

The element input data includes four nodes and the orthotropic material properties. The default element coordinate system is along global directions. Pressures may be input as surface loads on the element faces as shown by the circled numbers in figure 15. Positive pressures act into the element.

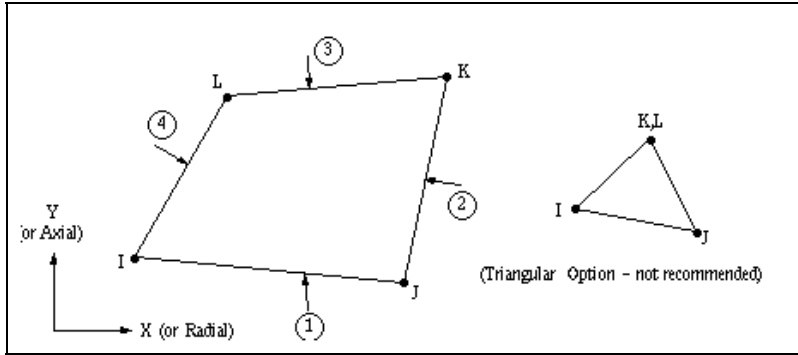


Figure 15. General geometry of PLANE 42 element.

PLANE 55 was used for tailcone thermal analysis both in-bore and out-of-bore. PLANE 55 can be used as a plane element or as an axisymmetric ring element with a 2-D thermal conduction capability. The element has four nodes with a single degree of freedom, i.e., temperature, at each node. The element is applicable to a 2-D, steady-state, or transient-thermal analysis. The element can also compensate for mass transport heat flow from a constant velocity field. PLANE 55 only accepts axisymmetric loading.

6.2 Meshing Approach

The use of triangular elements is not recommended for bending scenarios (such as the transition stage) due to possible over-stiffening of the structure. Therefore, the mesh was generated using the four-node quadrilateral option. The mesh generated was based on the outer geometry of the tailcone by individual mesh-refining using the smart sizing option. The finite element mesh was checked for individual element connectivity and for other general mesh quality requirements, such as aspect ratio and internal angles. An example of a typical mesh used in this analysis and its corresponding three dimensional (3-D) axisymmetric expansion is shown in figure 16. The finite element meshes used for the hollow tailcone analysis and the 95-mm filled-back tailcone is also shown in figure 17. It should be noted that a very fine mesh was used to effectively capture the stress/displacement development in the tailcone at the different loading stages.

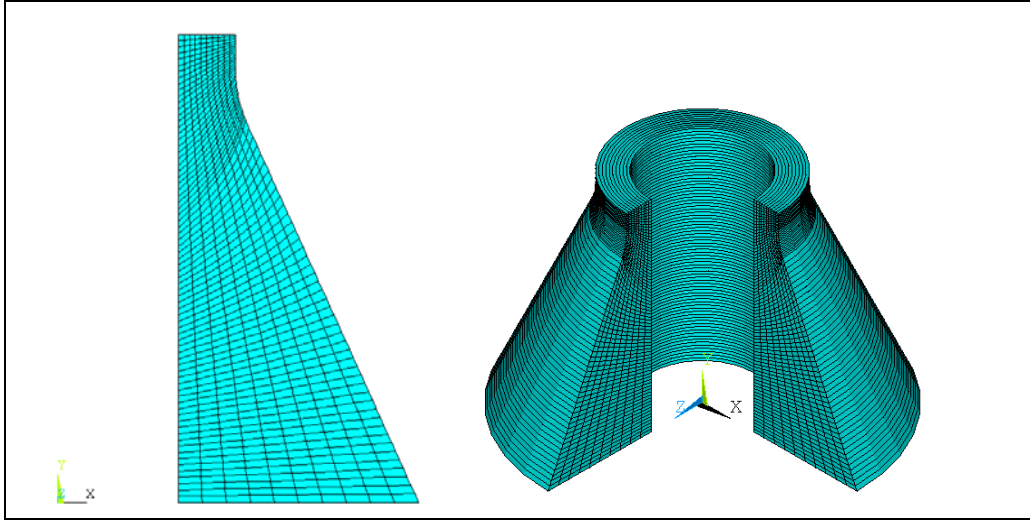


Figure 16. Finite-element mesh for XM-1002 tailcone generated using quads and corresponding axisymmetric expansion of 2-D model.

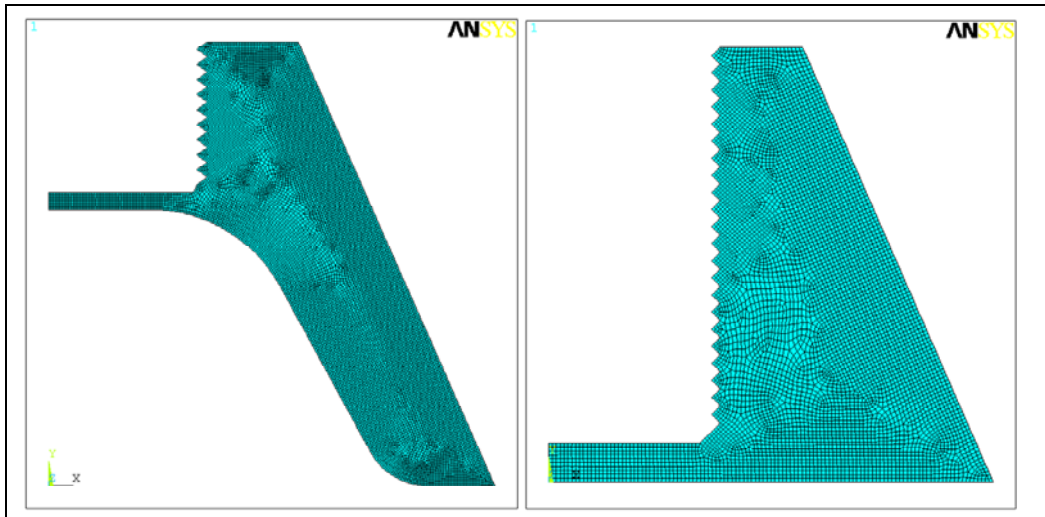


Figure 17. Corresponding finite-element mesh for hollow-back tailcone and filled-back tailcone.

7. Aluminum Tailcone

Two types of tailcones for the XM-1002 and the M865 projectiles were initially evaluated in the program as shown in figure 13 and table 2. The XM-1002 tailcone design and analysis was fully developed as part of the program. The existing 7075 aluminum tailcone for the XM-1002

projectile was modeled to study the baseline design for the loading conditions. For these simulations, the properties for 7075-T6 aluminum are shown in table 3. The structural simulations considered the pressure and the acceleration, while the thermal analysis measured temperature.

Table 2. Properties for the XM-1002 and the M865 projectile.

Property	XM-1002	M865
Projectile length (mm)	532	476
Projectile weight (kg)	8.17	5.5
Muzzle exit velocity (m/s)	1427	1700
Target range (m)	3000	2500

Table 3. Properties for 7075 T-6 aluminum and steel.

Property	Aluminum	Steel
Density (kg/m^3)	2810	7800
Tensile strength (MPa)	503	n/a
Modulus (GPa)	71.7	200
Poisson's ratio	0.33	0.29
Thermal conductivity ($\text{W/m}^*\text{K}$)	130	50
Specific heat ($\text{J/kg}^*\text{K}$)	960	500

7.1 Thermal Analysis

The thermal analysis was performed on a 2-D model using axisymmetric elements. The applied temperatures and the properties of the tailcone are axisymmetric. PLANE 55 element is used for 2-D thermal analysis; it can be used as either a plane element or axisymmetric. Also, it has provision for thermal conduction. PLANE 55 consisted of four nodes with a single degree of nodal freedom, i.e., temperature (15).

7.1.1 In-Bore Conditions

The initial conditions for the in-bore conditions are plotted in figure 18. For this analysis, the boundary conditions applied were a temperature of 1980 K for 6 ms. The tailcone had an initial temperature of 300 K, which increased as the temperature was conducted from the outer layer inward. In the thermal environment, the analysis is conducted taking into account not only the

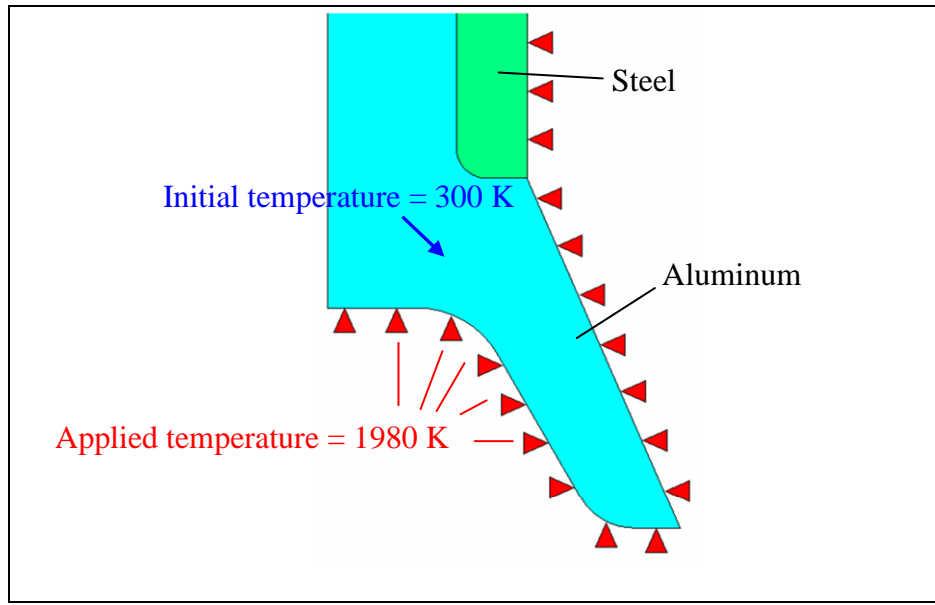


Figure 18. Initial conditions for the in-bore thermal analysis of the aluminum tailcone.

part to be analyzed, but also the surrounding component (such as the mating steel and/or aluminum). The reason for this is that in a thermal analysis, the temperatures of the surfaces in contact (steel and aluminum) are not known. These temperatures can only be known if the thermal properties of the surrounding material (steel) are known, and the analysis is conducted by incorporating these properties. Hence the results are given for the tailcone and its surrounding material.

The results for a transient analysis (for 6 ms) are shown in figure 19. This figure shows the influence of aluminum and steel thermal properties on the thermal conduction in the tailcone. While in the steel, the region affected by a temperature higher than 600°C (873 K) is 0.6 mm deep; in the aluminum, it is 0.8 mm. In the aluminum, the 0.8-mm region would soften or melt because of the temperature, while a 0.6-mm affected zone occurs in the steel. This analysis is performed under the supposition that there are no thermal protective coatings applied to the tailcone, and bare metal is exposed.

7.1.2 Out-of-Bore Condition

The high-velocity motion of the projectile induces a significant thermal load resulting from frictional drag in air. In previous work (16), it has been shown that for an M865 tailcone, the temperature of the airborne projectile can reach ~ 550 K. One of the requirements for the projectile is to survive for 5 s, which represents an ~ 8000 -m flight trajectory. Any tailcone material will need to endure this criterion in order to be a successful candidate for substitution in projectile applications.

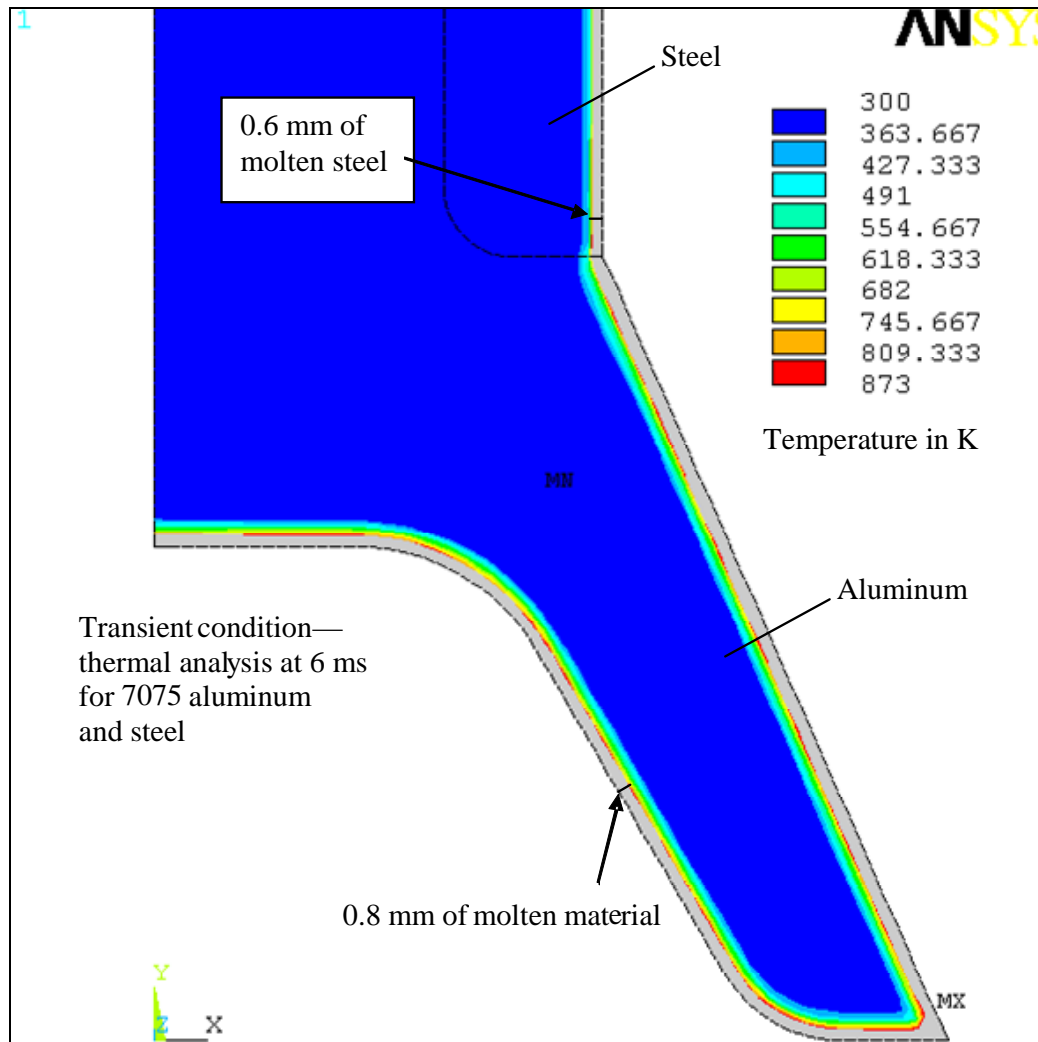


Figure 19. Transient thermal in-bore analysis for the steel and aluminum parts. The 0.8 mm of temperature-affected molten material is shown.

For the XM-1002, investigation into in-flight temperature has not been reported. Therefore, in order to evaluate potential candidate materials, the assumption of thermal loadings approximately equivalent to the M865 condition of 550 K was taken. This is believed to be a conservative case, in part because the XM-1002 is designed for a slower in-flight velocity.

The results from the in-bore analysis were set as the initial conditions for the out-of-bore analysis. The initial conditions are plotted in figure 20. For this case, the temperature was not applied to all the outer faces of the tailcone, but only to the face that is in contact with the high-speed air that causes the temperature rise.

Figure 21 shows typical results for 5 s into the flight. The arm of the tailcone has a temperature greater than 523 K after 5 s. This is due to the high thermal conduction of aluminum. This figure also contrasts the temperature profiles of the aluminum in comparison to steel.

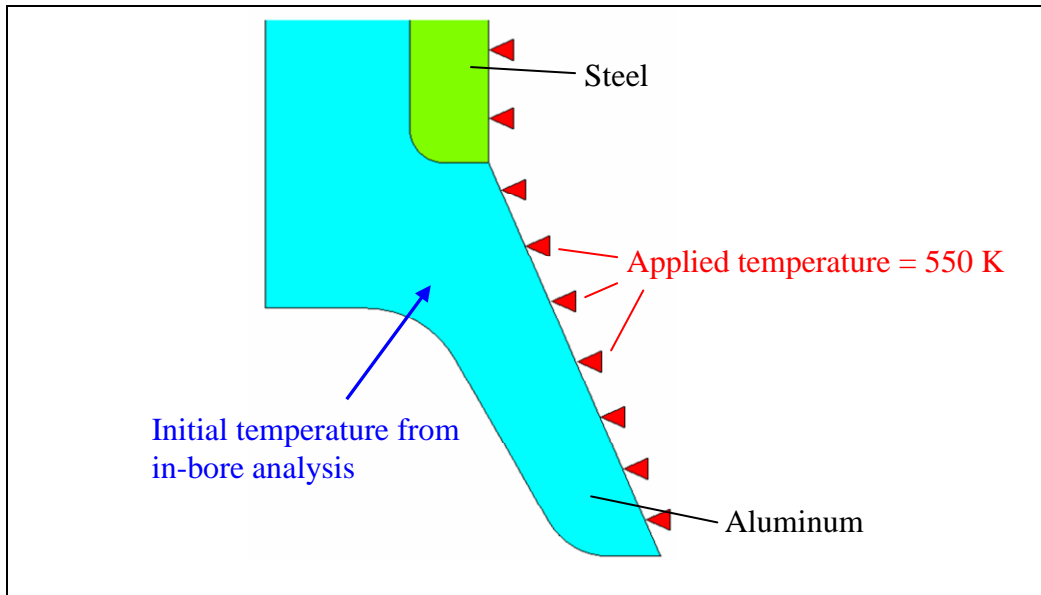


Figure 20. Initial conditions for the out-of-bore thermal analysis of the aluminum tailcone. In this case, the temperature is only applied to the outer part of the tailcone, which is in direct contact with the flowing air.

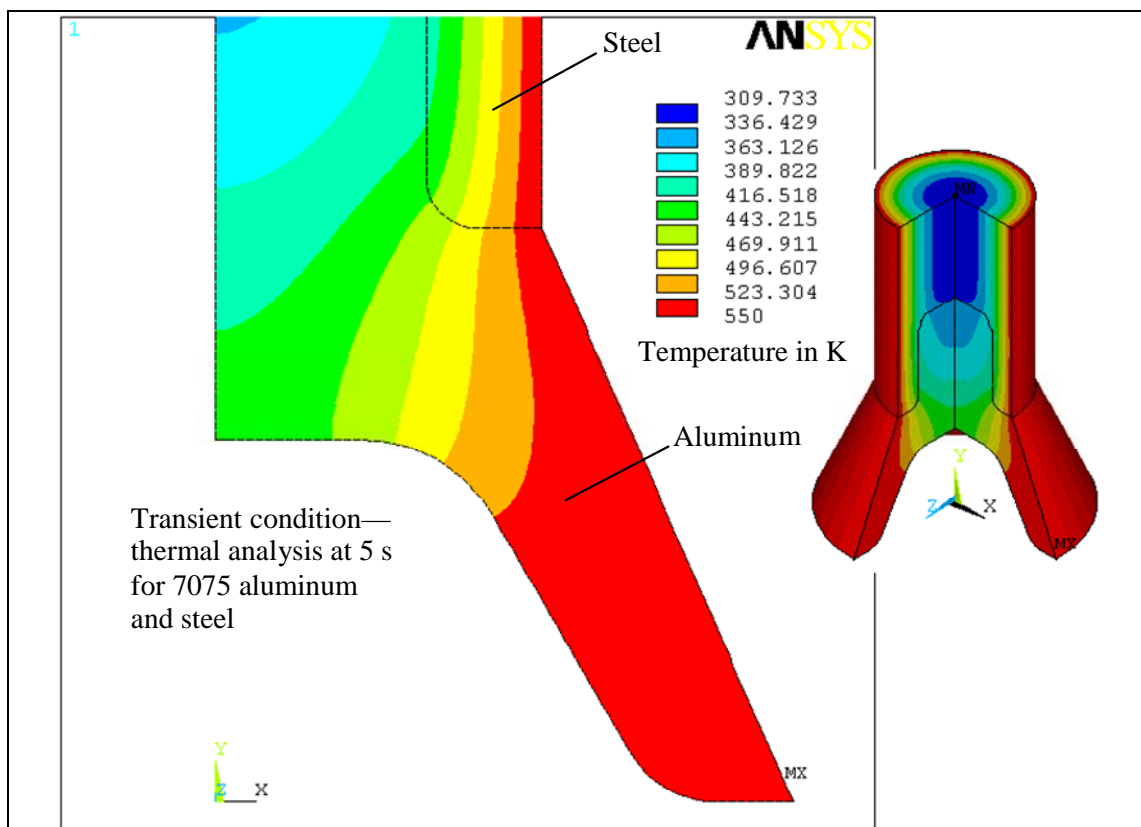


Figure 21. Transient thermal out-of-bore analysis for the steel and aluminum parts. The 3-D temperature visualization is presented to provide a better understanding of the material response.

Although 550 K (277 °C) is not high enough to cause the aluminum to melt, this analysis shows how aluminum reacts to the applied outer temperature. Later in the report, these results will be compared to the results for the LFT composite tailcone.

7.2 Structural Analysis

The structural analysis was also done using a 2-D analysis. Because the tailcone is axisymmetric (in geometry, loads, material properties, and boundary conditions), a half-cell 2-D model was used instead of a 3-D model (15). The type of element used for this analysis was PLANE 42. The PLANE 42 element is used for 2-D modeling of solid structures. The element can be used either as a plane element (plane stress or plane strain) or as an axisymmetric element. It is defined by four nodes that have 2 degrees of freedom at each node (translations in the nodal x and y directions). The element has plasticity, creep, swelling, stress-stiffening, large-deflection, and large-strain capabilities.

For the analysis, the von Mises stresses are plotted. The von Mises criterion is used because the material is ductile (13). The von Mises results are then compared to the yield stress, and any region that has a value of stress greater than the yield stress of the material is considered failed.

The safety factor used in the analysis is defined by

$$n = \frac{\sigma_{vonMises}}{\sigma_{yield}}, \quad (3)$$

where

n = safety factor,

$\sigma_{von Mises}$ = von Mises stress, and

σ_{yield} = yield stress for the material.

For the safety factor, any region with a value higher than 1 is considered failed.

7.2.1 In-Bore Conditions

The in-bore initial conditions can be observed in figure 22. This figure shows an axisymmetric view of the tailcone, in which the displacement constraints were set in the x and y directions, the pressures were 405.8 MPa applied over the outer lines, and the gravitational load was set as an inertia load (acceleration) of 434,061 m/s².

After running a static (steady state) analysis on the geometry (this is done assuming the material is not strain-rate dependent), the results were obtained and plotted in figure 23. From this figure, all stresses are seen to lie within the yield stress of the material. The maximum stress is 321 MPa, which is under 503 MPa, the yield stress. This gives a safety factor of 0.64.

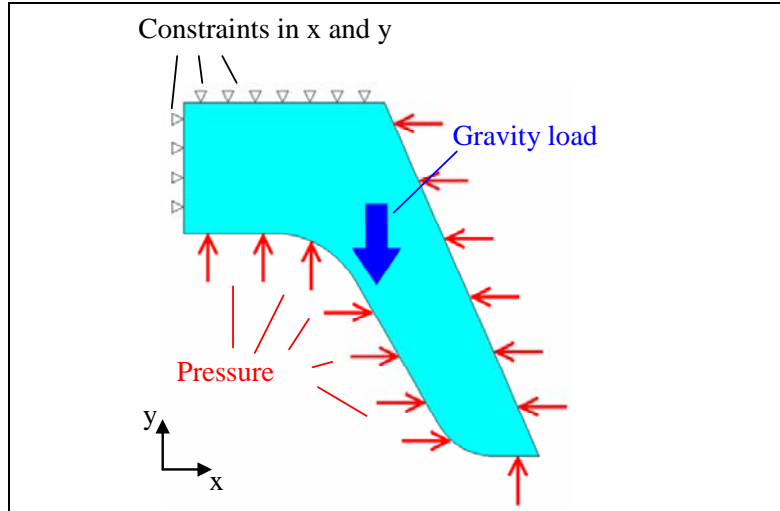


Figure 22. Initial conditions for the in-bore structural analysis of the aluminum tailcone.

The region of maximum stress is at the top outer part of the tailcone. The constraints in this region cause this high stress. These constraints are applied to simulate the action of the steel projectile on the tailcone. The steel projectile impedes the movement of the tailcone in the +y direction.

7.2.2 Transition Condition

The initial conditions for the transition condition are shown in figure 24. These conditions are similar to those used for the in-bore analysis. In this case, there is no acceleration load, and the applied pressure is 65 MPa (compared to 405.8 MPa for the in-bore initial conditions), and this pressure is only applied to the bottom part of the geometry.

Structural analysis was used to determine which state, between acceleration or no acceleration, would cause larger stresses in the tailcone. Applying acceleration to the initial conditions lowered the stresses in the tailcone (figures 25 and 26). This happens because the direction of the acceleration force is opposite to the force imposed by the pressure, reducing the stresses applied by the pressure differential. In this case, the worst case (no acceleration) was taken into account.

The results of this analysis can be observed in figure 25. The maximum stress is 1090 MPa. This gives a safety factor of 2.17. The failure occurs from high stresses encountered during the transition condition. To have a better perspective of the failure region, the results are represented as shown in figure 26. In this figure (plot), the stress scale is changed from 0 to 503 MPa, the yield stress of the material. From figure 26, it can be observed that although there is a very high stress concentration in the top right corner, the failed region is quite small. There are no other observable regions that could create additional failure paths. In other words, the failure region is highly localized.

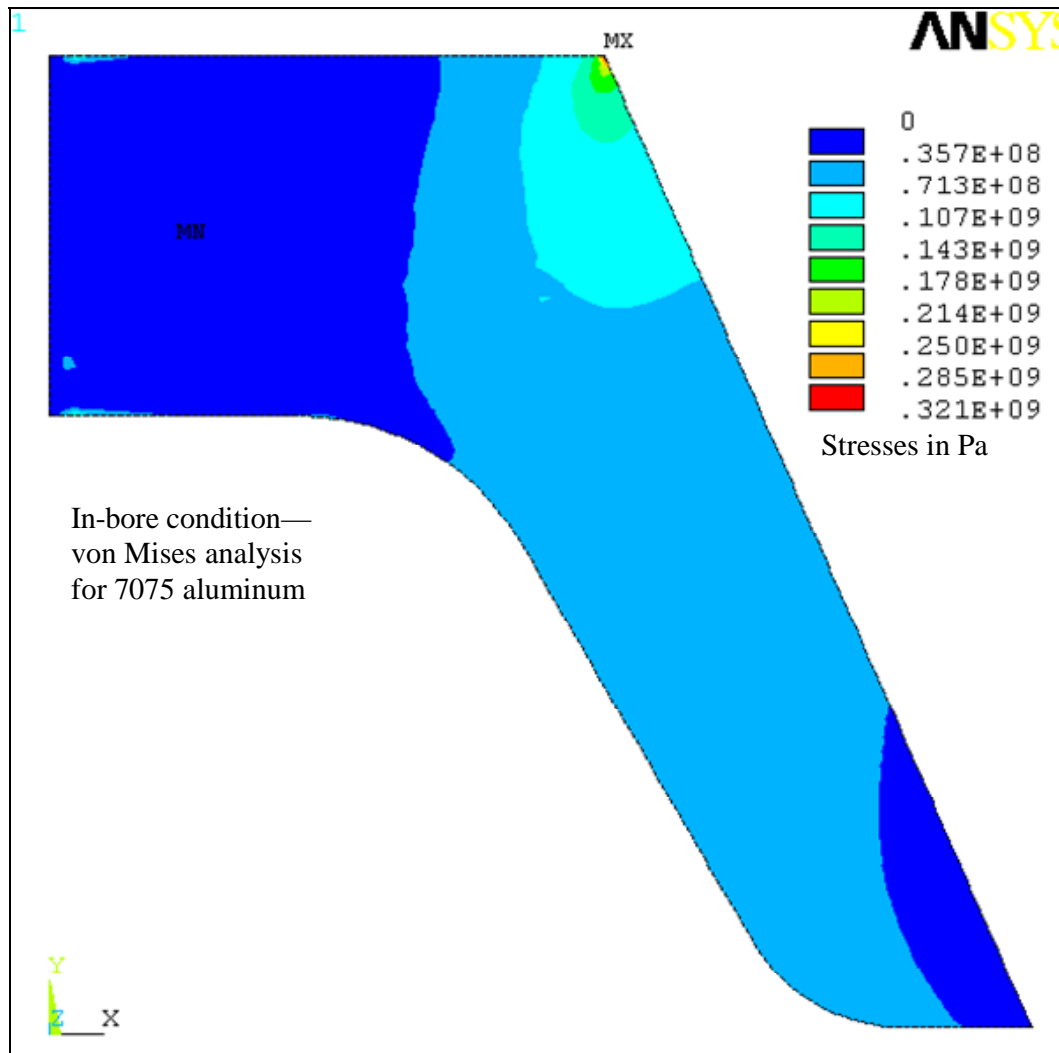


Figure 23. Von Mises stress plot for the 7075 aluminum tailcone at in-bore condition. The top-right part shows maximum stresses.

The local failure region is created by the compression caused by the pressure (acting at the bottom of the cone) (figure 27) and the steel projectile on the top (to which the tailcone is mated). This state of stress suggests that the real load caused by the pressure is higher than that caused by the acceleration for the in-bore condition. By observing the type of loading and its location—and the fact that while the pressure is acting mostly in the +y direction and the acceleration in the -y direction—it can be concluded that the pressure is the dominating factor.

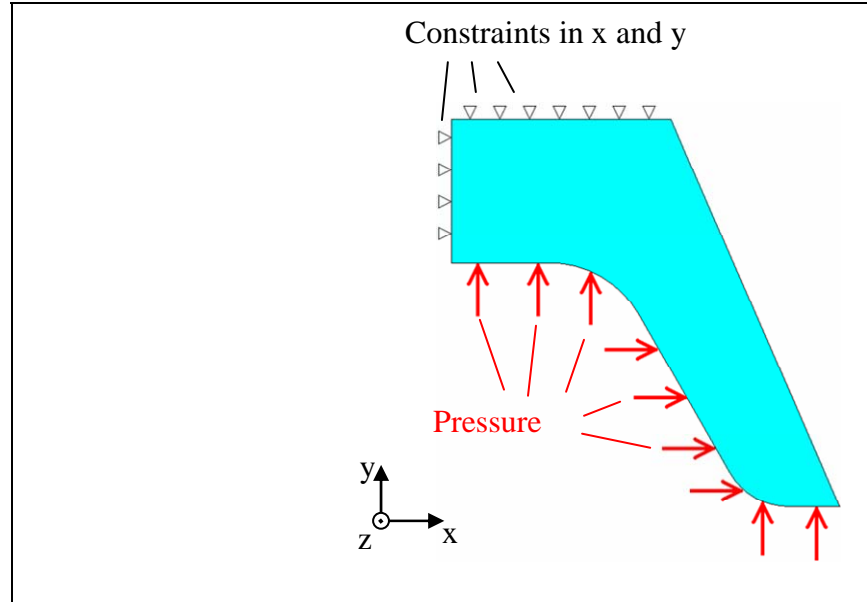


Figure 24. Initial conditions for the transition regime structural analysis of the aluminum tailcone.

8. Hollow-Back LFT Tailcone

One of the main concerns when developing the tailcone with the LFT composite material is its change in weight (mass). The center of gravity in a projectile is an essential element to performance. Adding or subtracting weight to the tailcone can cause stability problems, thus causing out-of-plane rotation in the y or z axis. Maintaining the same weight (as the all-aluminum version) of the tailcone was desirable. This issue was addressed by using a metal insert.

The threaded insert (made of aluminum) mates the LFT tailcone to the projectile. The interface between the metal insert and the LFT material was a significant design feature. An optimum geometry had to be designed to account for the interface stresses from the interaction between the tailcone and the insert. It was critical that the part retained its integrity (i.e., no separation between the insert and the surrounding LFT material). Two metal insert geometries were explored, beaded and threaded. For the hollow-back version, two geometries were explored depending upon the metal insert geometry. The details of the tailcone manufacturing are reported elsewhere (17).

8.1 Thermal Analysis

Thermal analysis was performed for the LFT material for the in-bore and out-of-bore conditions, respectively. The same type of material model was used (PLANE 55) under identical initial conditions as was used for the aluminum tailcone analysis.

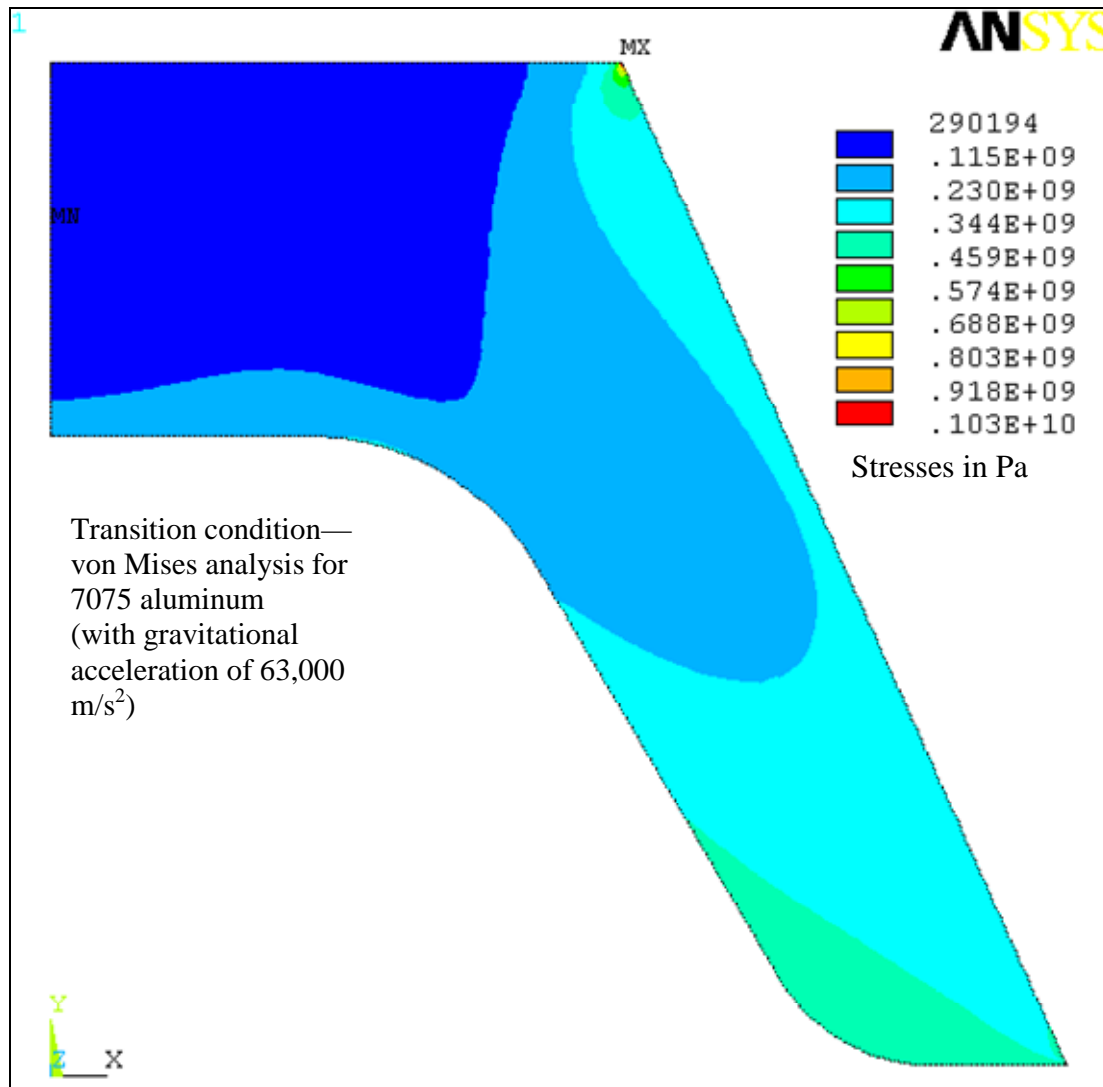


Figure 25. Von Mises stress plot for the 7075 aluminum tailcone at transition condition (acceleration of 63,000 m/s² in the -y direction). The maximum applied stress is 1030 MPa and is located in the top-right corner.

8.1.1 In-Bore Condition

The initial conditions for the LFT tailcone are shown in figure 28. These are the same initial conditions as the ones used for the pure aluminum tailcone. The difference in this analysis is that two additional interfaces are introduced, the LFT-aluminum and the LFT-steel insert.

The results for the transient in-bore thermal simulation are shown in figure 29. From this plot, it can be observed that although the critical temperature for the LFT is lower than for aluminum, the lower thermal conductivity compensates for this. While in the aluminum tailcone, without thermal protection, the molten region was 0.8 mm. In the LFT, this region is only 0.4 mm.

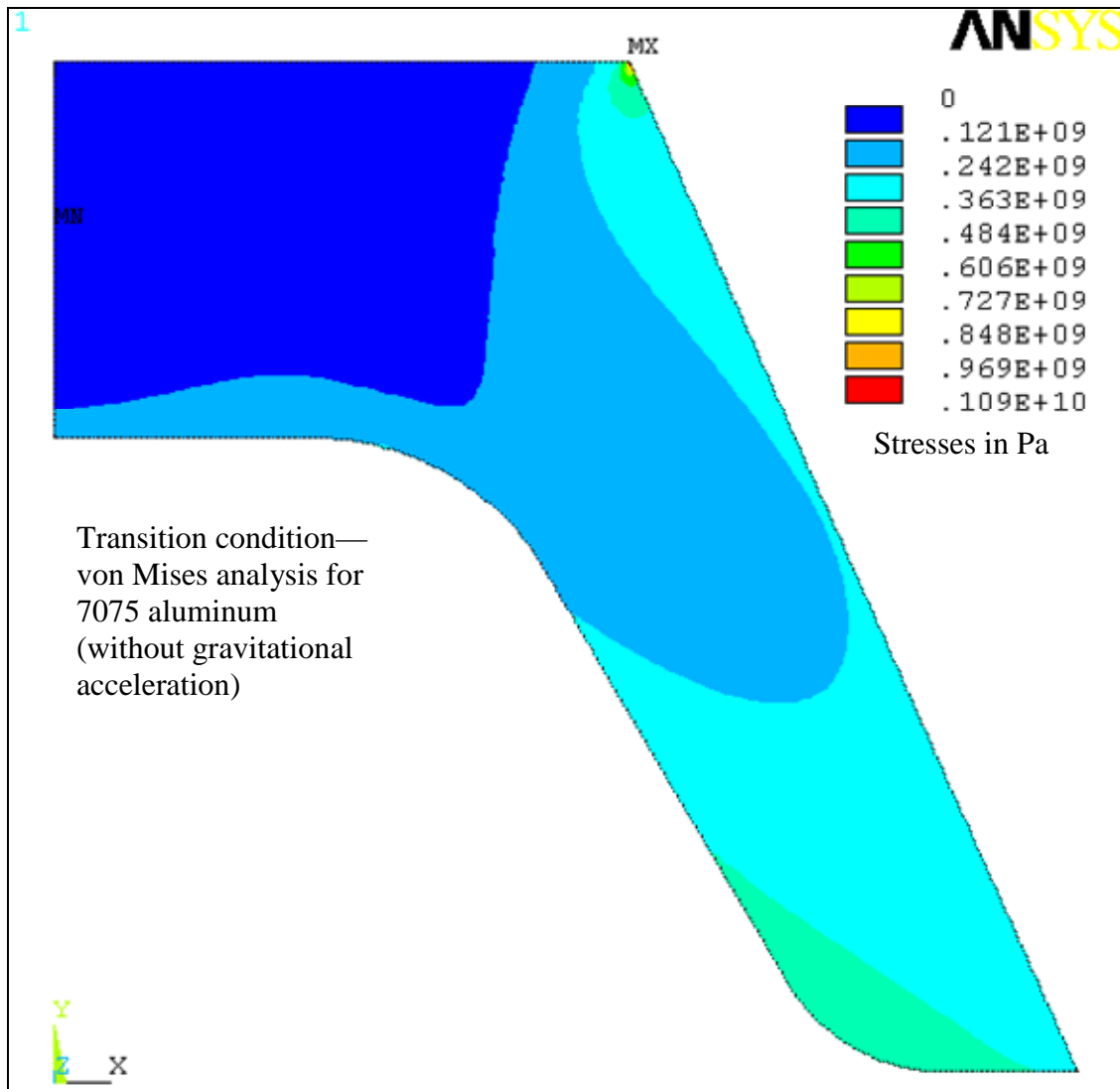


Figure 26. Von Mises stress plot for the 7075-T6 aluminum tailcone at transitions regime. The maximum applied stress is 1090 MPa (6% higher than the case with acceleration) and is located at the top-right corner.

8.1.2 Out-of-Bore Conditions

For this analysis, the results from the in-bore condition were used as input for the out-of-bore condition. Identical loading as in the aluminum case was applied. The applied initial conditions are shown in figure 30.

The results of this simulation are shown in figures 31 and 32. Figure 31 shows the highest temperature observed at the 5-s time interval. Figure 32 shows the detail of these temperatures but with the maximum temperature (on scale) being 570 K (the melting point of LFT). A temperature concentration region is located in the inner shoulder of the tailcone (figure 31). This can be explained as follows. At the first time step in the out-of-bore analysis, the 1980 K (which is the applied temperature for the in-bore condition) was applied to the surface. The negative

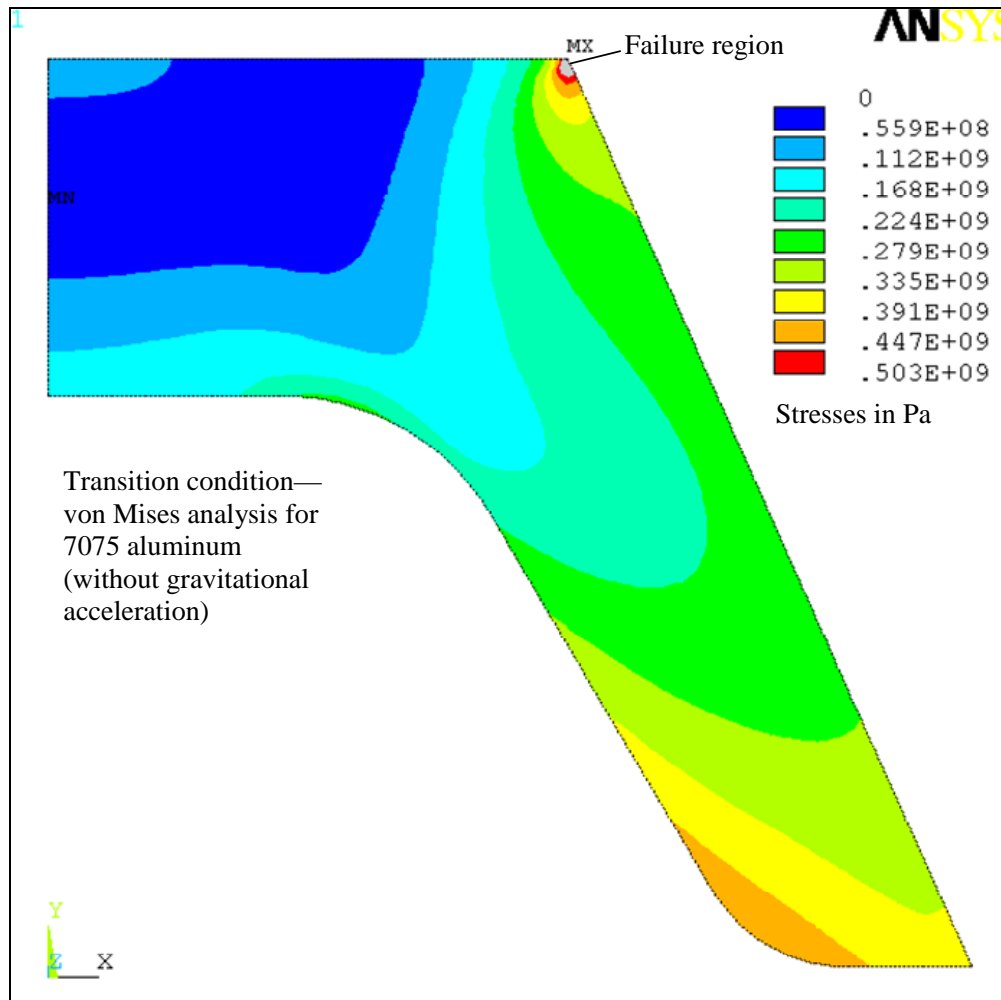


Figure 27. Detail of the von Mises stress plot. The scale is changed so the maximum stress shown is the yield stress. Any stress higher than the yield strength is shown as a gray region.

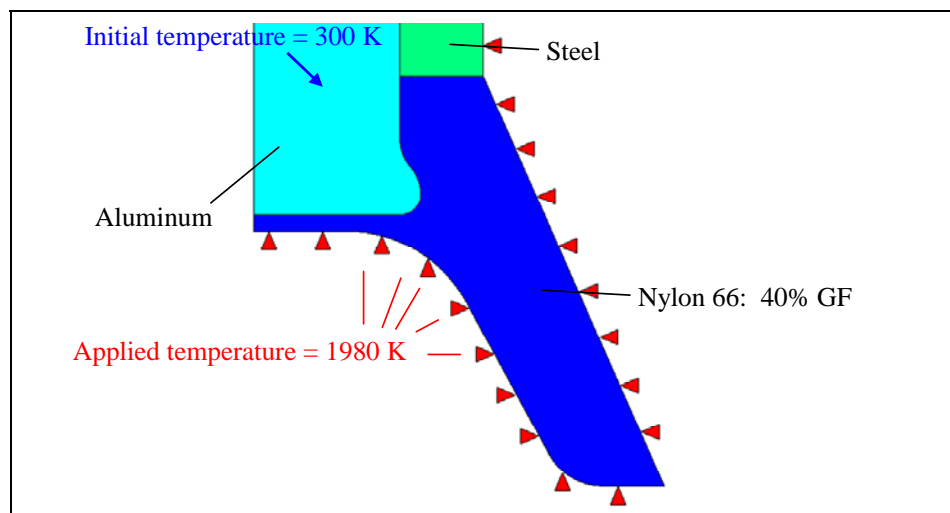


Figure 28. Initial conditions for the in-bore analysis of the LFT tailcone.

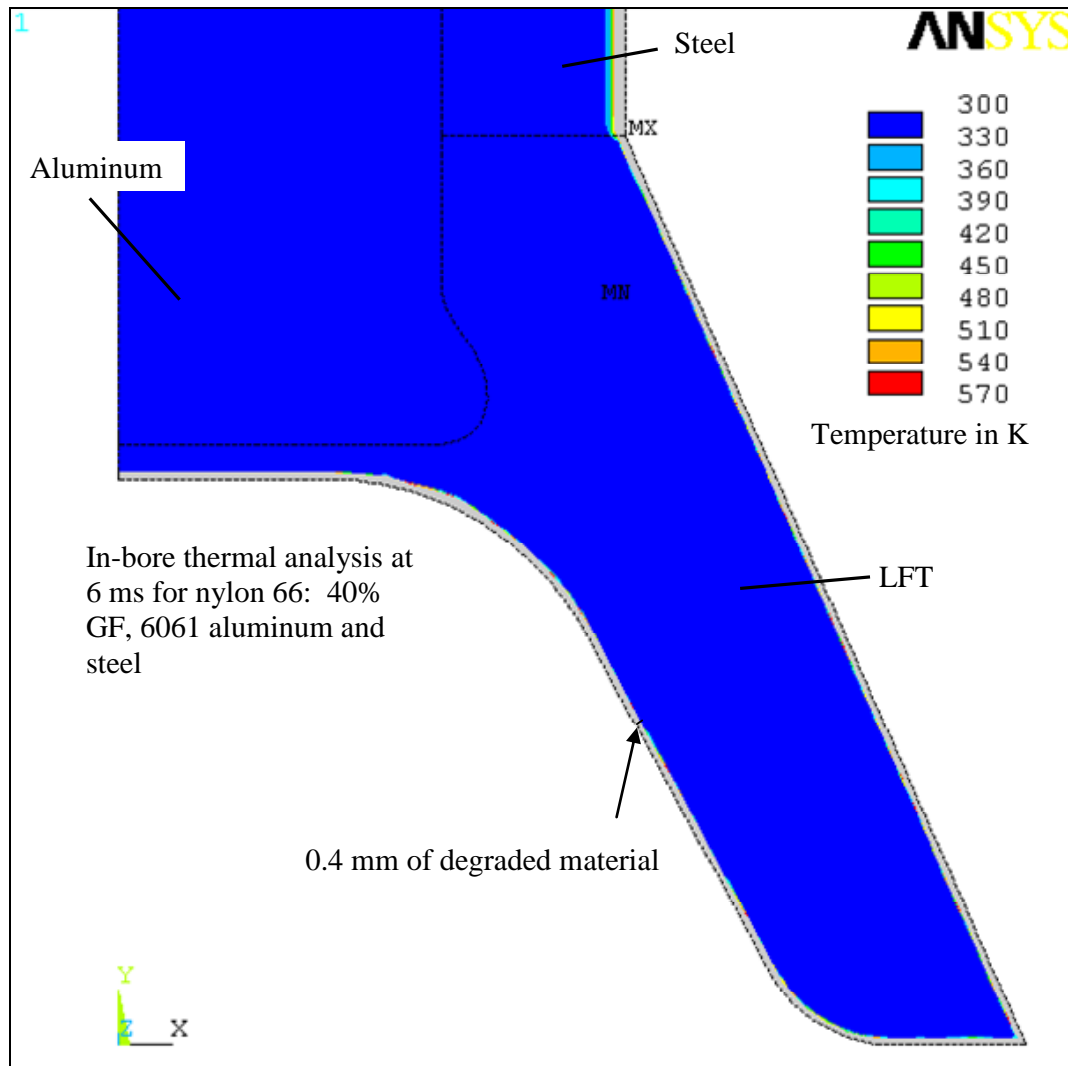


Figure 29. In-bore thermal analysis for the LFT, steel, and aluminum parts. In this case, only 0.4 mm of heat-affected material is observed.

concavity of this region signifies a temperature concentration on the LFT material. Although the temperature for the out-of-bore analysis (550 K) is below the melting temperature of the LFT, the 1980 K that was applied at the in-bore conditions still has an effect on the geometry even after the outer temperature is at 550 K.

The insert geometry (i.e., threaded vs. beaded) has no effect on the results. The critical temperature is a result of the thermal conduction of the air-to-LFT interface, not from the metal-to-LFT interface. The thermal results were the same for the threaded and beaded inserts.

8.2 Structural Analysis

PLANE 42 was used for the structural analysis of the LFT tailcone, which is the same type of element used for the aluminum tailcone. The same axisymmetric conditions were applied.

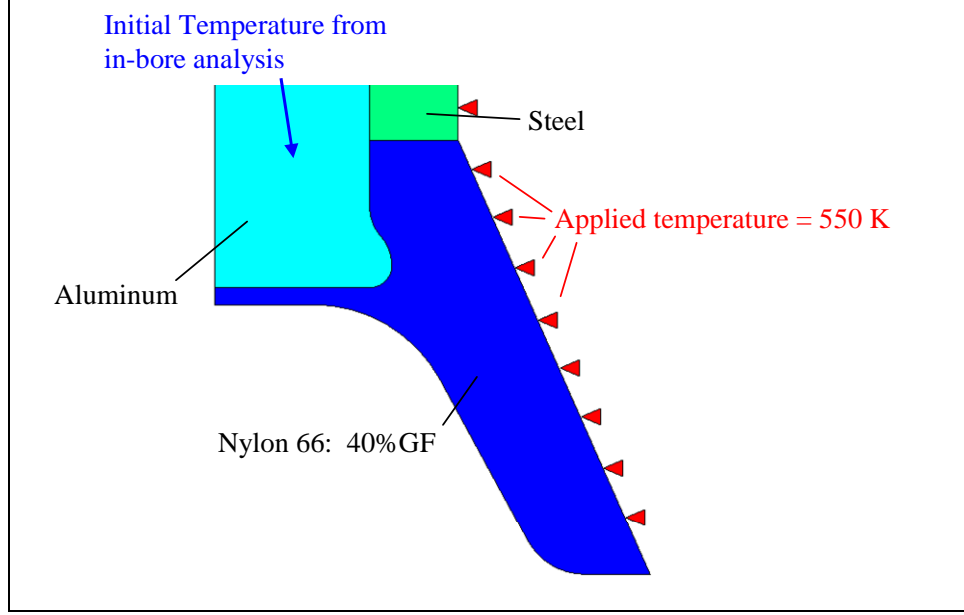


Figure 30. Initial conditions for the tailcone in out-of-bore conditions. The conditions from the in-bore analysis were used as the initial temperature.

For the LFT tailcone, the failure mechanisms considered are fiber fracture, matrix failure, interfacial failures, and buckling. The Tsai-Wu criterion evaluates the survival of the composite in an overall sense. For this analysis, the Tsai-Wu failure criterion was used. It is well known that Tsai applied this failure criterion to unidirectional, laminated composites that had different properties in the longitudinal and transverse directions (18).

For the case of the LFT tailcone, the properties are not directionally tailored as for a laminated composite. However, there is anisotropy due to preferential fiber distribution inherent to the compression molding of the LFT material. The properties also change when the material is loaded under tension or compression. A 15% improvement was found in the compressive strength compared with the tensile strength for nylon 66 with 40% glass fiber (19, 20). Hence the use of the Tsai-Wu criterion was justified in the present work.

The failure criterion used in ANSYS is a 3-D version of the Tsai-Hill 2-D. The Tsai-Hill 2-D criterion states that (15, 18)

$$F_{xx}\sigma_x^2 + 2F_{xy}\sigma_x\sigma_y + F_{yy}\sigma_y^2 + F_{ss}\sigma_s^2 + F_x\sigma_x + F_y\sigma_y = \xi_1, \quad (4)$$

where

$$F_{xx} = \frac{1}{X^t X^c}, \quad (5)$$

$$F_{yy} = \frac{1}{Y^t Y^c}, \quad (6)$$

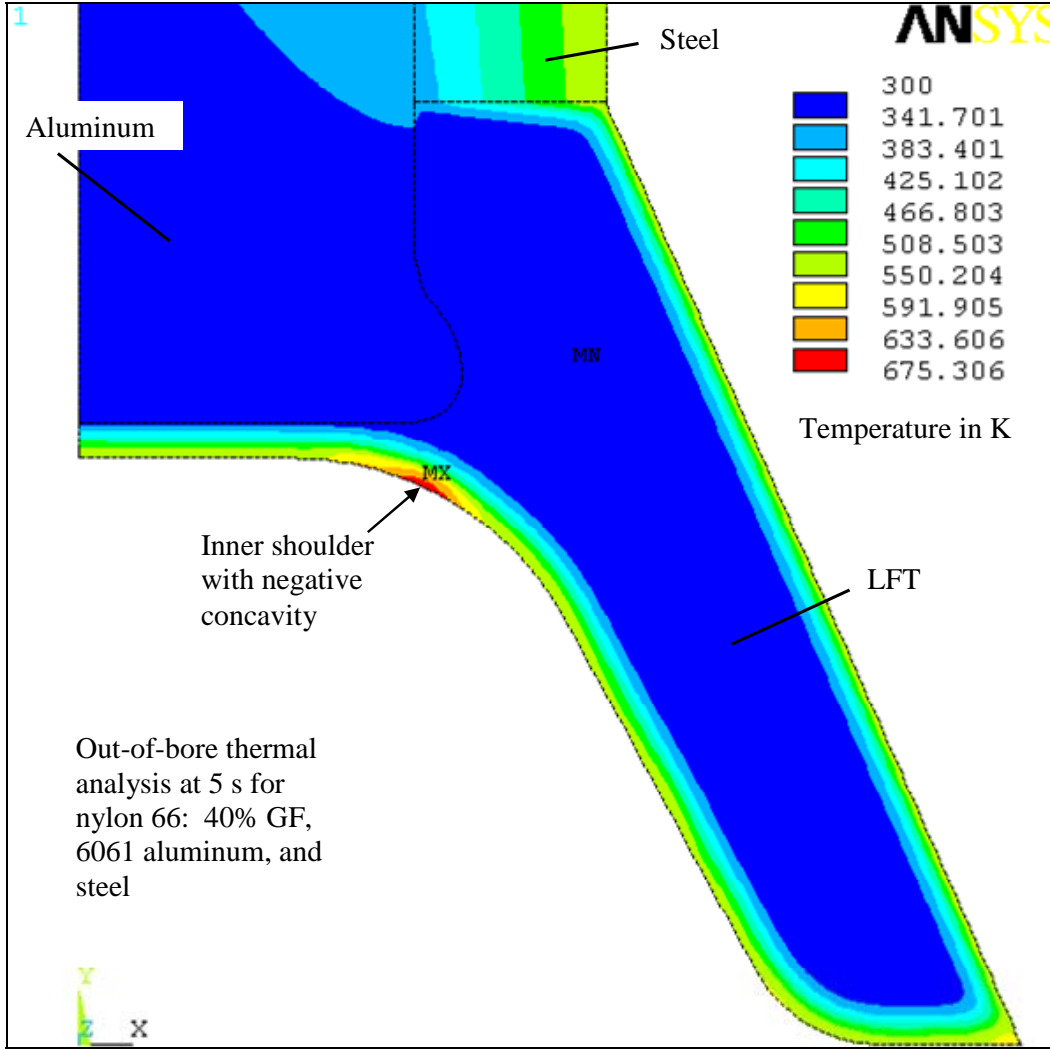


Figure 31. Out-of-bore thermal analysis for the LFT, steel, and aluminum parts. The maximum applied temperature at 5 s is 675 K. In this case, the shoulder acts as a heat sink.

$$F_x = \frac{1}{X^t} - \frac{1}{X^c}, \quad (7)$$

$$F_y = \frac{1}{Y^t} - \frac{1}{Y^c}, \quad (8)$$

$$F_{ss} = \frac{1}{S^2}, \quad (9)$$

and

$$F_{xy} = -\frac{\sqrt{F_{xx} + F_{yy}}}{2}, \quad (10)$$

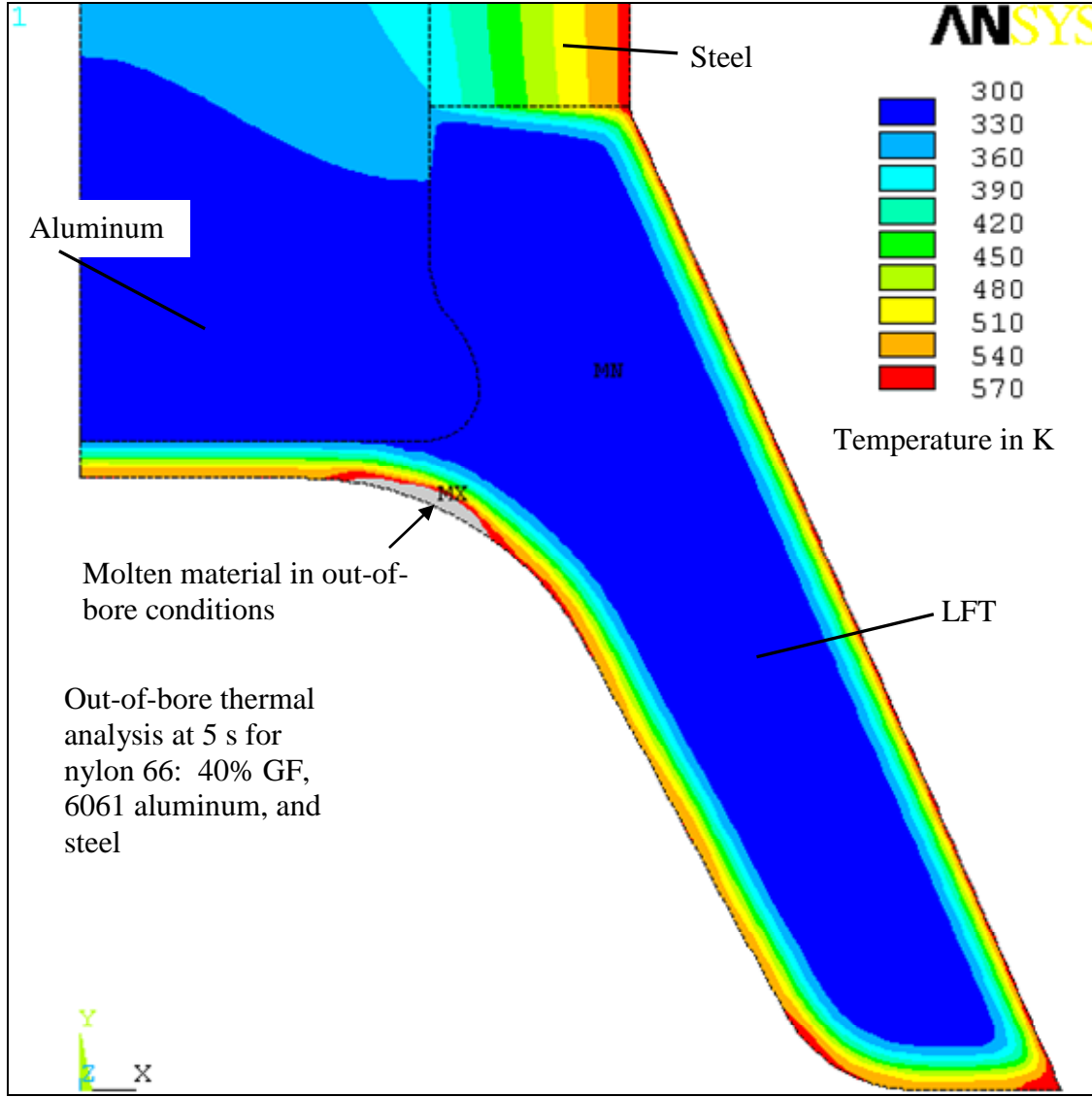


Figure 32. Detail of out-of-bore thermal analysis for the LFT, steel, and aluminum parts. The maximum temperature on the scale is 570 K, which is the melting temperature for the LFT.

where

σ_x and σ_y = applied stresses in x and y,

σ_s = applied shear stress,

X^t and Y^t = tensile strength in x, y, and z,

X^c and Y^c = compressive strength in x, y, and z,

S = shear strength in the xy plane, and

ξ_I = value of Tsai-Hill criterion.

ANSYS uses the strength ratio as a form of Tsai-Wu failure criterion in a 3-D version of the Tsai-Hill 2-D criterion in which

$$\xi_2 = \frac{1}{-\frac{B}{2A} + \sqrt{\left(\frac{B}{2A}\right)^2 + \frac{1}{A}}}, \quad (11)$$

where

$$A = -F_{xx}\sigma_x^2 - F_{yy}\sigma_y^2 - F_{zz}\sigma_z^2 + \frac{\sigma_{xy}^2}{S_{xy}^2} + \frac{\sigma_{yz}^2}{S_{yz}^2} + \frac{\sigma_{xz}^2}{S_{xz}^2} - \sqrt{F_{xx}F_{yy}}\sigma_x\sigma_y - \sqrt{F_{xx}F_{zz}}\sigma_x\sigma_z - \sqrt{F_{yy}F_{zz}}\sigma_y\sigma_z \quad (12)$$

and

$$B = \left(\frac{1}{X^t} + \frac{1}{X^c}\right)\sigma_x + \left(\frac{1}{Y^t} + \frac{1}{Y^c}\right)\sigma_y + \left(\frac{1}{Z^t} + \frac{1}{Z^c}\right)\sigma_z, \quad (13)$$

where

σ_x , σ_y , and σ_z = applied stresses in x, y, and z,

σ_{xy} , σ_{yz} , and σ_{xz} = applied shear stress in the planes xy, yz, and xz,

X^t , Y^t , and Z^t = tensile strength in x, y, and z,

X^c , Y^c , and Z^c = compressive strength in x, y, and z,

S_{xy} , S_{xz} , and S_{yz} = shear strength in the xy, xz, and yz plane, and

ξ_2 = value of Tsai-Wu strength ratio.

8.2.1 Bonding Between Aluminum and Polymer

The preliminary microstructure analysis of the LFT tailcone (20) showed that the interface between the insert and the surrounding LFT material was highly polymer (nylon) rich (figure 33). Hence the study of the bonding between the aluminum and nylon polymer was deemed important. The bonding between these two materials has been studied in previous works (21, 22). From these studies, it can be concluded that the adhesion between the metal and the surrounding polymer is improved by using a bonding agent. These studies also show that a high degree of mechanical bonding can be enhanced if the surface roughness is improved (23, 24). In the present case, the interlocking mechanism provided by the threads provides the mechanical bond to the LFT material. In the tailcones manufactured in the present work, the surface of the aluminum was not treated, and no bonding agent was present, therefore no bonding was assumed in the following analysis.

8.2.2 In-Bore Conditions

As mentioned before, two different insert geometries (beaded and threaded) were considered.

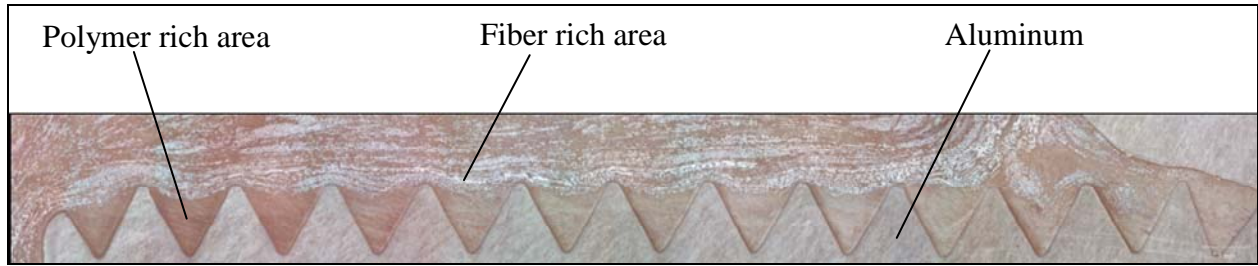


Figure 33. Section of the LFT-aluminum interface in the hollow-back threaded insert tailcone. There is a high concentration of nylon in the threads.

8.2.2.1 Beaded Insert Geometry. Both the beaded and the threaded insert geometries were subjected to the same applied loads to match the conditions witnessed by the aluminum tailcone in the transition zone. However, for the LFT tailcones, there is a metal insert (beaded or threaded). The boundary condition for the interface between the metal insert and the LFT material is an added set of constraints that are not present in the aluminum tailcone, because the latter is an isotropic monolithic material.

Figure 34 shows the initial loading conditions for the beaded geometry. In the LFT analysis, the polymer aluminum interface was treated as a no-bonded, frictionless interface in which the constraints were applied normal to the surface (referred to as normally constrained). This was an approximation of the actual conditions, because there is actually friction between the aluminum and the nylon that restricts the sliding movement between the two parts.

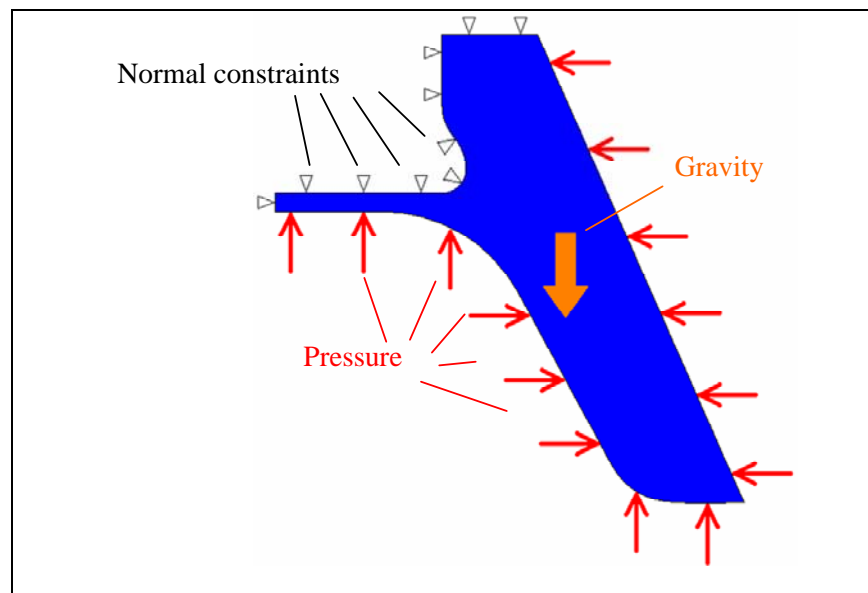


Figure 34. Initial conditions for the in-bore structural analysis of the LFT section of the beaded tailcone.

In the case of the beaded geometry, an analysis was conducted to observe the difference between having a fully constrained and a normally constrained geometry. From this analysis, it was observed that the normally constrained geometry showed higher applied stresses. In the field, the tailcone is subjected to a condition somewhere between the normal and the in-plane constraints due to the relative friction. Here, the results from only the normal constraints (conservative) are reported.

The results from this analysis are shown in figures 35 and 36. Figure 35 shows the maximum value of the Tsai-Wu failure criterion is 1.437. This means that this region fails by a factor of 0.437. As observed in figure 36, this is a small failure region, about 6%, of the LFT-aluminum interface. The region with the maximum stresses is at the location of the bead. In the vector displacement plot (figure 37), it can be observed that this region is a critical region where the LFT material tends to bifurcate in both directions. There is an equivalent tensile stress in this region as the material tends to fail by bifurcation, which is higher than the maximum stress for the material.

The highly stressed region seen in the LFT tailcone is also observed for the aluminum tailcone (figure 23). This region witnesses high stresses for the same reason as described for the aluminum tailcone. In this region, the steel projectile impedes the displacement of the LFT tailcone.

8.2.2.2 Threaded Insert Geometry. In this geometry, sharp corners are observed, which are constrained differently than a smooth surface as the one observed in the beaded insert geometry. Figure 38 shows a detail of the threaded insert section.

From figure 38, the normal constraints are observed in each of the threads. If the constraints are set all over the line (A), they will meet at the corners (C) with the adjacent constrained lines (B). The point where the two lines meet (C) has two constraints, the constraints being normal to each line. A point constrained in two directions in the same plane is the equivalent to being fully constrained (a sharp corner), so each of the nodes at corners such as C are fully constrained in x and y directions. These sharp corners are simulated as such because although in real life these corners have a radius, from a simulation point of view, these radii are too small and the elements near the corners have to be very small. Constraining these corners as fully constrained points is a good approximation to reality. Figure 39 shows the initial loading configuration for the threaded geometry at in-bore conditions.

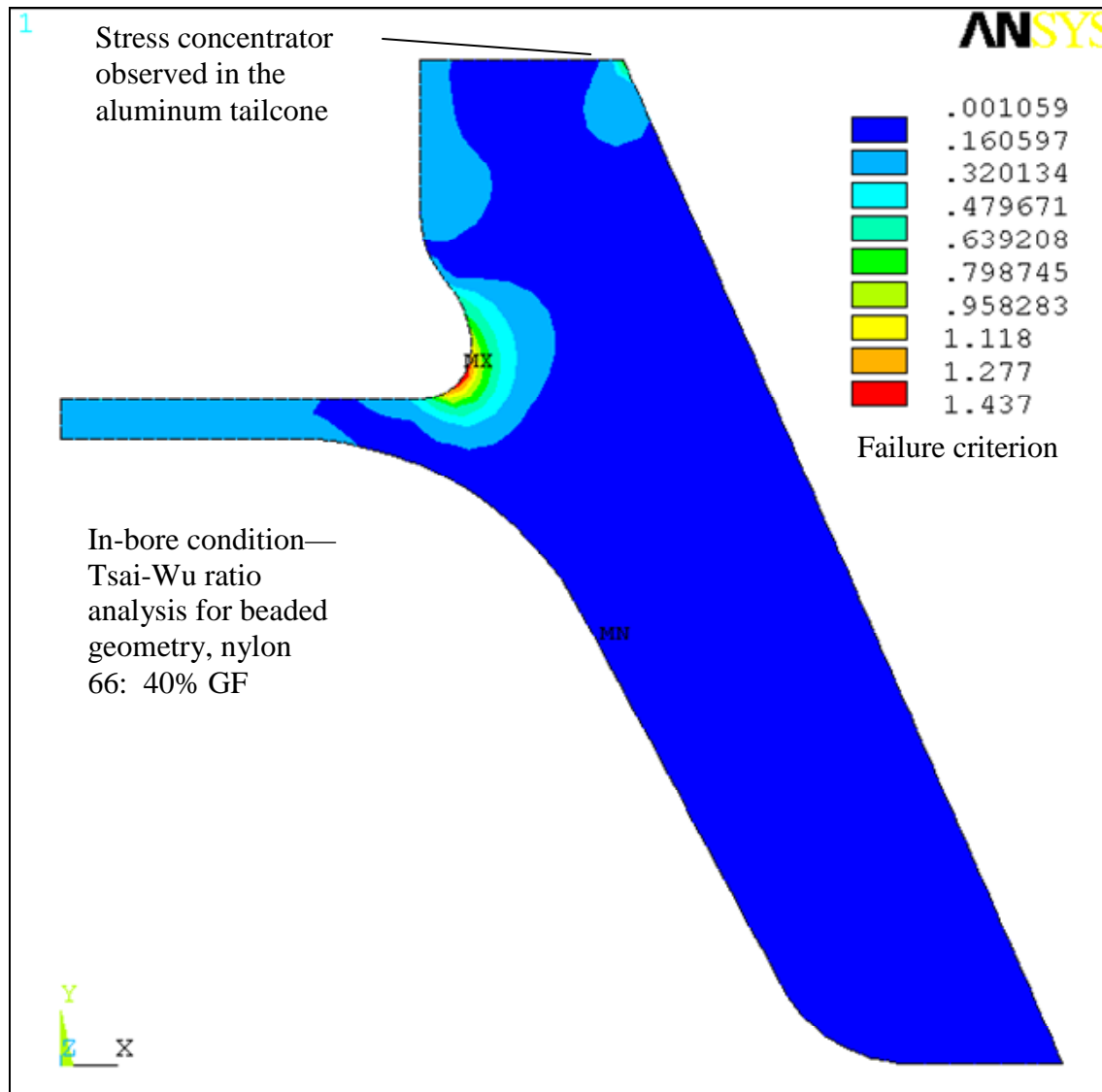


Figure 35. Tsai-Wu failure criterion plot for the beaded LFT section of the tailcone at in-bore conditions. The maximum value is 1.437 and is located at the edge of the bead. A stress concentrator, due to the presence of the steel projectile, is observed in the top-right corner of the tailcone.

The results of this analysis can be observed in figures 40 and 41. Figure 40 identifies the failure region for the in-bore conditions. The highest Tsai-Wu ratio for this condition was noted to be 1.247, which is 24.7% higher than the allowable limit. Still, this value of 24.7% for the threaded insert is lower than that for the beaded insert case. For the threaded insert, the failure region is not in the LFT-aluminum interface but is at the top-right corner, as seen in figure 41. As discussed for the beaded insert case, the highest stress occurs at the top-right corner because of the steel projectile that impedes the displacement of the LFT tailcone. The stresses in the threaded insert case are smaller than those in comparison to the beaded insert case because each

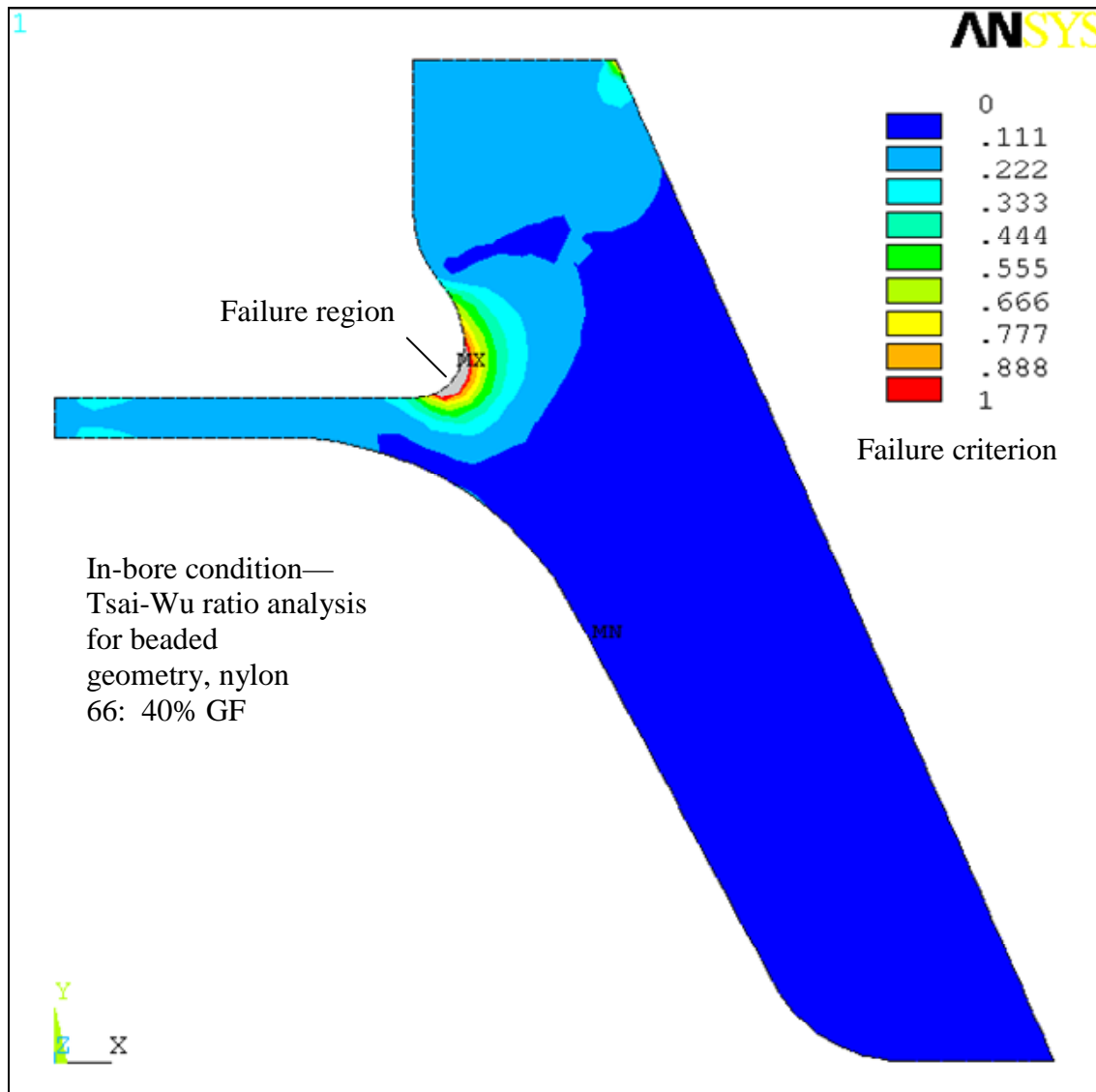


Figure 36. Detail of the Tsai-Wu failure criterion plot for the beaded LFT section of the tailcone at in-bore conditions. The failure region in the interface is 6% of the complete interface between the LFT and the aluminum insert.

one of the threads restricts the movement of the LFT material. This can be observed in figure 42 where, although the vector plot shows a relative movement between the two (i.e., the LFT and the insert), this movement is restricted because of the tortuous path created by the threads. Although every thread acts as a stress concentrator, it also helps restrict the relative movement between the LFT material and the insert.

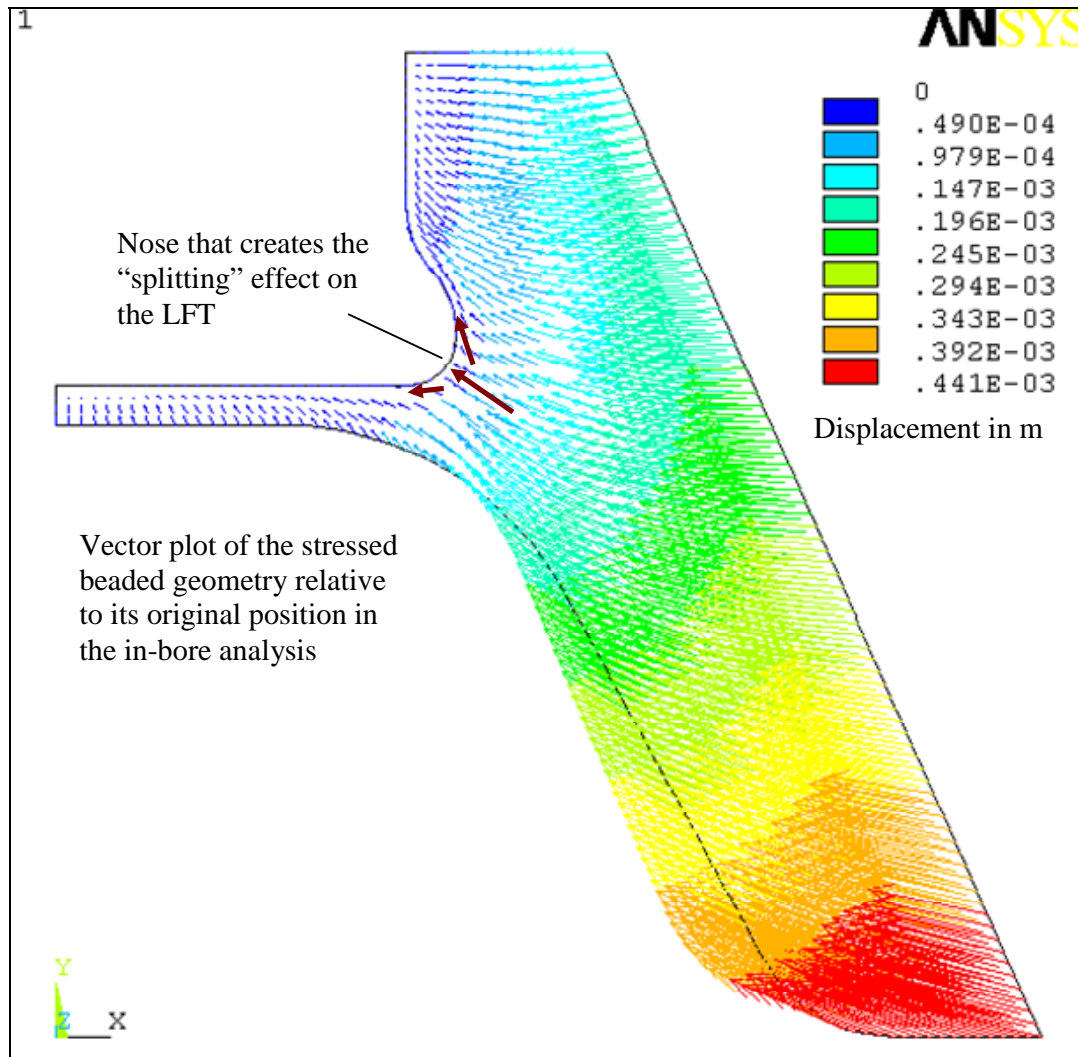


Figure 37. Vector plot that shows the displacement of the beaded LFT section of the tailcone comparing it to its original position. The bead acts as a “splitting” nose for the LFT.

From the in-bore analysis, the threaded insert geometry is a better design in terms of the stresses that are generated. The threads distribute the stresses more evenly throughout the interface (i.e., LFT to insert). The local stresses in the vicinity of the threads (figure 40) are higher than those observed for the vicinity of the bead (in the case of the beaded insert) (figure 35). Although the local stresses surrounding the threads (in the case of the threaded insert) are higher than the stresses surrounding the bead in the beaded insert, these are lower than the limiting value for failure.

8.2.3 Transition Condition

The boundary conditions for the beaded and threaded insert geometries were similar to those ones used for the in-bore conditions. The LFT metal-insert interface was analyzed to evaluate the constraints as they occur in reality.

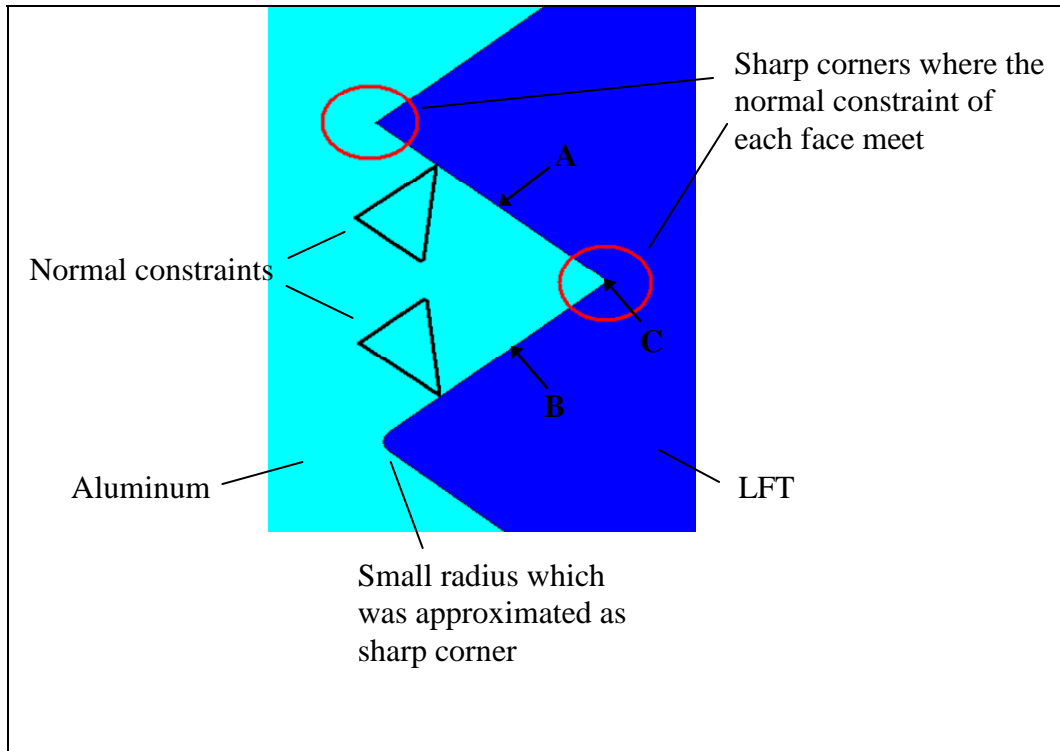


Figure 38. Detail of thread in LFT-aluminum interface. The small radius in each thread is approximated to be a sharp corner that is fully constrained.

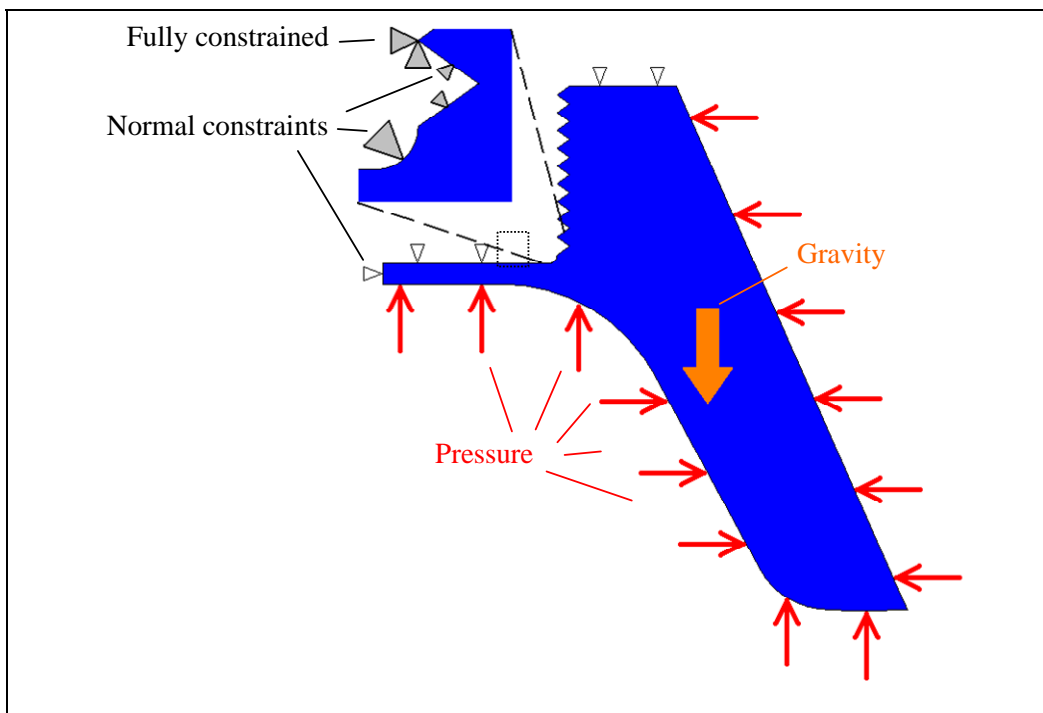


Figure 39. Initial conditions for the in-bore structural analysis of the LFT section of the threaded tailcone. The detail shows the threads as fully constrained at each corner.

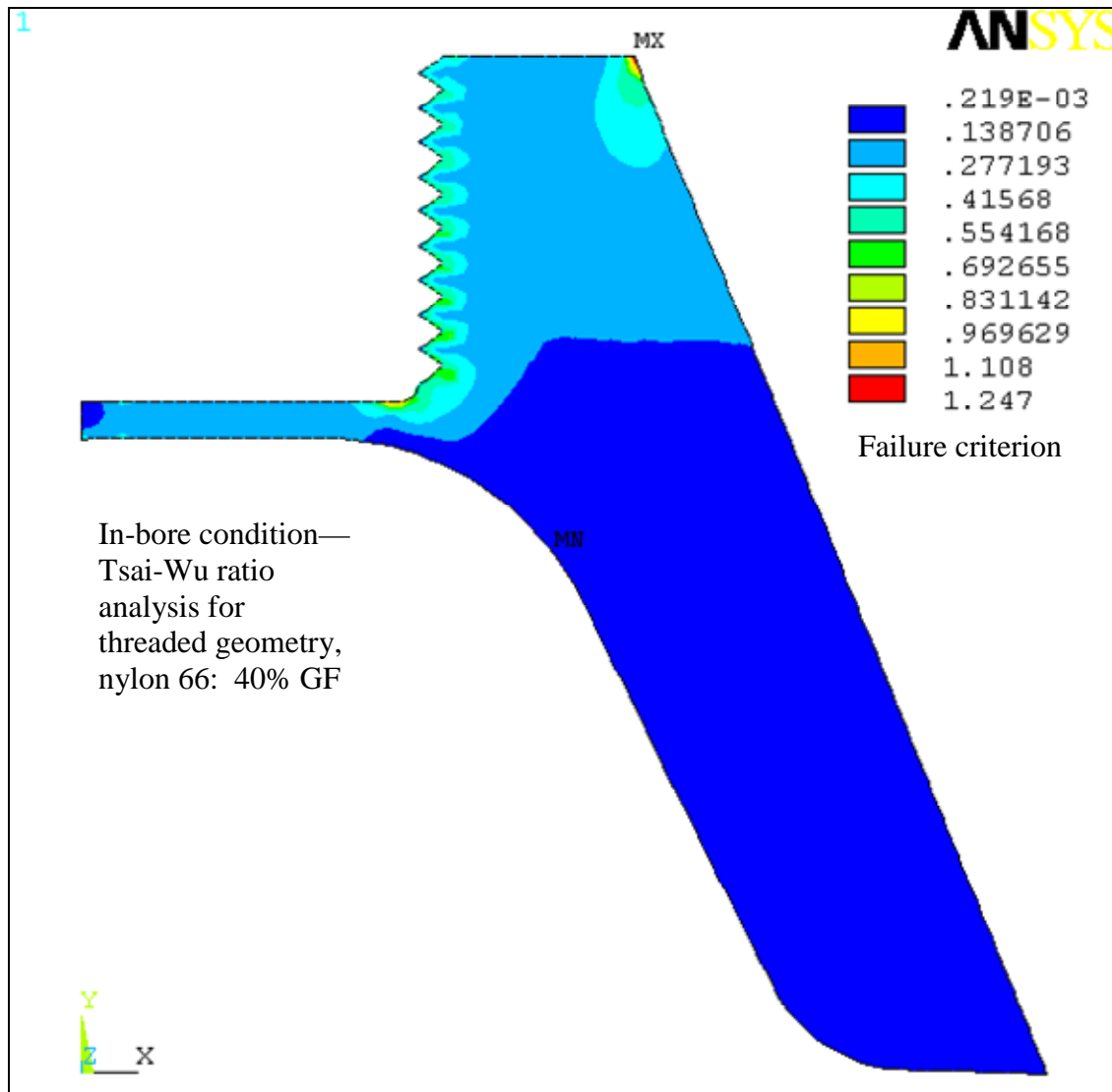


Figure 40. Tsai-Wu failure criterion plot for the threaded LFT section of the tailcone at in-bore conditions. The maximum value is 1.247 and is located at the top-right part of the tailcone due to the presence of the steel projectile in the top-right corner of the tailcone.

8.2.3.1 Beaded Insert Geometry. To determine the realistic constraints of the LFT material and the metal insert, the assumptions are (a) the LFT material is under compression and is being firmly pressed into the metal insert and (b) the LFT material is under tension and is being pulled away from the metal insert. For case (a), any compression between the metal insert and the LFT material (figure 43) is assumed to be a constraint for this analysis. For case (b), when the displacement of the LFT is away from the insert causing it to separate, the constraint has to be released in the analysis. This is because there is no actual bonding in the LFT-aluminum interface.

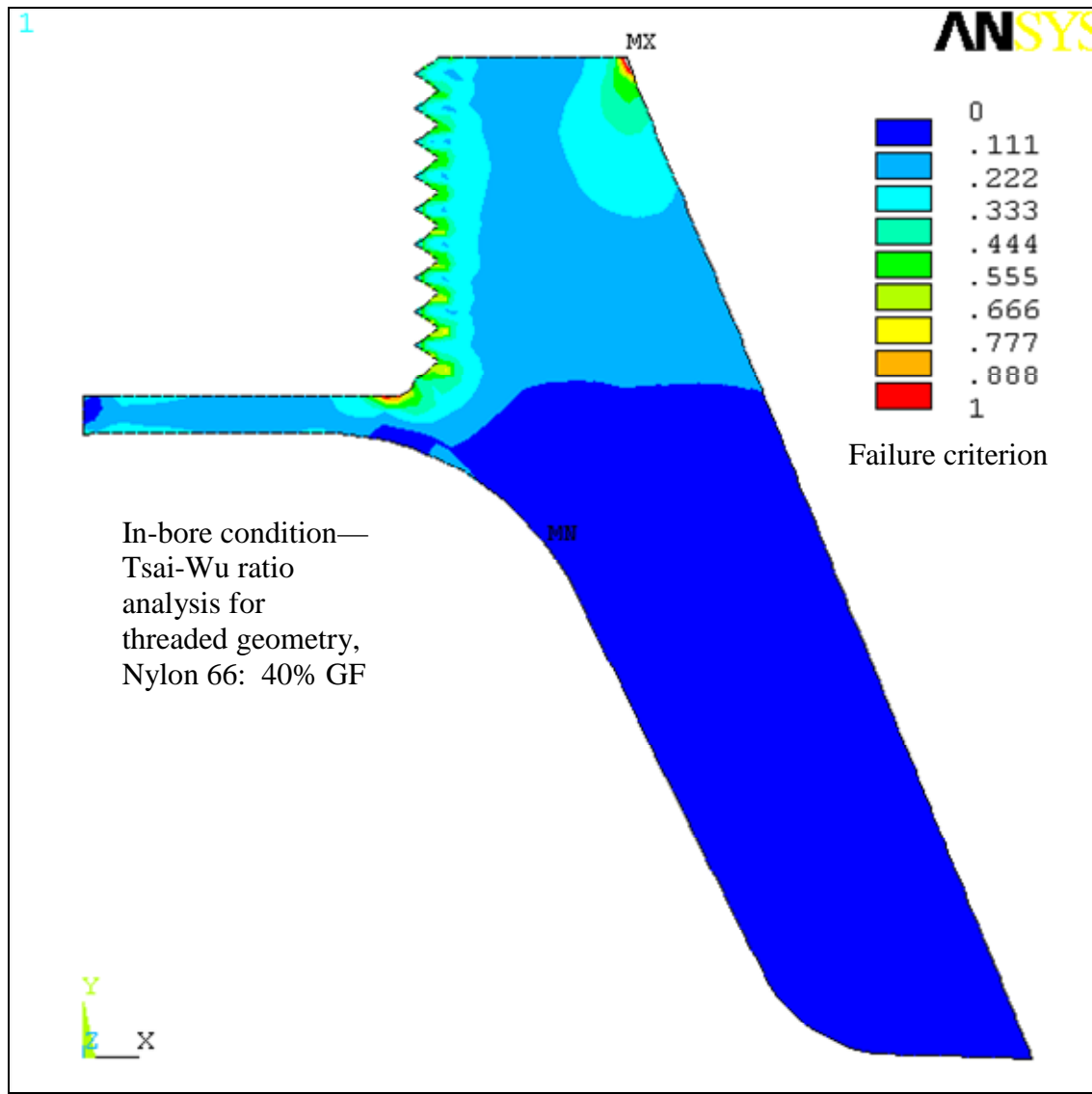


Figure 41. Detail of the Tsai-Wu failure criterion plot for the threaded LFT section of the tailcone at in-bore conditions. The LFT-aluminum interface is under the critical value of the stress.

To observe the deformation pattern of the LFT material around the beaded insert, an analysis was conducted by releasing all constraints between the LFT material and the bead (figure 43). The arrows in the figure represent the direction of relative displacement of the LFT material. The analysis shown in this figure provided useful insight into applying constraints for specific nodes along the interface of the LFT material and the beaded insert.

Figure 44 shows the results of the Tsai-Wu failure criterion incorporating the boundary conditions/constraints discussed above. It can be observed from the figure that the LFT tailcone featuring the beaded insert geometry witnesses stresses that are almost $2.5\times$ higher than the permissible stress. The maximum stresses are in the upper-right region of the tailcone, (figure 44) the same as observed for the in-bore condition analysis. The stresses in the transition

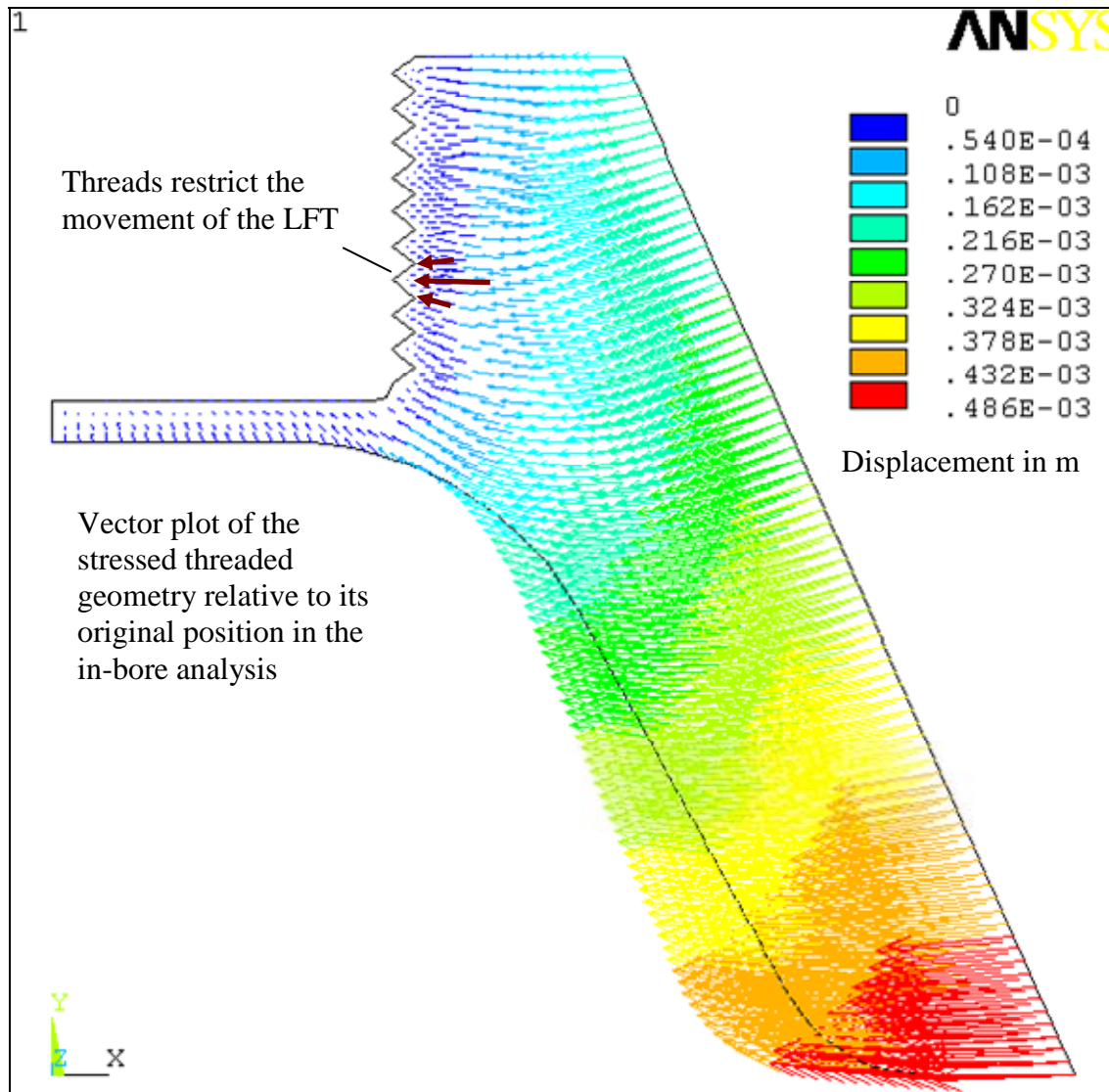


Figure 42. Vector plot that shows the displacement of the threaded LFT section of the tailcone compared to its original position. The threads restrict movement and cause better distribution of the stresses.

region are compressive. This is because the arm (figure 12) is being pushed outwards, causing a bending moment, and the maximum stressed part behaves as the axis of the arm rotation.

The failure path can be seen in figure 45. The dashed lines represent the failure path that separates the failed region of the LFT material from the rest of the tailcone. This failure is not permissible in flight since the part that is predicted to fail would render instability to the flight of the projectile. In figure 46, the vector plot shows that the stress buildup is consistent with the failure modes as observed.

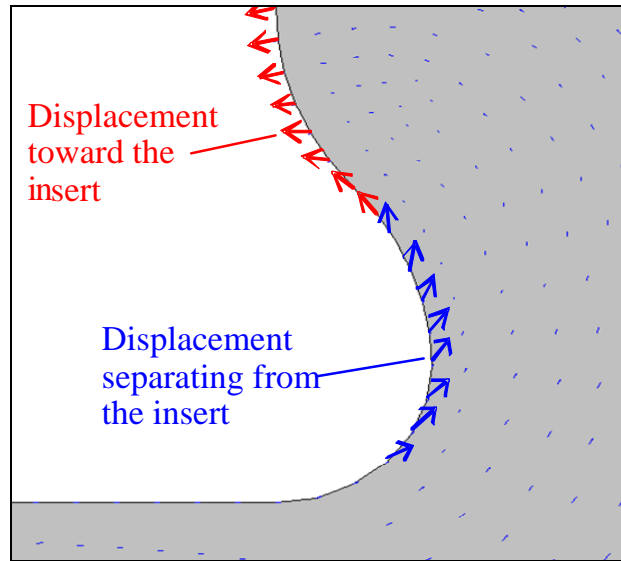


Figure 43. Displacement per node on the transition analysis for the beaded geometry. The blue arrows represent the displacement of the marked nodes as they tend to separate the aluminum insert. The red arrows represent their displacement toward the insert.

8.2.3.2 Threaded Insert Geometry. The discussion on the constraints/boundary conditions from the previous section applies to this section as well. The threaded insert geometry was analyzed assuming no boundary conditions were imposed on the threads (free to move by relative displacement). Figure 47 identifies a no-displacement point, which can be thought of as a pivot point. Around this pivot point, the displacements represented by vector arrows are observed to occur in a counter-clockwise manner (analogous to rotation of the part). These displacements around the pivot point result in two conditions (similar to those observed in the beaded-insert case), i.e., the points that move toward the insert and those that move away from the insert. The points that move toward the insert were constrained normal to the surface, and the ones that move away had no constraint (constraint released). The analysis was run using the constraints discussed in figure 48, and the results for the Tsai-Wu failure criterion are shown in figures 49 and 50.

In this analysis, the highest Tsai-Wu failure criterion value is 3.737, which is 34% higher than the beaded analysis. The reason for this increase in the threaded insert geometry value is due to a higher number of constraints (at the threads) which impede the relative movement between the LFT and the insert and results in higher stresses.

These constraints are an advantage, as it will be seen later in section 7. They provide a longer interface which provides a tortuous failure path. For the threaded insert geometry, the tailcone still fails, but less LFT material is lost during the transition condition.

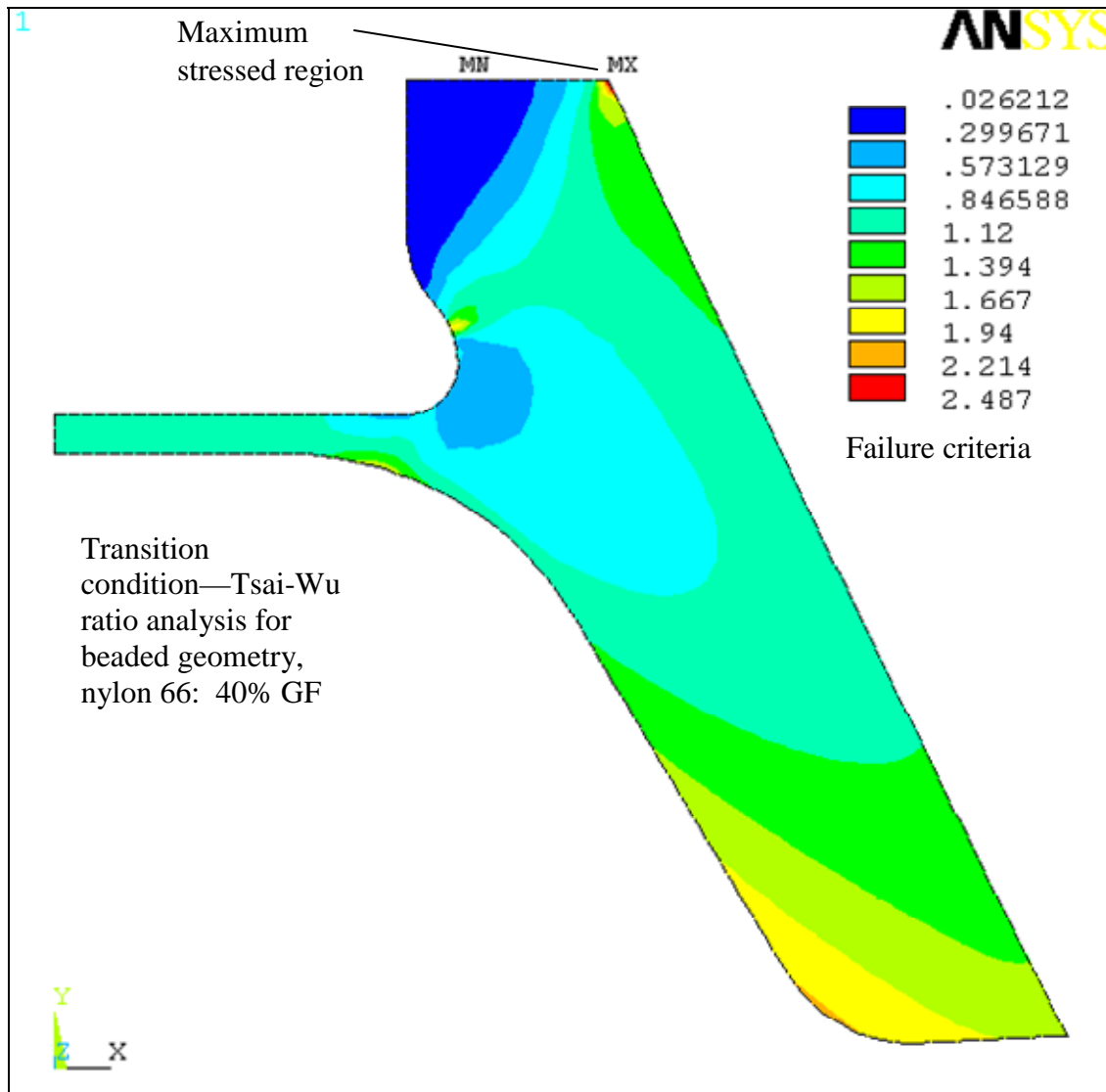


Figure 44. Tsai-Wu failure criterion plot for the beaded LFT section of the tailcone at transition conditions. The maximum value is 2.487 and is located at the edge of the bead.

9. Tests for the Hollow-Back Geometry Tailcones

Testing of LFT tailcones was conducted at Aberdeen Proving Ground (APG), MD. The testing was conducted under realistic representations of the in-bore, transition, and out-of-bore conditions. These conditions have been described in section 4. The results obtained from these tests are shown in figures 48 and 49 (for a distance of 15 m from the exit of the bore).

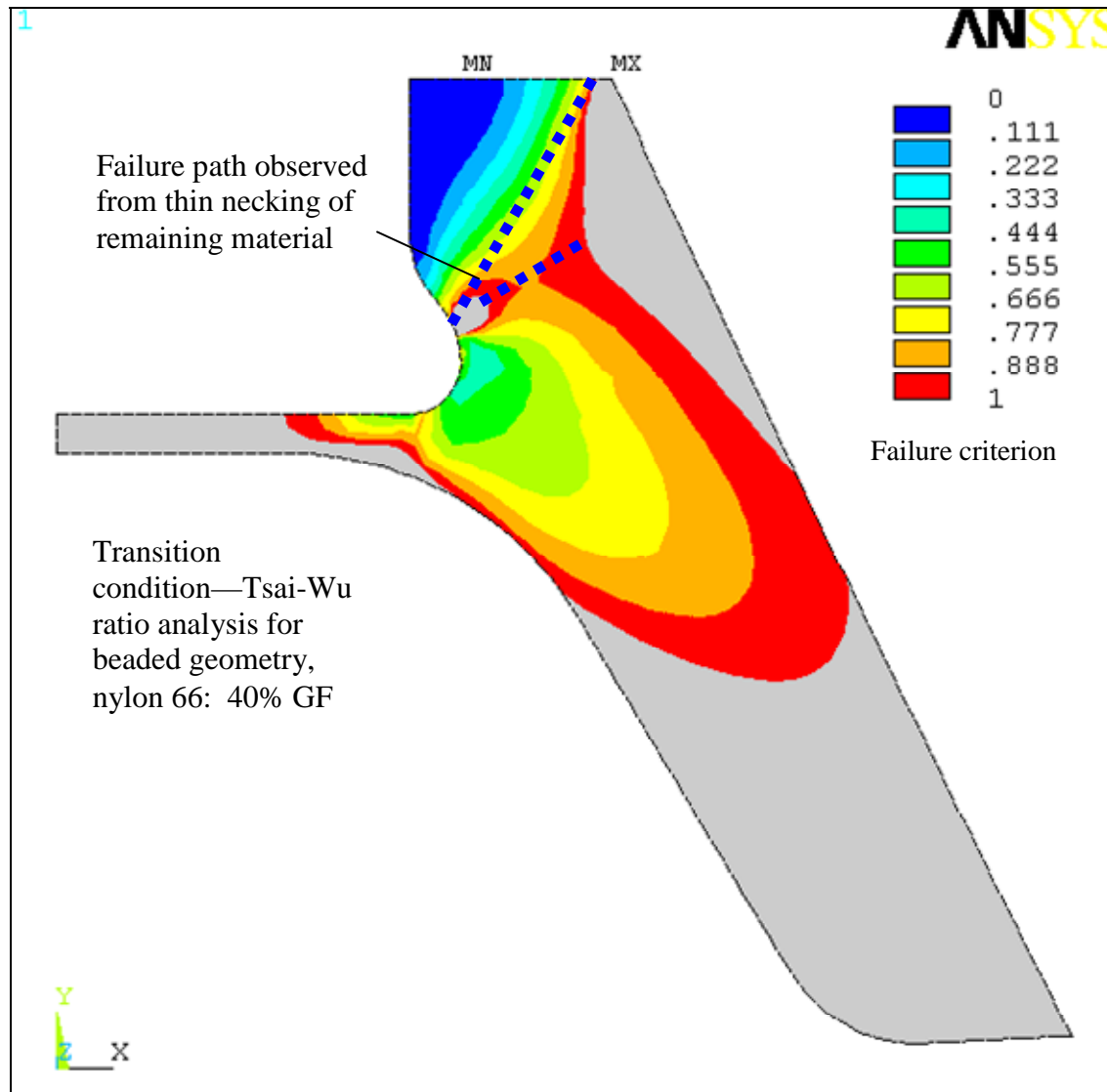


Figure 45. Detail of the Tsai-Wu failure criterion plot for the beaded LFT section of the tailcone at transition conditions. The failure path in the top part is due to the neck that is created with the load.

9.1 Beaded Insert Geometry

Figure 51 shows a picture of the projectile featuring the beaded insert geometry at a distance of 15 m from the bore exit. A portion of the LFT tailcone has been lost in flight due to the stress scenarios occurring in the transition region, which has been described in detail in section 7. The failure predicted from the analysis (figure 45) can be compared and matched with the failure path observed from the actual firing trial.

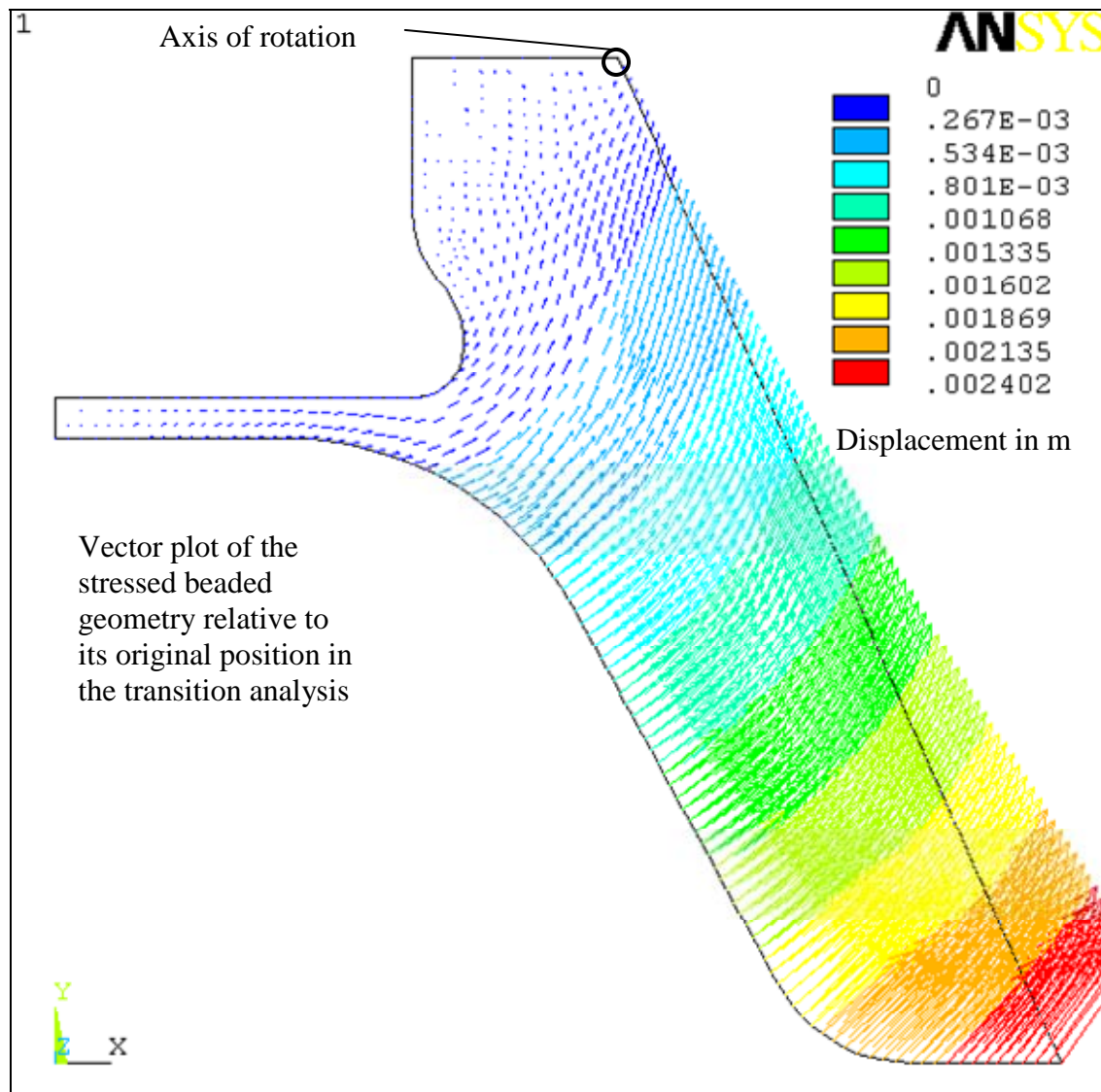


Figure 46. Vector plot that shows the displacement of the threaded LFT section of the tailcone comparing it to its original position. The region shown as the axis of rotation is where the maximum loads are applied.

The results of these tests coincide very well with the analysis for both the beaded and the threaded insert geometries. In this picture, the residual portion of the tailcone (that still remains on the projectile) coincides with the prediction from the finite element analysis (FEA). The lower portion of the bead is left bare of LFT material and shows the clean metal of the beaded insert. This happening is predicted from the FEA as well.

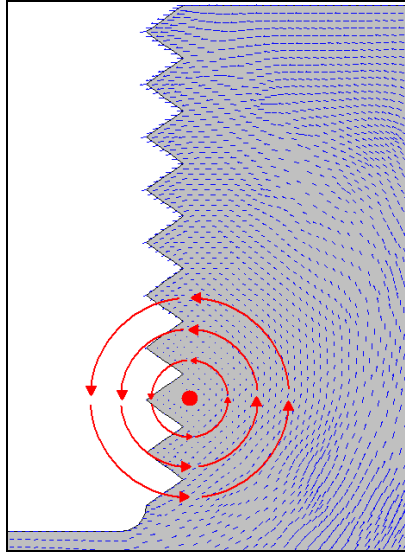


Figure 47. Displacement per node on the transition analysis for the threaded geometry. The displacements move in a counter-clockwise manner around the center point.

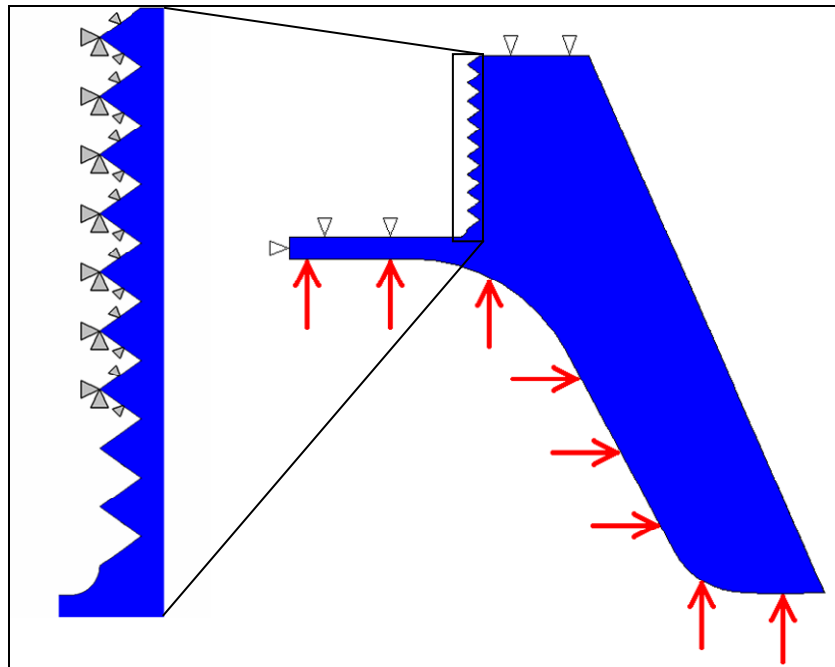


Figure 48. Initial conditions for the transition structural analysis of the LFT section of the threaded tailcone. The expanded view highlights that there are only constraints where the material displaces toward the insert.

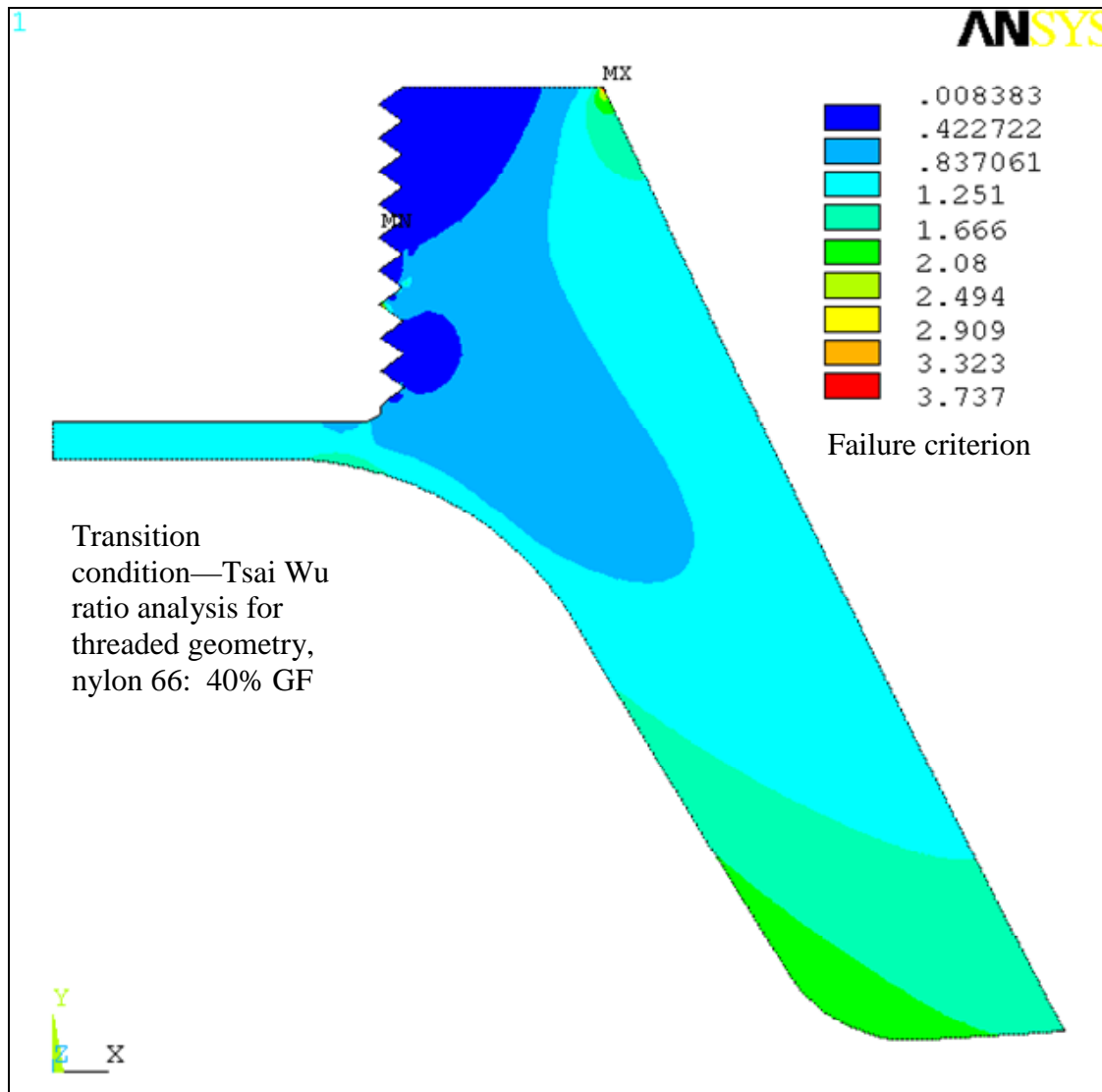


Figure 49. Tsai-Wu failure criterion plot for the threaded LFT section of the tailcone at transition conditions. The maximum value is 3.737 (33% higher for the beaded geometry), which can be attributed to the larger constrained area.

9.2 Threaded Insert Geometry

The results from firing the projectile for the threaded insert are shown in figure 52. The failure paths observed from the test coincide with the failure paths predicted by FEA. The LFT material still remaining on the tailcone matches that of the FEA. (See failure path shown by dashed lines in figure 50.)

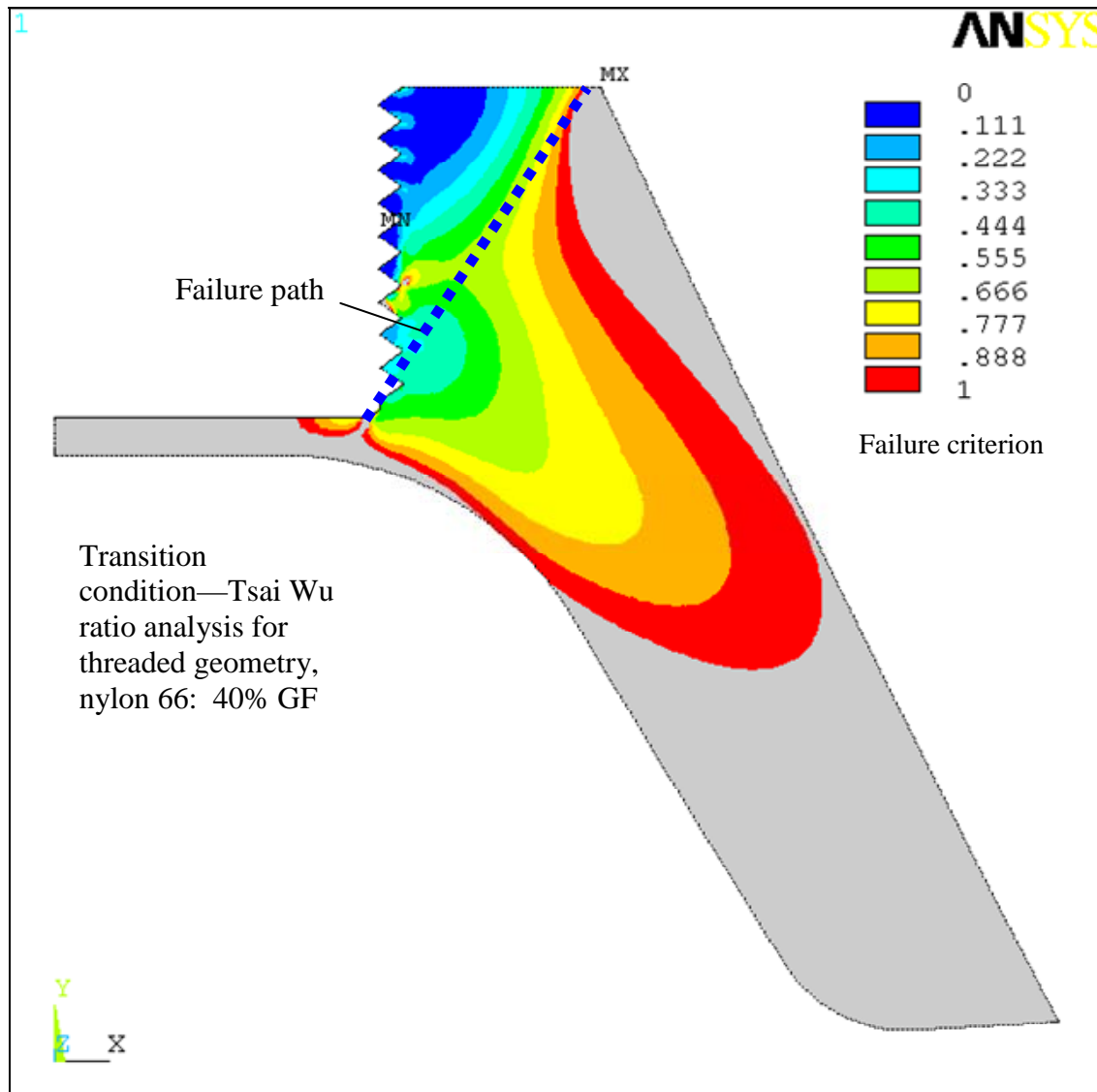


Figure 50. Detail of the Tsai-Wu failure criterion plot for the threaded LFT section of the tailcone at transition conditions. The failure path in this geometry is longer than the beaded. The failure path increase and decrease in neck length is an advantage over the beaded geometry.

10. Filled-Back LFT Tailcone

Working from the results of the hollow-back LFT tailcone testing, it was apparent that the transition condition would result in failure of the LFT-based tailcone. The hollow-back design was initially adopted to mimic the existing 7075 aluminum tailcone that is presently being used by the Army. In light of the results described in section 8, the hollow-back design was discarded.

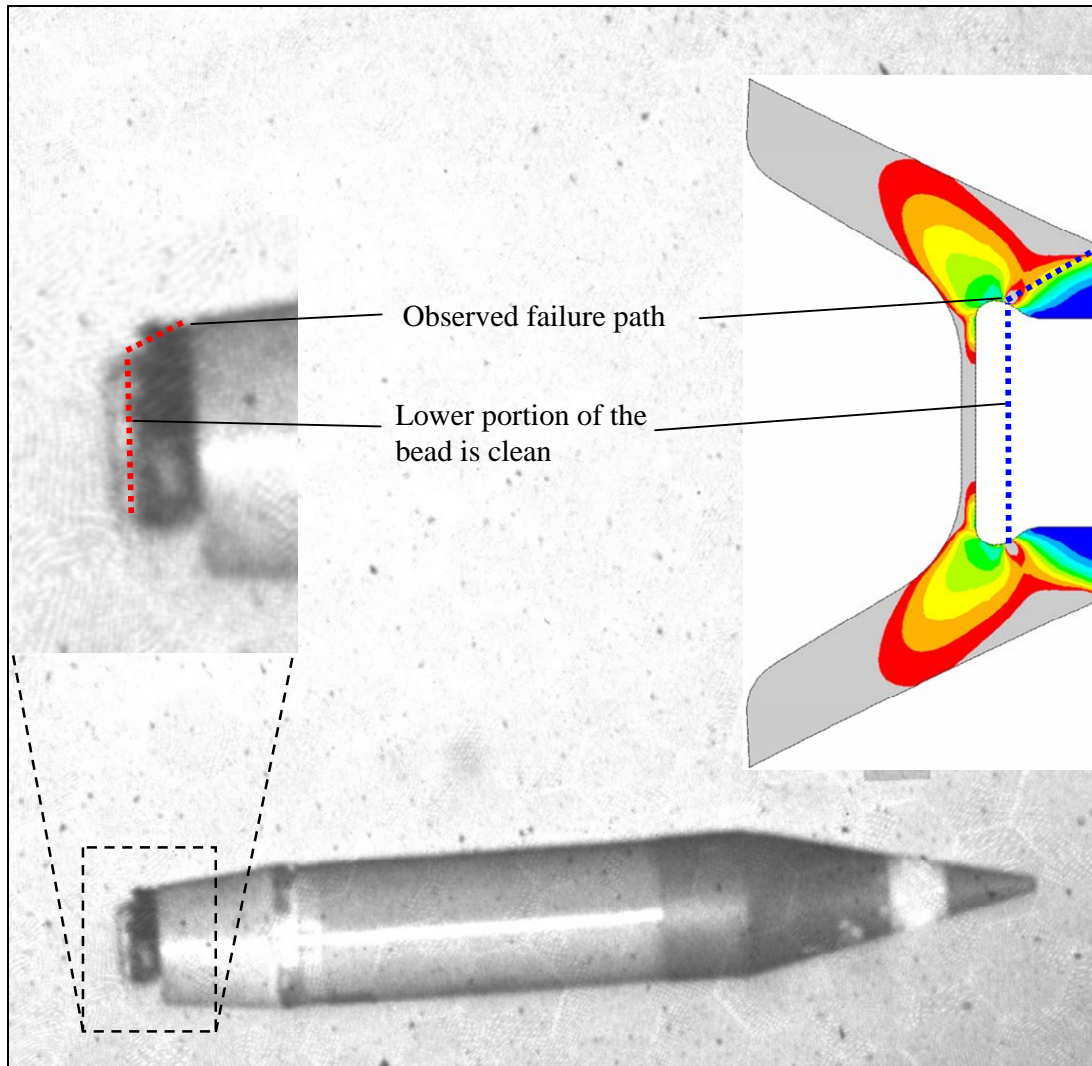


Figure 51. Fired projectile with beaded geometry at 15 m. The failure path and the line where the tailcone separates from the insert coincide with the FEA.

A new concept featuring filled-back geometry was explored for the design of the LFT tailcone. In the filled-back geometry, the basic approach was to create a tailcone that would accomplish the same objective as the previous geometry in terms of its functions such as providing stability, alignment, and drag for deceleration.

To accomplish these objectives, the tailcone geometry had to possess the same frontal area (geometric characteristics) when it comes into contact with the flow of air. This means that it had to maintain the same area and shape facing the flow. The design variations could then be accommodated only in the inner geometry.

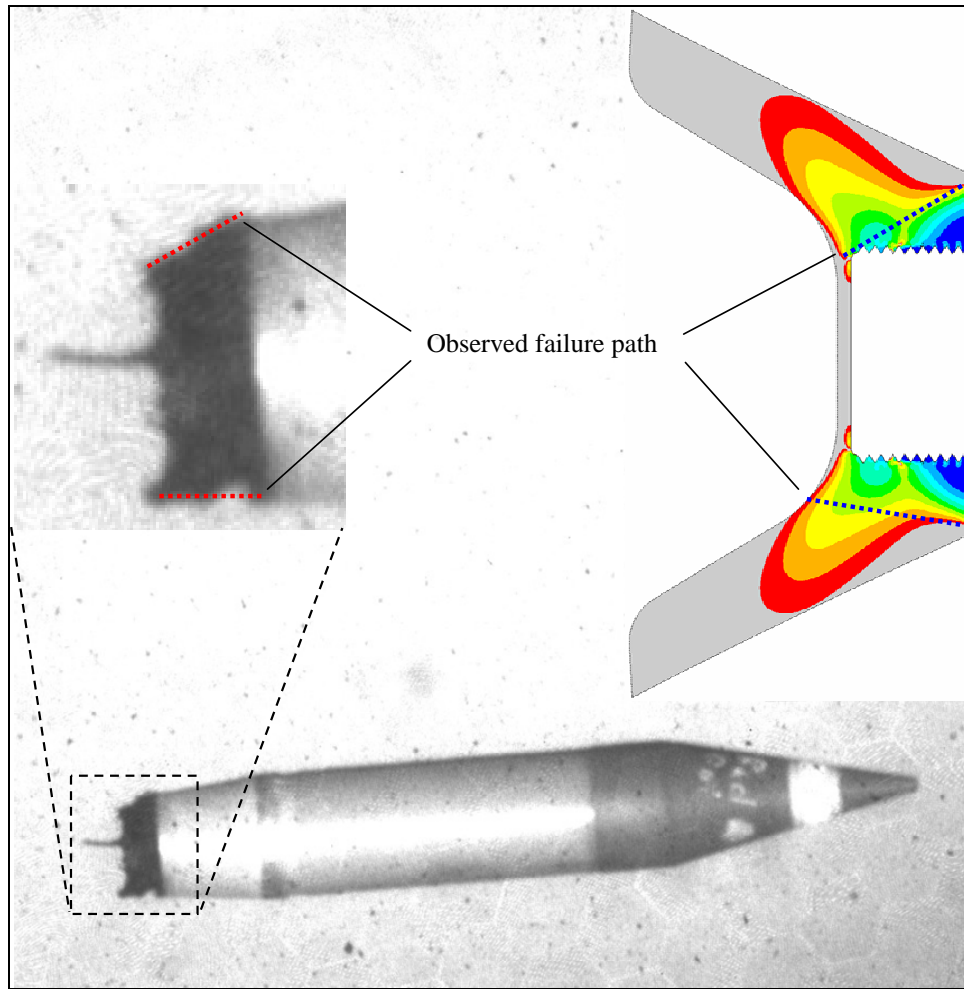


Figure 52. Fired projectile with threaded geometry at 15 m. The failure path coincides with the FEA.

The hollow-back LFT tailcone had an arm (figure 12) that bends outward tending to separate the LFT material from the insert. In the concept of the redesign, this arm was bypassed or minimized by filling the inside (the hollow portion) of the tailcone. Instead of having a 50-mm arm, it would be changed by a reduced arm length to 20 mm (40% of the original value) with added robustness. Figure 53 illustrates the filled-back tailcone concept and the reduced arm. The magnitude of the applied pressure behind the tailcone, P2, is the same as in the hollow-back geometry. The difference is in the location where the pressure is applied. In the case of the hollow-back geometry, this area was $26,500 \text{ mm}^2$ while in the filled-back geometry, this area is only $10,900 \text{ mm}^2$, which is 41% of the original area. With a smaller area, the force is also smaller, i.e., 41% of the original force.

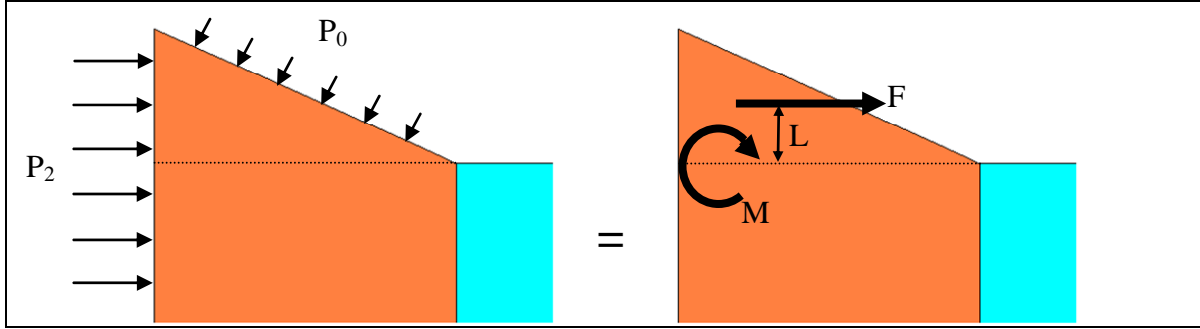


Figure 53. Transformation of the applied pressures into a force and a moment. The figure shows the filled-back geometry compared to the hollow-back geometry. The arm for the filled-back geometry is 40% smaller.

10.1 Two Different Insert Geometries

With the outer geometry now defined (i.e., filled-back), the idea was to provide an insert that would be compatible with this geometry so that it would cause the least amount of stresses in the LFT part and possess a strong interface to prevent failure. The concept of the threaded insert was proven to be effective in the case of the hollow-back tailcone for the portion of the LFT that survived. Hence the use of the threaded insert continued to be adopted for the filled-back version. The length of the insert was then determined.

For the tailcone to survive the flight, the contact between the insert and the LFT should be maximized. Two insert dimensions were considered. First, a 100-mm-long insert that would extend the full depth of the cone and, second, a 95-mm-long insert (referred to as the 95 and 100 geometries for discussion purposes).

The main difference between these two insert lengths is that for the 95-mm-long insert, a 5-mm LFT lip is left in the lower part of the tailcone. Figure 7 shows the two configurations.

10.1.1 Rationale for the 95-mm Insert Geometry

The rationale for the 95-mm insert geometry is that the lip has the potential to provide a seal for the hot gases from combustion, escaping and/or initiating failure at this location. If these gases are not blocked, they can separate the LFT part from the insert, causing it to fail. The 5-mm lip not only blocks the gases by acting as a lid, but also acts as a structural member that undergoes tension when the tailcone is in the transition regime. Due to tension stresses, the relative separation between the LFT and the insert in the bottom part of the tailcone is less, hence causing lesser stresses in the threaded part. The stresses are shifted from the threads to the point of contact between the lip and the threaded section of the tailcone.

10.1.2 Rationale for the 100-mm Insert Geometry

The 100-mm insert geometry was designed for two purposes: to have the maximum contact area (5 more mm as compared to the 95 mm) for the threads and to have access to the metallic insert for further machining and/or assembly of the tracer. However, in the 100-mm insert, the LFT can separate from the insert (due to weak interface), and this can create a gap for hot gases to escape. The gap has to be prevented by adding a protective coating to the bottom part of the tailcone, such as room-temperature vulcanizing (RTV) silicone.

10.2 Structural Analysis

The LFT material properties of the tailcone and the insert were similar to those for the hollow-back design. The element types and the design criteria for the beaded and threaded insert analysis were the same as for the hollow-back cone.

10.2.1 In-Bore Conditions

10.2.1.1 The 95-mm Insert Geometry. The initial loading conditions for the 95-mm insert geometry are shown in figure 54. The constraints in the in-bore case are applied at every thread in the direction normal to the surface. The LFT-aluminum interface was treated as a no-bonded, frictionless interface.

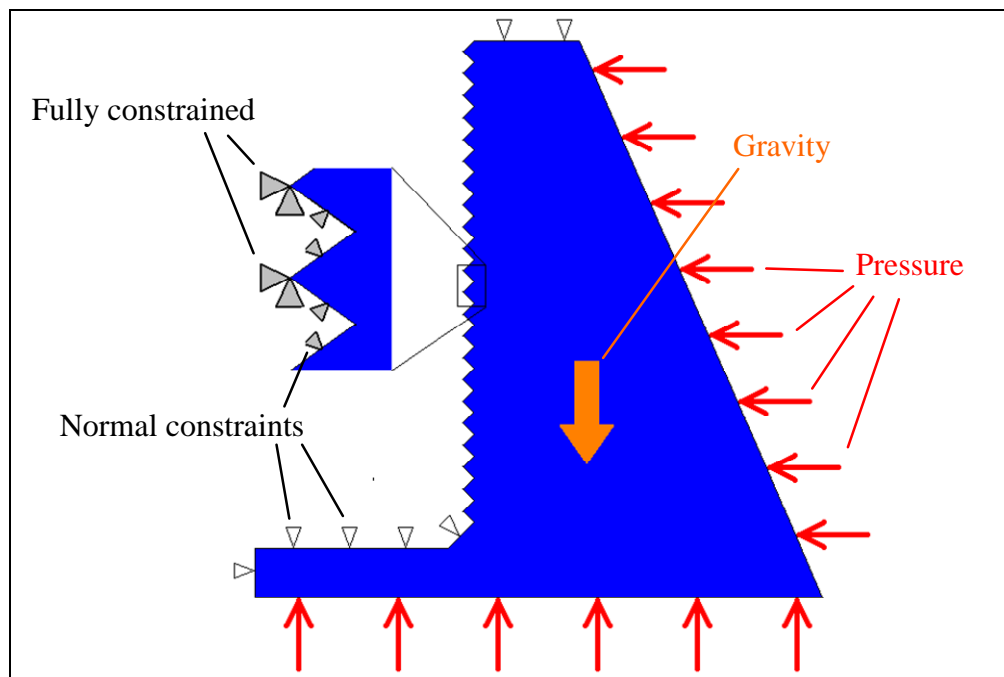


Figure 54. Initial conditions for the in-bore structural analysis of the LFT section of the 95-mm insert tailcone. The expanded inset highlights that the threads are fully constrained at each corner and normally constrained at each groove.

The results from this analysis are plotted in figures 55 and 56. Figure 55 shows the maximum value of the Tsai-Wu failure criterion as 1.307. (It fails by a factor of 0.307.) Figure 56 illustrates the analysis detail that shows that the failure region (in compression) is very small compared to the total area of the part (0.6% of the total area). The Tsai-Wu failure criterion is 4% higher than the threaded geometry in the in-bore analysis.

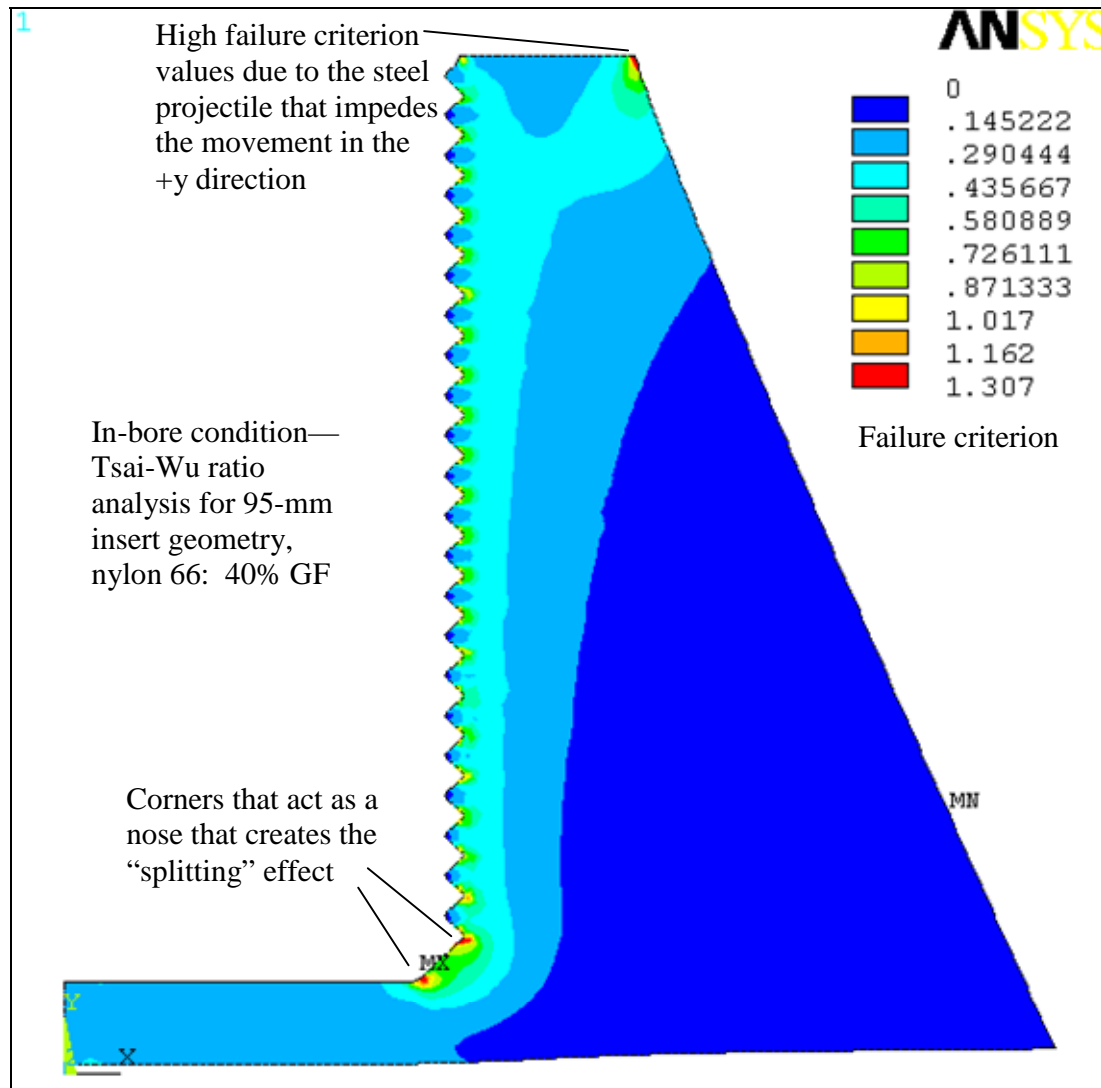


Figure 55. Tsai-Wu failure criterion plot for the 95-mm insert LFT section of the tailcone at in-bore conditions. The maximum value is 1.307 and is located at the bottom corner where the threads meet the lip. This is due to the splitting nose effect seen also in the beaded geometry.

Two things can be said about these results. First, although there are regions in the LFT tailcone (95-mm insert geometry) where the failure criterion is higher than the maximum allowable stress, the Tsai-Wu criterion for each of the threads is within the passing value (less than 1). The higher values are not in the threads but at the bottom corner, where the LFT material senses the same nose effect observed for the beaded geometry (section 8.2.3.1), and in the top-right corner,

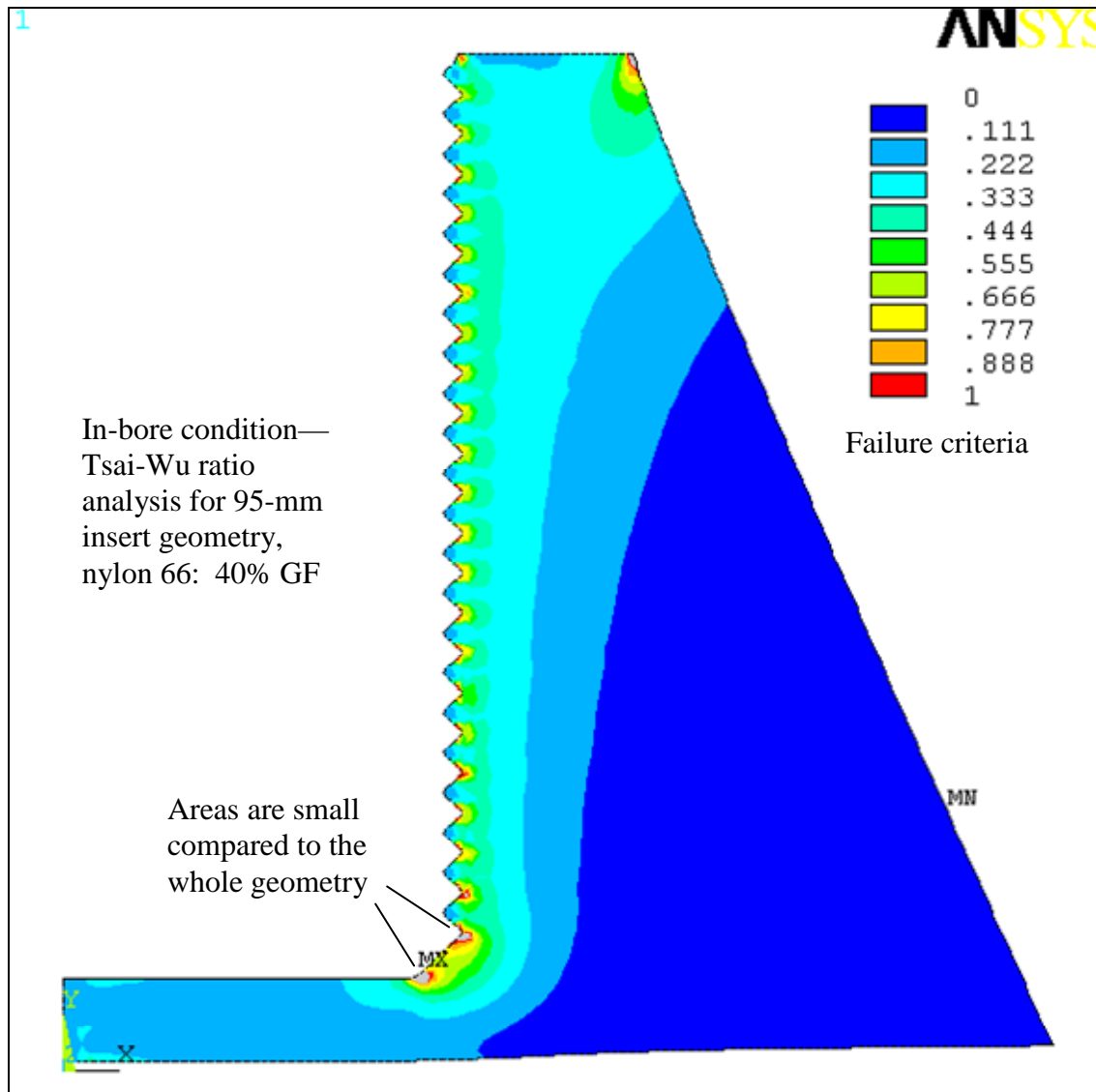


Figure 56. Detail of the Tsai-Wu failure criterion plot for the 95-mm insert LFT section of the tailcone at in-bore conditions. The area of the failure region is 0.6% of the total LFT area.

due to the steel projectile that prevents the displacement of the LFT tailcone. Second, this design has a stiffer geometry compared to the hollow-back geometries (with the beaded or threaded insert). In the case of the hollow-back geometry, the moment arm allows the geometry to release stresses by deforming itself. These stresses have to be within reasonable values to prevent the failure.

10.2.1.2 The 100-mm Insert Geometry. The initial conditions for this geometry are the same as those for the 95-mm insert geometry. These are shown in figure 57. In this case, the LFT-aluminum interface was again treated as an unbounded, frictionless interface.

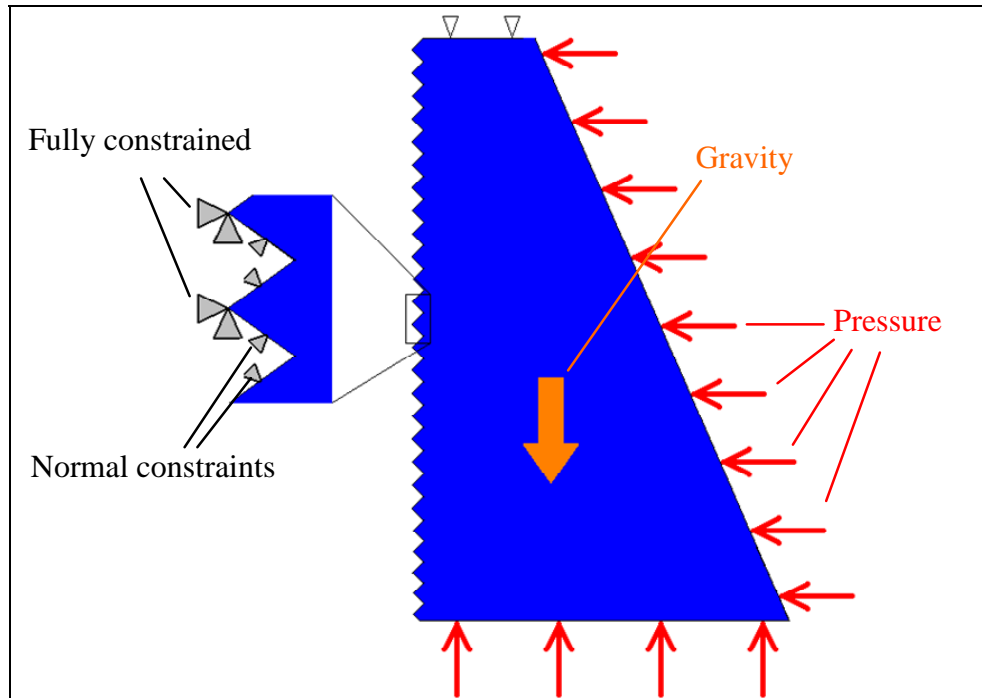


Figure 57. Initial conditions for the in-bore structural analysis of the LFT section of the 95-mm insert tailcone. The detail shows the threads fully constrained at each corner and normally constrained at each thread.

The results from this analysis are plotted in figures 58 and 59. Figure 58 shows the maximum value of the Tsai-Wu failure criterion as 1.494. (It is failing by a factor of 0.494.) In this case, the failure criterion is 13% higher than for the 95-mm insert geometry. Figure 59 shows that the new failure region area is 0.1% of the total area, which is 0.5% smaller than for the 95-mm insert geometry.

The threads are within the Tsai-Wu failure criterion (lower than 1), and the fact that this geometry does not have an LFT lip makes the geometry less susceptible to the splitting nose effect. The higher value of the Tsai-Wu failure criterion is not witnessed in the threads but in the top corner where the LFT-to-steel interface becomes the stress raiser. The fact that the failure region is only 0.1% of the total area, and it only occurs as a point stress (no failure path), makes this geometry more reliable than the 95-mm insert geometry for the in-bore condition.

10.2.2 Transition Condition

In the case of the hollow-back LFT tailcone (both the beaded and threaded insert geometries), the transition condition was the most critical because this was the condition that caused failure. The filled-back tailcones (with 95- and 100-mm inserts) were analyzed for the loading and boundary conditions. The results for the 95- and 100-mm inserts follow.

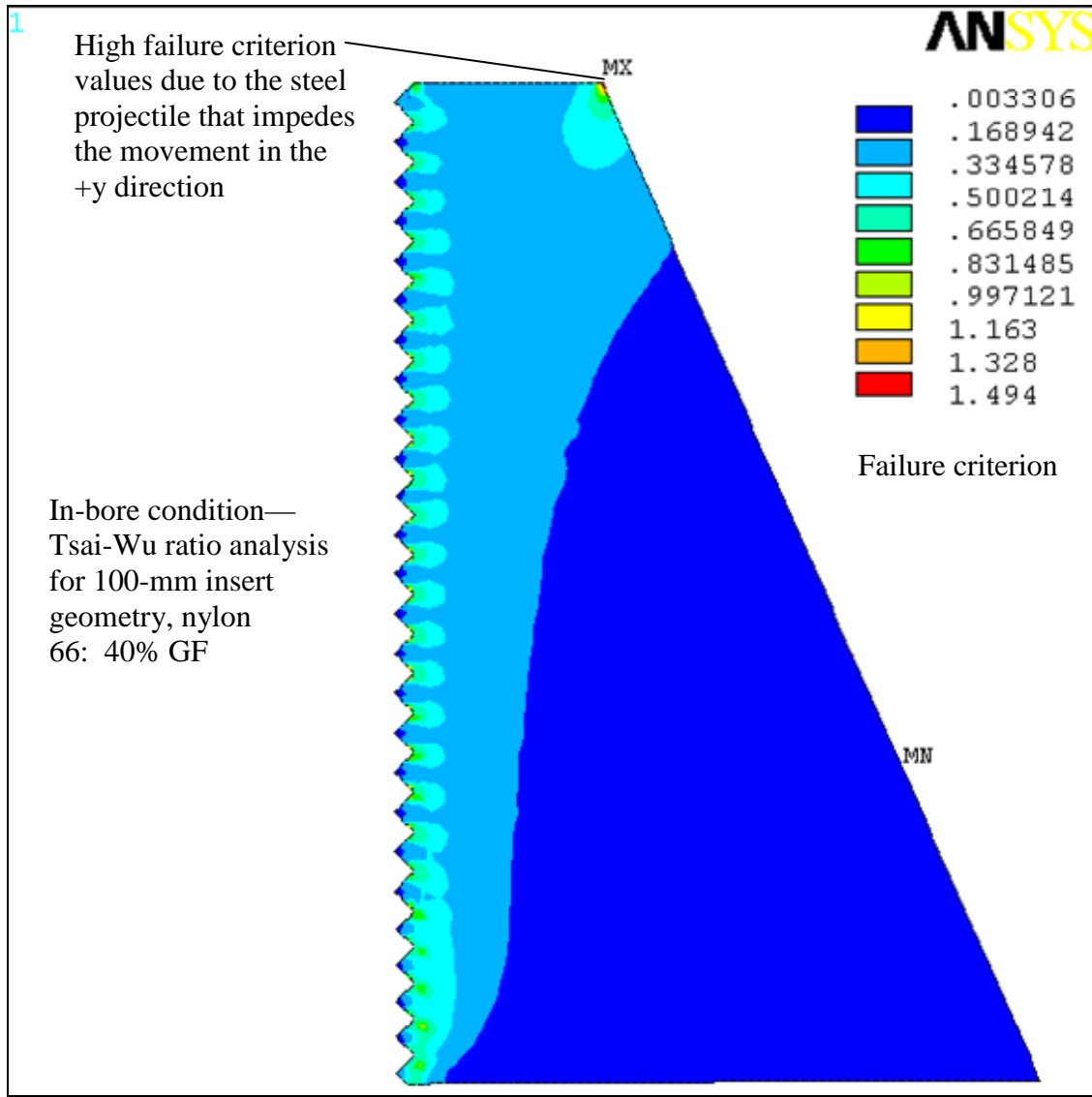


Figure 58. Tsai-Wu failure criterion plot for the 100-mm insert LFT section of the tailcone at in-bore conditions. The maximum value is 1.494 and is located at the top corner where the LFT meets the steel projectile.

10.2.2.1 The 95-mm Insert Geometry. The applied loads for the 95-mm insert geometry are shown in figure 60. The stresses witnessed by each thread in the case of the 95-mm insert (filled-back tailcone) at the transition condition are different than the stresses for the transition condition of the hollow-back tailcone with threaded insert (figures 47 and 48) and the in-bore condition of the 95- and 100-mm insert filled-back geometries (figures 54 and 57).

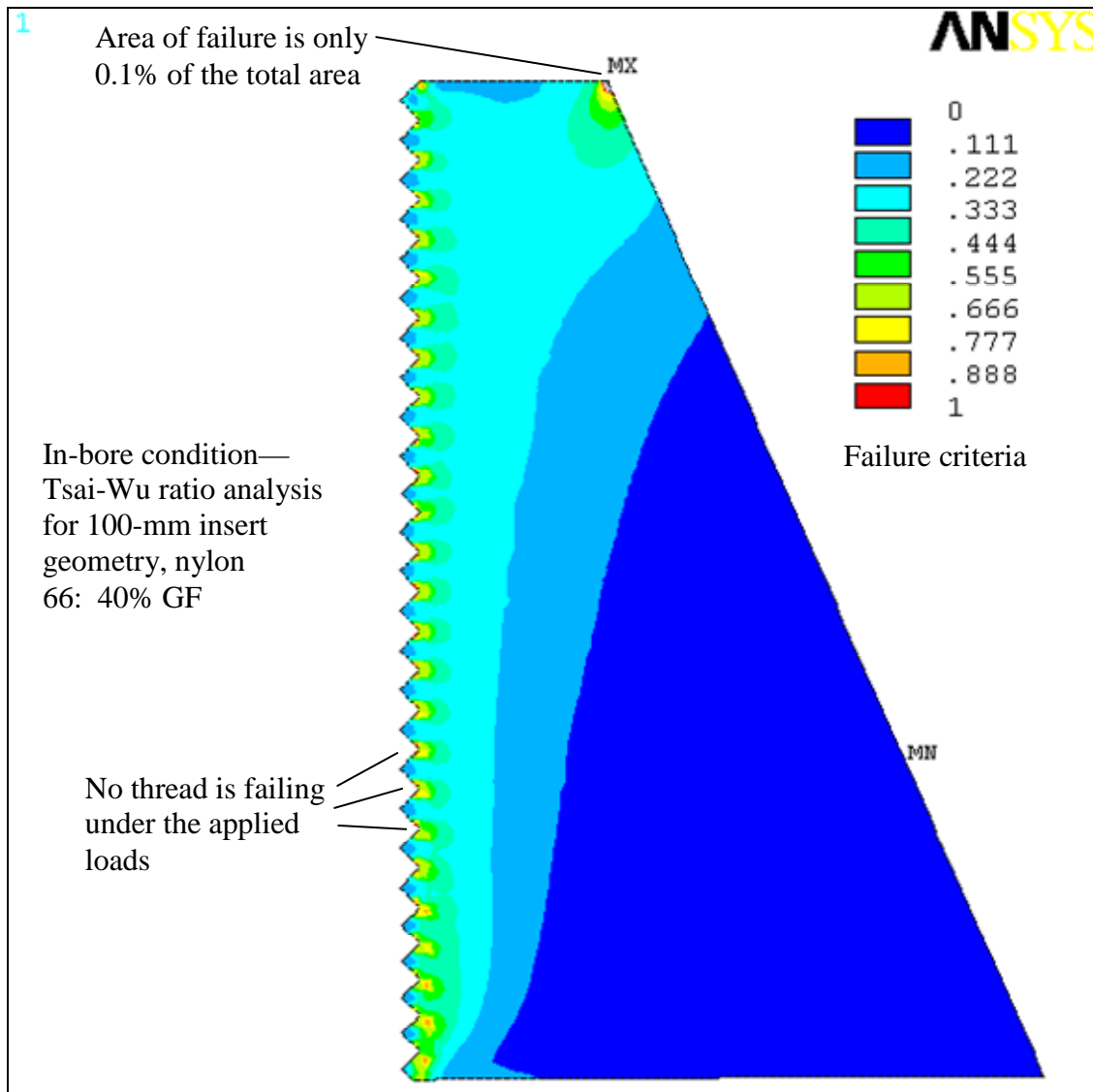


Figure 59. Detail of the Tsai-Wu failure criterion plot for the 100-mm insert LFT section of the tailcone at in-bore conditions. The failure region area is 0.1% of the total LFT area.

For the 95-mm insert, the rotation axis was not located in the threads, as can be seen in figure 61, because the pressure is normal to the bottom face (figure 60). For the hollow-back tailcone with the threaded insert geometry (figure 47) at the transition condition, the axis of rotation is located in the threads. Because the rotation axis is presumably outside the geometry, the LFT material is subjected primarily to axial stress (i.e., no bending). The pressure being normal to the bottom face of the tailcone results in the reaction forces to be oriented in the y direction as shown in figure 60. Furthermore, in the thread region, the resultant in each thread is also in the y direction. Hence, as can be noted from figure 57, a normal constraint is provided at the top surface of each thread. This constraint impedes normal thread movement but allows normal transverse movement.

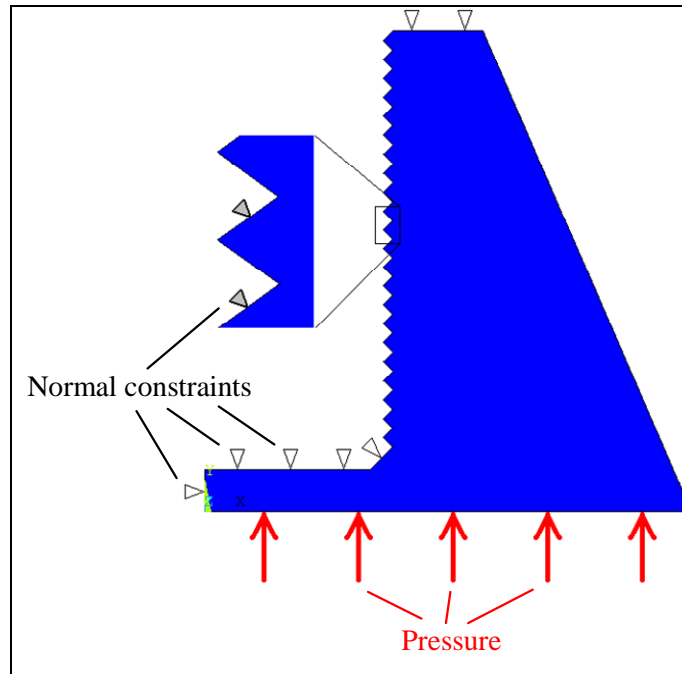


Figure 60. Initial conditions for the transition structural analysis of the LFT tailcone with a 95-mm insert. The detail shows the threads constrained normally in the top surface of each thread. The applied pressure is only in the y direction.

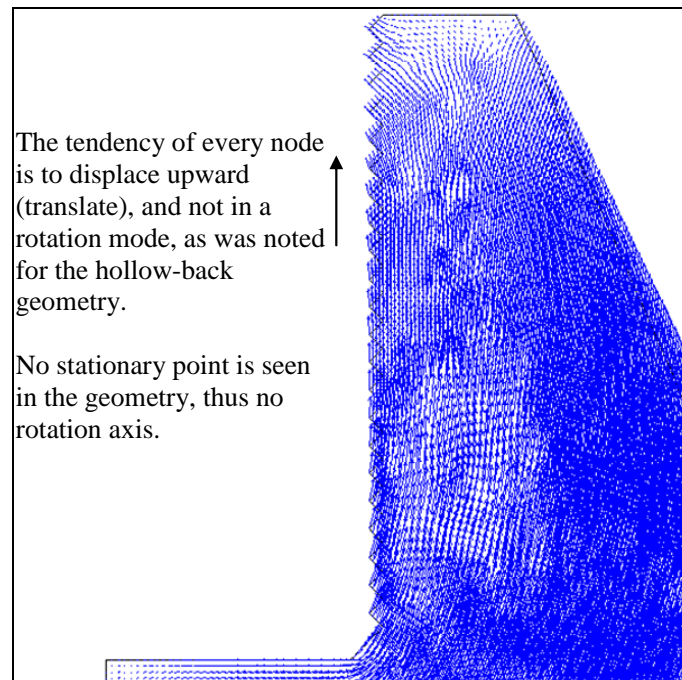


Figure 61. Displacement-per-node plot for the 95-mm insert geometry at the transition condition. No stationary point can be seen in the geometry, thus no rotation axis was assumed.

The results from this analysis are shown in figures 62 and 63. Figure 62 shows the maximum value of the Tsai-Wu failure criterion, which is 2.798 (it fails by a factor of 1.798). In this case, the failure criterion is 34% smaller than the case of the threaded geometry of the hollow-back LFT tailcone. The failure area in the present case is 4% of the total area (figure 63).

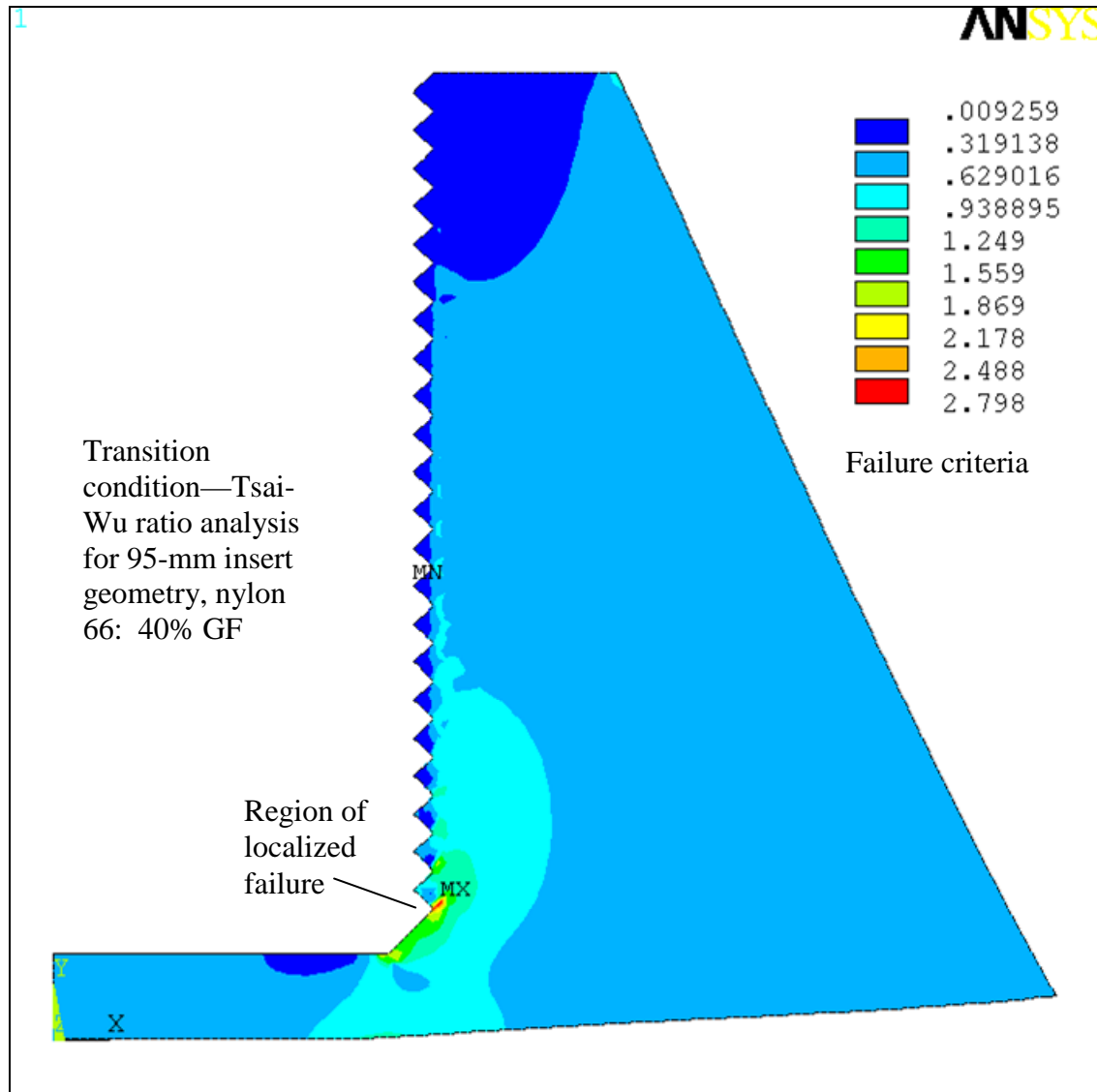


Figure 62. Tsai-Wu failure criterion plot for the 95-mm insert LFT section of the tailcone at the transition condition. The maximum failure criterion value is 2.789.

The results for this analysis show that although this geometry has local failure regions, they do not comprise the bulk area of the geometry. If the Tsai-Wu ratio results are compared to those for both the hollow-back geometries (i.e., beaded and threaded insert), the filled-back tailcone exhibits better performance.

It may be noted from figure 63 that three of the 22 threads that are in contact with the LFT material have undergone failure locally. This may lead to a failure path connecting to the lower-outer face (the thin layer in the back referred to as the lip in this report) as shown by the dashed line. The generated failure path is safe from a survivability point of view, because even if the tailcone were to fail in this local region, the residual part is subjected to compression. The pressure from the transition condition would result in compression of the bottom part of the insert.

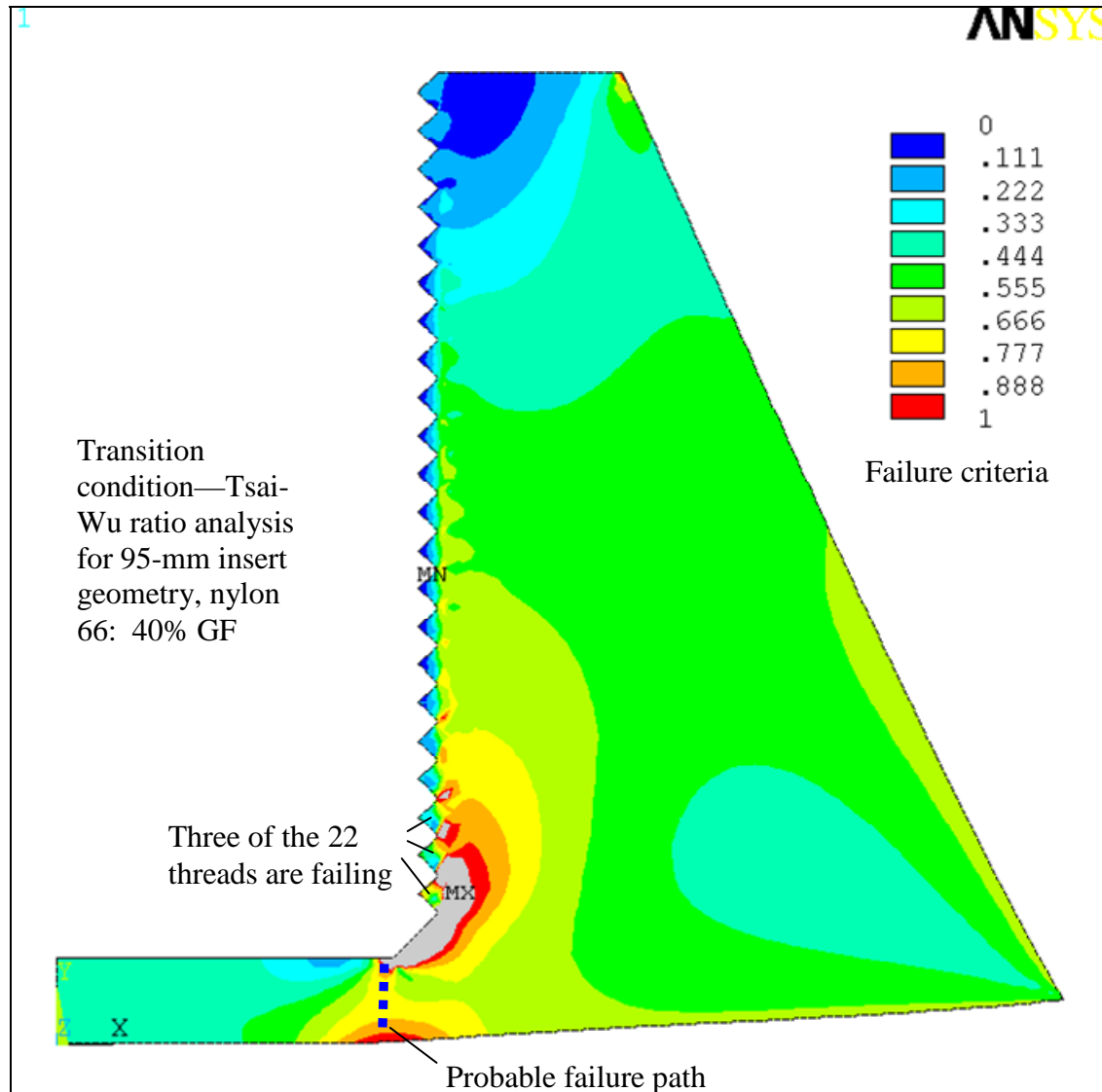


Figure 63. Detail of the Tsai-Wu failure criterion plot for the 95-mm insert LFT tailcone at the transition condition. The probable failure path divides the lip from the tailcone. The lip will be compressed toward the insert by the pressure at transition.

Figure 64 shows the x-plot displacement of the 95-mm insert geometry. This figure illustrates that the maximum displacement in the threaded face of the LFT is 0.09 mm. This indicates that the lip holds the LFT tailcone in position, so little relative displacement (between the LFT and the insert threads) is observed as the pressure at the transition condition is applied.

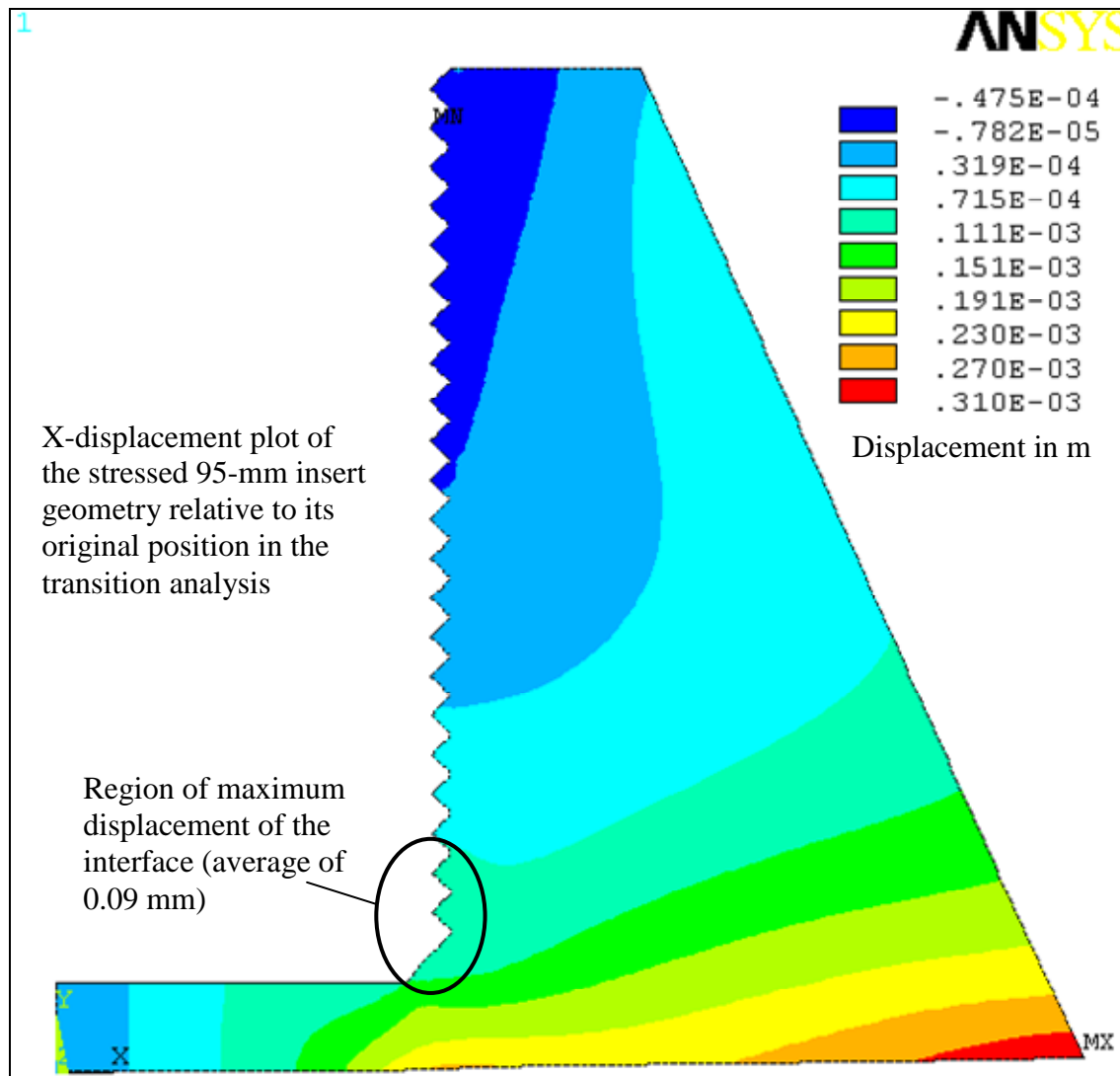


Figure 64. X-displacement plot of the 95-mm insert LFT section of the tailcone. A maximum displacement of 0.09 mm is calculated for the threads under load.

10.2.2.2 The 100-mm Insert Geometry. The applied loads for the 100-mm insert geometry are shown in figure 65. The stresses for this new geometry are applied in the same direction as for the 95-mm insert geometry. In this case, there is no lip that protects the LFT tailcone from the high-pressure and high-temperature gases that are generated from the detonation. Due to the absence of the lip, less area of the LFT would be exposed to the gases, and more threads (26 threads vs. 22 for the 95-mm geometry) would be holding the insert to the LFT. This was

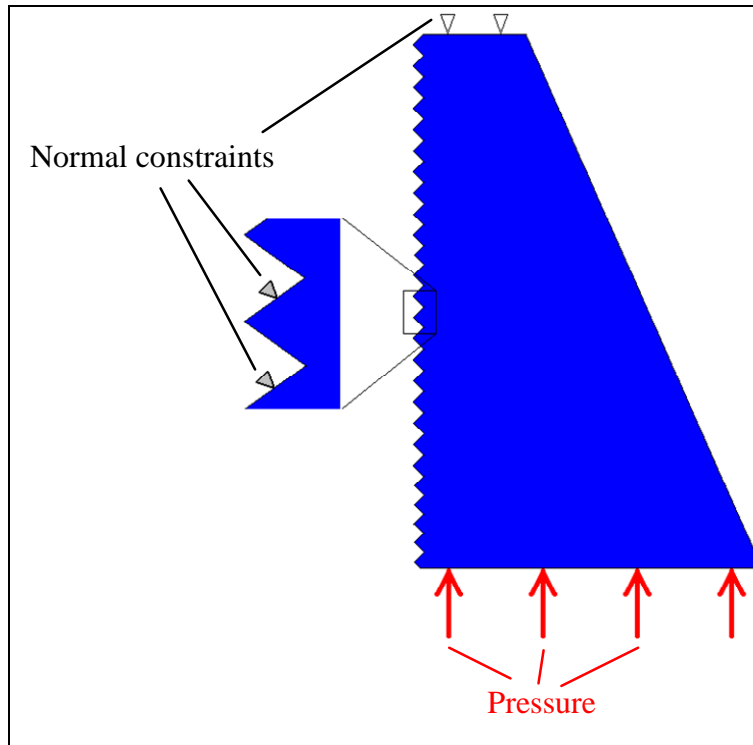


Figure 65. Initial conditions for the transition structural analysis of the LFT section of the 100-mm insert tailcone. The detail shows the threads constrained normally in the top surface of each one. The applied pressure is only in the y direction.

the reasoning behind testing both geometries; the 95-mm insert geometry offered protection from the gases and from over-deformation (by the use of the lip). The 100-mm geometry offered more area in contact with the threads (in comparison to the 95-mm insert geometry) and access to the back of the insert to mount a tracer.

The Tsai-Wu analysis results for the 100-mm insert geometry are shown in figures 66 and 67. Figure 66 shows the maximum value of the Tsai-Wu failure criterion, which is 2.185 (it fails by a factor of 1.185). The failure criterion is 28% smaller than for the case of the 95-mm insert geometry. The failure area in the present case is 1.5% of the total area (figure 67).

The results of this analysis on the 100 mm insert show the same behavior as that for the 95-mm insert geometry in the transition condition. Figure 68 shows the computed displacement plot for the 100-mm insert design. The local failure regions comprise only two isolated areas, i.e., the bottom-left corner (at the first thread) and the top-right corner (where the LFT meets the steel projectile). In this case, only one of the 26 threads (4%) witnesses failure loads (10% less than the 95-mm insert geometry).

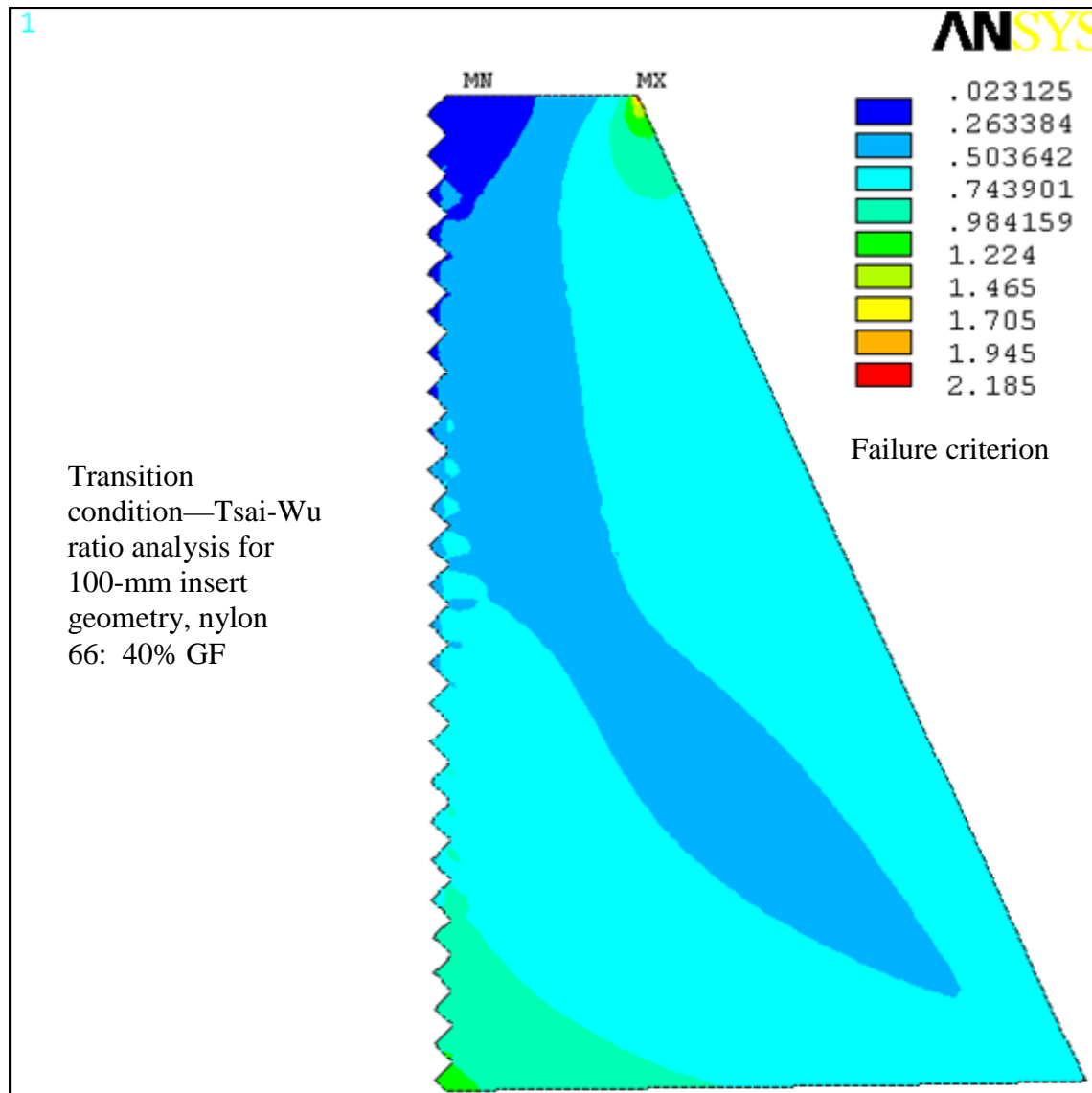


Figure 66. Tsai-Wu failure criterion plot for the 100-mm insert LFT section of the tailcone at the transition condition. The maximum failure criterion value is 2.185.

The disadvantage of the 100-mm insert geometry is the separation of the bottom LFT threads from the insert. In the case of the 95-mm insert, the separation was 0.09 mm, while in the 100-mm insert geometry, the separation was 0.345 mm (4× higher). This separation, which is not a problem for the 95-mm insert geometry, must be avoided by applying RTV silicone to the bottom part of the tailcone. The threads would be exposed and damaged from the high-temperature and high-pressure gases.

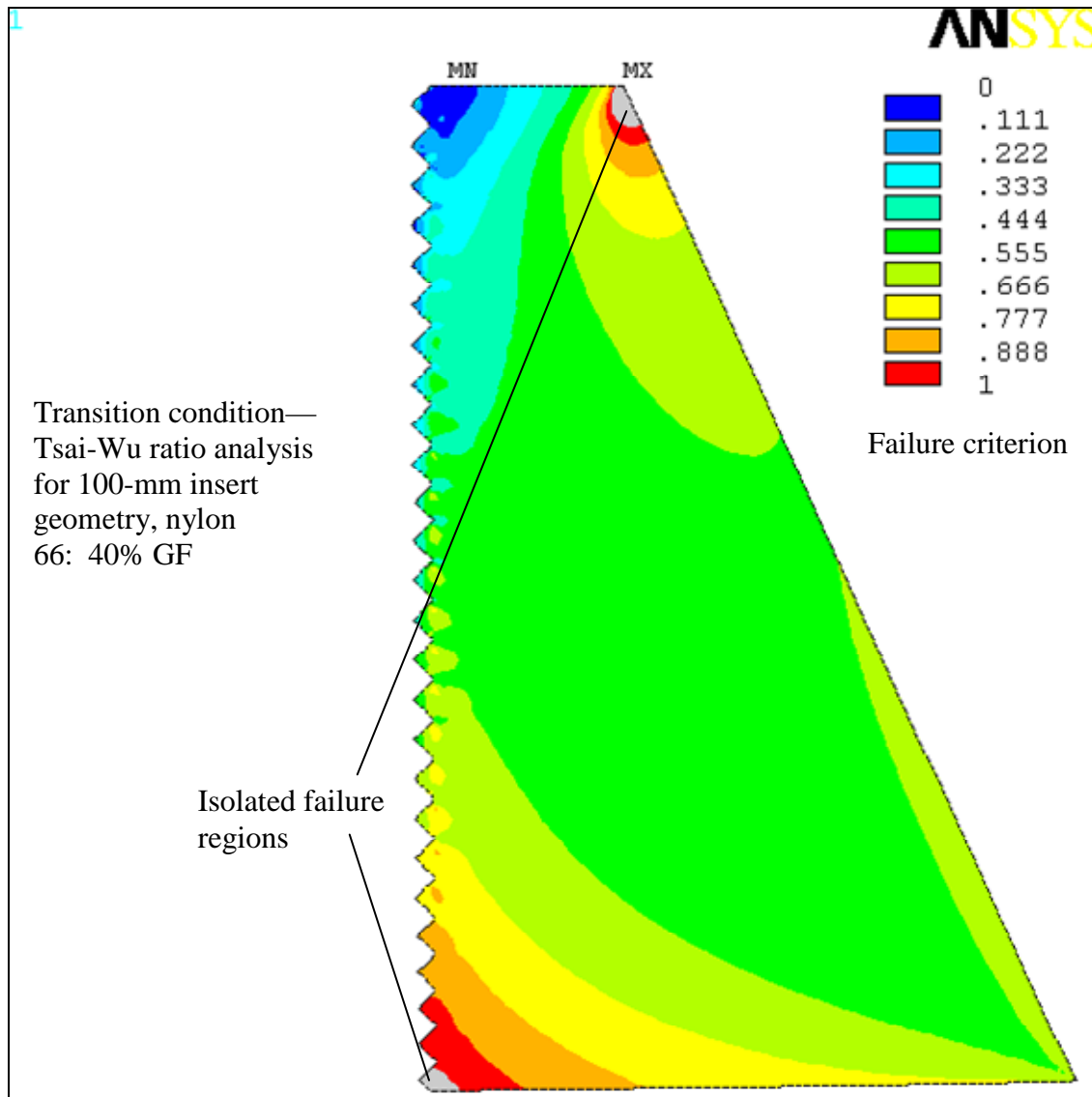


Figure 67. Detail of the Tsai-Wu failure criterion plot for the 100-mm insert LFT section of the tailcone at the transition condition. From a structural point of view, this geometry has better performance than the 95-mm insert geometry.

11. Tests for the Filled-Back Geometry Tailcones

Testing of the filled-back 40% glass-content LFT tailcones was also conducted at APG. The results obtained from these tests (for a distance of 5 and 15 m from the exit of the bore) are shown in figures 69 and 70. Both insert geometries (95 and 100 mm long) were successful.

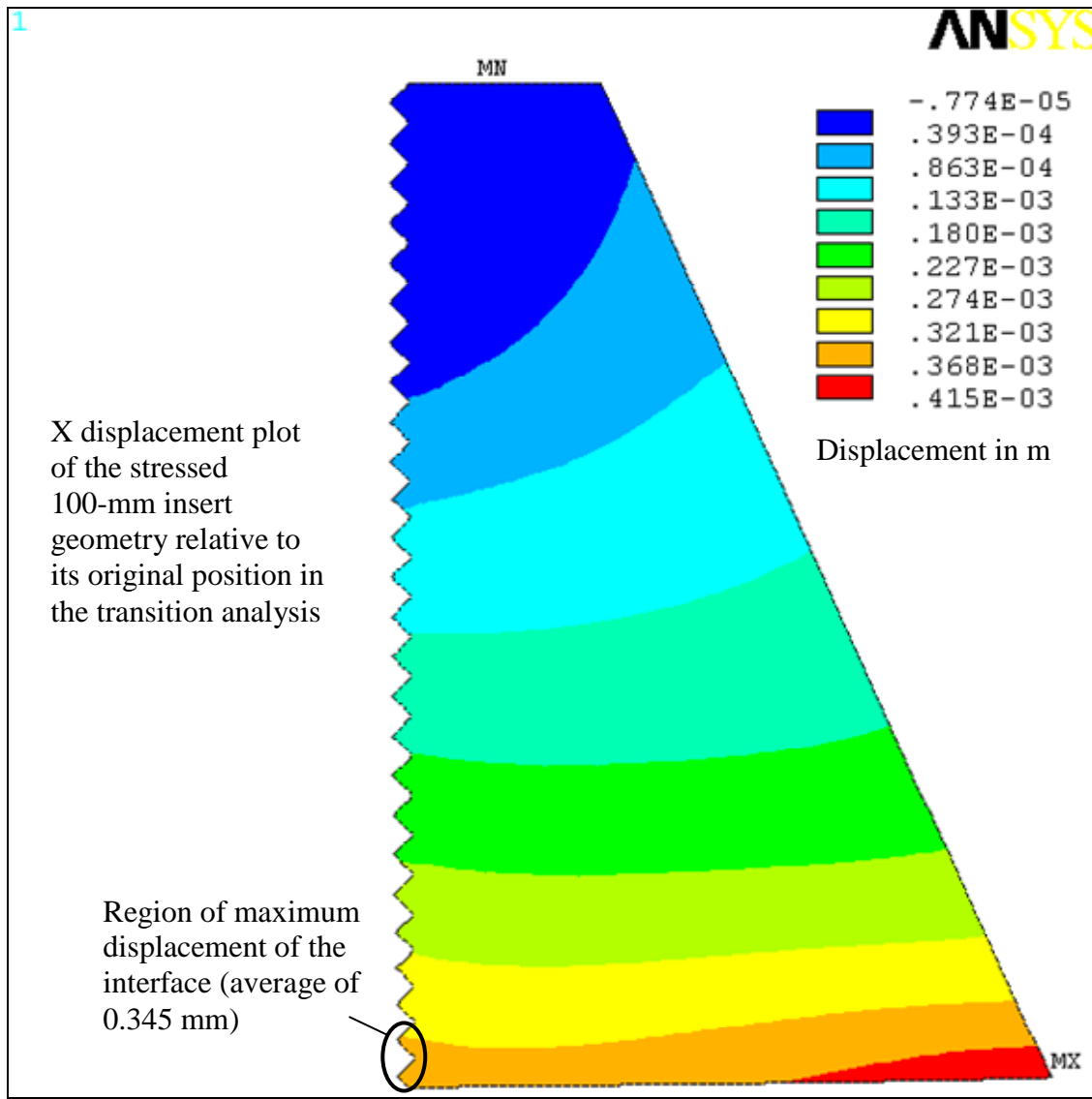


Figure 68. X-displacement plot of the 100-mm insert LFT section of the tailcone. A maximum displacement of 0.345 mm is calculated for the threads under load (3.6× greater than for the 95-mm insert geometry).

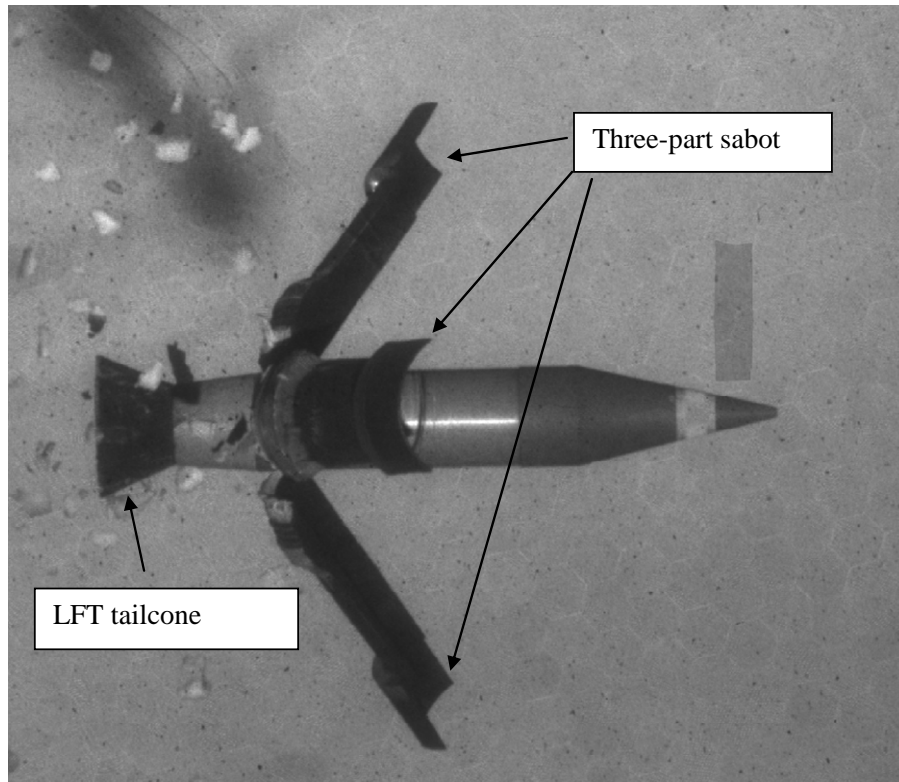


Figure 69. Fired projectile with full-back LFT tailcone geometry at 5 m. The filled-back tailcone maintained its integrity at a 5-m distance.

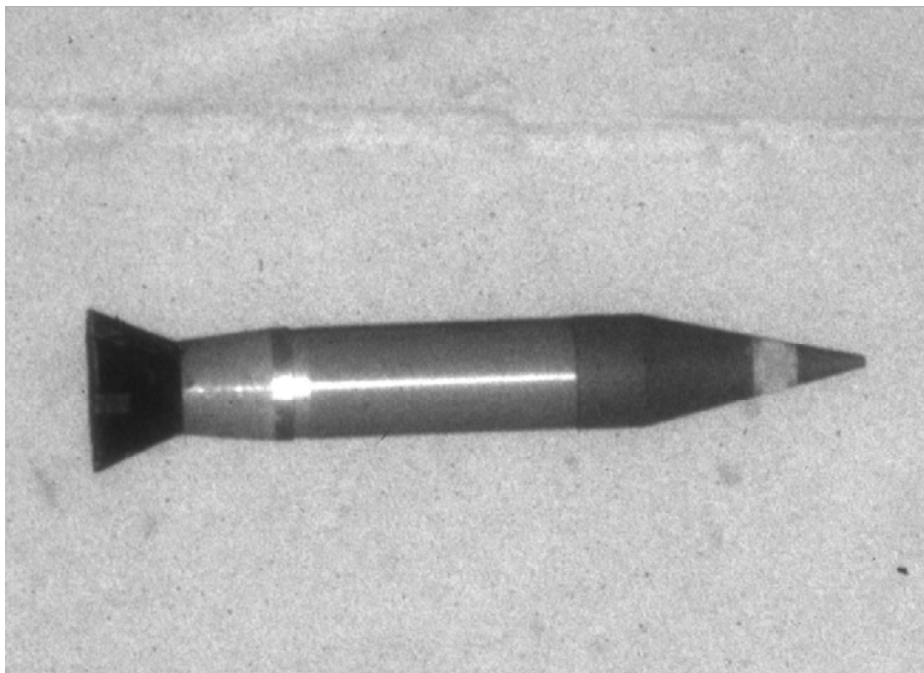


Figure 70. Fired projectile with full-back LFT tailcone geometry at 15 m. The filled-back tailcone maintained its integrity at a 15-m distance.

12. Summary and Conclusions

From the analysis and research conducted in this study, the following conclusions can be drawn:

1. A successful full-cycle design, analysis, tooling, prototype, manufacture, and validation of an LFT glass/nylon tailcone for an XM-1002 training round was accomplished.
2. Among two designs considered, the hollow-back and the filled-back LFT glass/nylon tailcone, the latter was successful in meeting all the loading conditions including temperature, pressure and gravity loads over the in-bore, transition, and out-of-bore tailcone scenarios (attached to the projectile) in actual firing.
3. The threaded metal insert was more effective in providing integrity to the LFT tailcone body at all stages of firing. The threads provided mechanical interlock where local stresses exceeded the yield stress of the material in few of the threads but did not compromise the body of the tailcone. The successful firing trials were obtained without any insert pretreatment.
4. Although the in-service allowable temperature of metals (aluminum) is higher than that of polymers (nylon), the specific heat (energy required to increase its temperature) is much higher for the latter. Also, the LFT material has extremely low thermal conductivity. This makes the LFT polymer less prone to failure from temperature. When dealing with armament, the manufacturers are skeptical about using polymers, but from the results in these tests, it has been observed that polymers (or polymer-based composites) are a good and inexpensive option to meet specific requirements.
5. The possibility of using the 100-mm insert geometry to place the tracer in the insert is viable, making the LFT tailcone as useful as the presently used aluminum version. The LFT tailcone is projected to cost 20% less than the aluminum baseline.
6. Considering the viscoelastic behavior of the LFT material, from a finite element analysis standpoint, a static analysis was adequate (and effective) to obtain an accurate analysis on a dynamic event.
7. The principal step toward a high-quality FEA is describing the constraints as close to the reality as possible.
8. The RTV sealant has proven to be effective in sealing the tailcone during high pressures without failing.

13. References

1. ATK. http://www.atk.com/ProductsSolutions/conventionalammo_largecaliber.asp (accessed March 2005).
2. Jones, A., Ed. *Speer Reloading Manual*, 4th ed.; Blount Inc. Sporting Equipment Division: Lewiston, ID, 2001; pp 23–50.
3. Munson B. R.; Young, D. F.; Okiishi, T. H. *Fundamentals of Fluid Mechanics*, 4th ed.; Wiley & Sons: New York, 2001.
4. Anderson, J. D. *Fundamentals of Aerodynamics*, 3rd ed.; McGraw Hill: New York, 2001.
5. Chawla, K. K. *Fibrous Materials*, 1st ed.; Cambridge University Press: New York, 1998.
6. Hartness, T.; Husman, G.; Koenig, J.; Dyksterhouse, J. The Characterization of Low Cost Fiber Reinforced Thermoplastic Composites Produced by the DRIFT Process. *Composites: Part A* **2001**, 32, 1155–1160.
7. Bush, S. F.; Torres, F. G.; Methven, J. M. Rheological Characterization of Discrete Long Glass Fiber (LGF) Reinforced Thermoplastics. *Composites* **2000**, 31, 1421–1431.
8. Chawla, K. K. *Composite Materials: Science and Engineering*; Springer: New York, 2001; pp 118–121.
9. Curtis, P. T.; Bader, M. G.; Bailey, J. E. The Stiffness and Strength of a Polyamide Thermoplastic Reinforced With Glass and Carbon Fibers. *J. Mater. Sci.* **1978**, 13, 377–390.
10. RTP Company. <http://www.rtpcompany.com/info/data/index.htm> (accessed January 2005).
11. Plastics Technology. <http://www.plasticstechnology.com/articles/200509rprice.html> (accessed March 2005).
12. Thomson, T.; Kamar, D. Computer Modeling of Pressures on 120 mm Tank Round in the M256 Gun. Presented at the National Defense Industrial Association 36th Annual Gun & Ammunition Symposium & Exhibition, San Diego, CA, 9–12 April 2001.
13. Shigley, J. E.; Mischke, C. R. *Mechanical Engineering Design*, 6th ed.; McGraw-Hill: New York, 2001.
14. McCoy, R. L. *Modern Exterior Ballistics: The Launch and Flight Dynamics of Symmetric Projectiles*, 1st ed.; Schiffer Publishing: Atglen, PA, 1999.
15. Kohnke, P. *ANSYS, Inc. Theory Reference*; SAS IP, Inc.: Canonsburg, PA, 1994.

16. Garner, J.; Bundy, M.; Newill, J. *Development of a Plastic Stabilizer for the M865 Training Projectile*; ARL-MR-445; U.S. Army Research Laboratory: Aberdeen Proving Ground, MD, 1999.
17. Sands, J.; Vaidya, U.; Husman, G.; Serrano, J.; Brannon, R. Manufacturing of a Composite Tailcone for an XM-1002 Training Round; U.S. Army Research Laboratory: Aberdeen Proving Ground, MD, submitted for publication, 2007.
18. Tsai, S. W.; Hahn, H. T. *Introduction to Composite Materials*, 1st ed.; Technomic Publishing Co.: Lancaster, PA, 1980.
19. MatWeb. <http://www.matweb.com/search/SpecificMaterial.asp?bassnum=O2514> (accessed June 2005).
20. eFunda, Inc. http://www.efunda.com/materials/polymers/properties/polymer_datasheet.cfm?MajorID=PA&MinorID=32 (accessed June 2005).
21. Ho, P. S.; Hahn, P. O.; Bartha, J. W.; Rubloff, F. K.; LeGoues, F. K. Chemical Bonding and Reaction at Metal/Polymer Interfaces. *J. Vac. Sci. Technol., A* **1985**, 3, 739–745.
22. Sirinyan, K.; Wolf, G. D. High Quality Polyamide/Metal Composites. *Ind. Eng. Chem. Res.* **1989**, 28, 1888–1892.
23. Ramani, K.; Moriarty, B. Thermoplastic Bonding to Metals Via Injection Molding for Macro-Composite Manufacture. *Poly. Eng Sci.* **1998**, 38, 870–877.
24. Lee, H. Y.; Qu, J. Microstructure, Adhesion Strength and Failure Path at a Polymer Roughened Metal Interface. *J. Adhes. Sci. Tech.* **2003**, 17, 195–215.

NO. OF
COPIES ORGANIZATION

1 DEFENSE TECHNICAL
(PDF INFORMATION CTR
ONLY) DTIC OCA
8725 JOHN J KINGMAN RD
STE 0944
FORT BELVOIR VA 22060-6218

1 US ARMY RSRCH DEV &
ENGRG CMD
SYSTEMS OF SYSTEMS
INTEGRATION
AMSRD SS T
6000 6TH ST STE 100
FORT BELVOIR VA 22060-5608

1 DIRECTOR
US ARMY RESEARCH LAB
IMNE ALC IMS
2800 POWDER MILL RD
ADELPHI MD 20783-1197

1 DIRECTOR
US ARMY RESEARCH LAB
AMSRD ARL CI OK TL
2800 POWDER MILL RD
ADELPHI MD 20783-1197

1 DIRECTOR
US ARMY RESEARCH LAB
AMSRD ARL CI OK T
2800 POWDER MILL RD
ADELPHI MD 20783-1197

ABERDEEN PROVING GROUND

1 DIR USARL
AMSRD ARL CI OK TP (BLDG 4600)

<u>NO. OF COPIES</u>	<u>ORGANIZATION</u>
3	US ARMY RESEARCH OFC D STEPP R SHAW T DOLIGALSKI PO BOX 12211 RESEARCH TRIANGLE PARK NC 27709-2211
1	DARPA TACTICAL TECHLGY OFC S WALKER 3701 N FAIRFAX DR ARLINGTON VA 22203-1714
2	DARPA DEFENSE SCI OFC W COBLENZ L CHRISTODOULOU 3701 N FAIRFAX DR ARLINGTON VA 22203-1714
1	COMMANDER US ARMY MATERIEL CMD AMSMI INT 9301 CHAPEK RD FORT BELVOIR VA 22060-5527
1	COMMANDER US ARMY TACOM PM COMBAT SYS SFAE GCS CS 6501 ELEVEN MILE RD WARREN MI 48397-5000
1	PEO GCS SFAE GCS BCT MS 325 WARREN MI 48397-5000
1	COMMANDER US ARMY TACOM PEO CS & CSS PM LIGHT TACTICAL VEHIC SFAE CSS LT M114 6501 ELEVEN MILE RD WARREN MI 48397-5000
1	US ARMY TACOM AMSRD TAR R D TEMPLETON MS 263 6501 E ELEVEN MILE RD WARREN MI 48397-5000

<u>NO. OF COPIES</u>	<u>ORGANIZATION</u>
1	NSWC CARDEROCK DIV R PETERSON CODE 28 9500 MACARTHUR BLVD WEST BETHESDA MD 20817-5700
1	NSWC CARDEROCK DIV R CRANE CODE 2802 9500 MACARTHUR BLVD WEST BETHESDA MD 20817-5700
1	MARINE CORPS INTLLGNC ACTVTY D KOSITZKE 2033 BARNETT AVE QUANTICO VA 22134-5011
3	UNIV OF ALABAMA AT BIRMINGHAM T JACKSON U VAIDYA G JANOWSKI BEC 254 1530 THIRD AVE SOUTH BIRMINGHAM AL 35294-4461
1	NORTH DAKOTA STATE UNIV C ULVEN DOLVE 111 PO BOX 5285 FARGO ND 58105
1	VIRGINIA TECH S R TURNER 2 DAVIDSON HALL 0201 BLACKSBURG VA 24061
1	UNIV OF DELAWARE J DEITZEL 219 COMPOSITES SCI LAB NEWARD DE 19716-3144
1	DREXEL UNIV G PALMESE 3141 CHESTNUT ST PHILADELPHIA PA 19104
1	TICONA D EMERSON 2600 OPDYKE RD AUBURN HILLS MI 48326

NO. OF
COPIES ORGANIZATION

ABERDEEN PROVING GROUND

18 DIR USARL
AMSRD ARL AP EG FI
M ADAMSON
AMSRD ARL HR
P DEITZ (BLDG 459)
AMSRD ARL WM
J SMITH
AMSRD ARL WM B
M ZOLTOSKI
AMSRD ARL WM BC
J GARNER
AMSRD ARL WM M
J BEATTY
S MCKNIGHT
AMSRD ARL WM MA
M VANLANDINGHAM
AMSRD ARL WM MB
L BURTON
A FRYDMAN
T BOGETTI
AMSRD ARL WM MC
M MAHER
AMSRD ARL WM MD
B CHEESEMAN
J SANDS
AMSRD ARL WM T
P BAKER
AMSRD ARL WM TA
S SCHOENFELD
AMSRD ARL WM TC
R COATES
AMSRD ARL WM TE
A NIILER

INTENTIONALLY LEFT BLANK.